THERMODYNAMIC AND FLUID PROPERTIES OF CELLS, TISSUES AND MEMBRANES

A Dissertation

Submitted to the Graduate School
of the University of Notre Dame
in Partial Fulfillment of the Requirements
for the Degree of

Doctor of Philosophy

by

Arpita Upadhyaya, M.Sc., B.E.

James A. Glazier, Director

Department of Physics
Notre Dame, Indiana

April 2000

THERMODYNAMIC AND FLUID PROPERTIES OF CELLS, TISSUES AND MEMBRANES

Abstract

by

Arpita Upadhyaya

This dissertation studies cellular rearrangements in tissues and attempts to establish the role of physical properties of cells, tissues and membranes in several biological phenomena. Using experiments and statistical mechanical modeling, we study cell sorting, tissue engulfment, single cell motion and membrane fluctuations.

When cells of two different types are mixed together, they sort out, with the less cohesive tissue surrounding the more cohesive one. This sorting out resembles the phase separation of a mixture of immiscible liquids. We have measured the rate of sorting in tissues and compared it with a cellular automaton based model of cell aggregates. We have also established that cell sorting agrees well with the theory for phase separating fluids.

Engulfment is the spreading of one type of tissue over the surface of another tissue placed adjacent to it. Differences in adhesion cause an imbalance of surface tension forces which drives tissue spreading. We have quantitatively studied engulfment between different tissue types and compared the experimental rate with results from computer simulations and a liquid model. Our results suggest that simple physical principles can model tissue motion.

Studying the motion of single cells in aggregates is important to understanding the overall pattern formation in tissues. We characterized cell motion in different types of adhesive aggregates to elucidate the role of adhesion in cell motion. We also observed that the cells exhibited a novel type of statistics including correlations and collective motion. Membrane deformations of cells played a negligible role in large scale cell motion. Our results indicate the importance of correlated motion for cells to move long distances in tissues.

At the single cell level, tension of the cell membrane and intracellular membrane can play an important role in cell shape changes, regulation of cell motility and membrane dynamics. We used optical tweezers to measure the membrane tension of tubulo-vesicular networks obtained from Golgi and Endoplasmic Reticulum (ER) membranes within cells. As expected on the basis of some previous experiments, the ER has a higher membrane tension than the Golgi.

To my parents, sister and Sridhar.

CONTENTS

FIGURES

ACKNOWLEDGEMENTS

I would like to thank my supervisor, Dr. James A. Glazier, for the guidance and encouragement he has provided in my work and also for the freedom that has enabled me to pursue several areas of research. I am grateful to my committee members for carefully reading this thesis and for their helpful suggestions. I gratefully acknowledge the hospitality of Prof. Yasuji Sawada of Tohoku University where I had the opportunity to collaborate with him and Jean Paul Rieu. I deeply appreciate Dr. Mike Sheetz at Duke University for opening up an entirely new field of research and most kindly allowing me to work in his lab for several months. I would like to acknowledge my lab members, Rich, Mark, Burk, Marius, Yi for their help and patience.

CHAPTER 1

INTRODUCTION

1.1 Overview

Morphogenesis is the establishment of the complex organization of tissues and organs during development. One of the most important morphogenetic processes is the movement of individual cells or tissue masses from one part of the body to another.

A cell is the functional subunit of all living organisms. Eukaryotic cells are extremely complex, but also highly structured and essentially similar at a basic level. Each cell consists of a cell membrane, cytoplasm and nucleus. The plasma membrane (a mixture of lipids and proteins) separates the interior self-contained world of the cell from its surroundings. The cytoplasm contains organelles that synthesize proteins and provide energy to the cell. The nucleus contains the cell's genetic blueprint in the form of DNA which passes from one generation to the next. In a developing organism, a single cell divides, differentiates (becomes specialized) and grows to become an entire adult. Remarkably, the developmental stages are similar in most animals from *Hydra* to human beings. This similarity allows us to hope for a general understanding of the common principles of development despite the varying specific mechanisms coded in the genetic programs. Further, these common principles can point to a quantitative description of the underlying processes.

Morphogenetic rearrangement involves the development of spatial pattern and structure within tissue masses. Although genes are crucial for pattern formation, genetics says nothing about the actual mechanisms involved. The genetic program provides the blue-print or recipe, but it cannot specify exactly where and how each cell in an organism needs to move. Genes determine the expression of specific molecules in cells which lead to certain physical properties - like viscosity of the cytoplasm or adhesion of the membrane. Differences in the expressions of these molecules control the nature of the particular cellular property. Physical forces and dynamical processes like gravity, adhesion, viscous shear, interfacial tension and reaction-diffusion mechanisms determine how these properties will interact and lead to formation of patterns involving motion and shape changes of the tissue. Aggregation of many cells in tissues can give rise to many tissue-specific properties like surface tension or viscoelasticity. Changes in the material properties of multicellular aggregates, for example changes in adhesion during embryogenesis, can play a large part in driving the transitions between different stages of development [10].

Two well documented examples provide strong evidence that universal physical properties play a central role in certain biological functions. One is the role of the elastic properties of soft shells (*e.g.* lipid bilayers or bilayer-cytoskeleton compound membranes) in shape changes of cells or of intracellular compartments (reviewed in [11, 12]). Measurable parameters of cell membranes include bending and shear elasticity and membrane viscosity. The second example is the role of nonspecific interaction mechanisms (such as van der Waals or electrostatic forces, osmotic effects and membrane undulation forces [13]) in cell-cell or cell-substrate interactions [14]. For example, one easily identifiable physical property that arises from interactions between membrane bound proteins (ligands and receptors) is adhesion.

Before coming to the specific topics of our research, in the next section we present some biological background that will be useful in understanding the work presented in this thesis. The book by Alberts *et al.* [10] is an excellent source for further details and references about the biology.

1.2 Biological Background

We start with a very simple picture of an animal cell and describe some of its internal structure and function. Most animal cells are eukaryotic cells, possessing a nucleus, whereas prokaryotic cells (like bacteria) do not. Most eukaryotic cells have the same basic composition. Plant cells differ from animal cells in that they possess a cell wall (cellulose matrix for structural rigidity), vacuoles (a large membrane bound vesicle to fill space) and chloroplasts (photosynthetic apparatus).

1.2.1 Cell Membrane

The plasma membrane encloses the cell and maintains the difference between the cytoplasm and the extracellular environment. It allows nutrients to enter the cell, filters out unwanted material and prevents metabolites from leaving the cell. It maintains the proper ionic composition and osmotic pressure of the cytoplasm. Other major functions are to communicate and interact with other cells and recognize extracellular signals. A very specialized structure allows for such a variety of tasks.

All biological membranes have a common general structure: each is a thin film of lipid and protein molecules held together by noncovalent interactions. The lipid molecules - mostly phospholipids - form a continuous double layer about 5 nm thick. Each phospholipid has a hydrophilic head group and two hydrophobic tails. The amphiphilic nature of the molecules causes them to spontaneously form bilayers in aqueous solution, in such a manner that hydrophobic tails are on the inside

and hydrophilic heads are exposed to water. These lipid bilayers tend to close on themselves to form sealed compartments called **vesicles**, eliminating hydrophobic free edges. Biological membranes are complex and contain many different lipid and non-lipid species, including different kinds of phospholipids, glycolipids (which play an important role in signal transduction and targeting [10]) and cholesterol (which is believed to have mainly a structural role [15]).

Two important properties of a bilayer are that it reseals when torn and it behaves like a fluid. Individual lipid molecules are able to diffuse freely within the bilayers - the common modes being lateral diffusion within a monolayer and rotational diffusion about their long axis. However, the rate of exchange of lipid between bilayers (flip-flop) is very small (the free energy barrier for doing so is of several kT). The fluidity or viscosity of a lipid bilayer depends on its composition and temperature and can regulate certain membrane transport processes. According to the Fluid Mosaic Model [16], the fluid bilayer serves as a matrix for functional proteins, which may be incorporated into the membrane as transmembrane proteins or adsorbed into the membrane surface. In the usual plasma membrane, about 50% of the mass is proteins or long chain polymers, and the composition varies according to function. Some examples of specific functional proteins are molecular pumps, ion channels, specific cell surface receptors and adhesion molecules. Proteins anchored in the lipid bilayer matrix can form interlinked structures, which give the otherwise fluid membrane some of the solid (elastic) structure of a cross-linked network. Such a cytoskeletal network exists beneath the plasma membrane of most cells and is rich in actin filaments which attach to the membrane in numerous ways. Membrane proteins are also free to move about in the membrane - by rotational diffusion (about an axis perpendicular to the bilayer plane) or lateral diffusion along the bilayer plane.

The energies that bind adjacent lipid molecules (lipids) to each other can range from 1-10^4 kT. Therefore, some types of membranes are in constant thermal motion and spontaneously undergo shape fluctuations. Lipids are free to move (flow) laterally; however, due to the fixed topology of the lipid molecules in the membrane, they have a finite bending stiffness unlike, say, the fluid film of a soap bubble. Surface tension, on the other hand, is very small. Also, neighboring lipids can chemically bind and thereby change the local stiffness.

1.2.2 Intracellular Organelles

Eukaryotic cells contain intracellular membranes that enclose nearly half the cell's total volume in intracellular compartments called organelles. The main types of membrane bound organelles that are present in all eukaryotic cells are the endoplasmic reticulum, Golgi apparatus, nucleus, mitochondria and several types of vesicles. Many vital biochemical processes, like lipid and protein metabolism, take place within or on membrane surfaces.

The largest membrane in a cell is the **endoplasmic reticulum** (ER) - a set of membrane tubules, sheets and sacs that fuse with each other to form a network, or **reticulum**. The ER specializes in the synthesis and transport of most membrane lipids and transmembrane proteins. The **Golgi apparatus** is a set of stacked, membrane bound, flattened sacs involved in modifying, sorting, and packaging macromolecules, received from the ER, for secretion or delivery into other organelles. Around the Golgi are numerous small membrane-bounded vesicles that carry material between the Golgi apparatus and different compartments of the cell.

Each intracellular compartment encloses a space that is topologically equivalent to the outside of the cell, and they all communicate by means of transport vesicles. A process called **exocytosis**, *i.e.* the fusion of protein filled vesicles with the plasma

membrane, transports proteins synthesized in the ER to the plasma membrane and secretes them from cells. **Endocytosis** is the reverse process by which cells ingest macromolecules from the external environment. Localized regions of the plasma membrane invaginate and pinch off to form endocytotic vesicles. Within the cell, transport vesicles that bud off from one membrane and then fuse with another mediate exocytotic and endocytotic pathways.

1.2.3 Cytoskeleton

The cytoskeleton is the internal structural framework of cells which controls the spatial location of protein complexes and organelles and provides communication pathways between them. It provides mechanical support and makes possible the coordinated and directed movements of cells. It is a highly dynamic network that reorganizes continuously as the cell changes shape, divides and responds to its environment. The cytoskeleton consists of three main types of polymerized filaments.

Actin

Actin filaments are double stranded helical polymers formed by self-assembly of actin monomers. Polymerization of actin is a dynamic process that requires hydrolysis of the nucleotide adenosine triphosphate (ATP). In cells, approximately half the actin is present as monomers and actin molecules continually polymerize and depolymerize during cell motion. Extracellular signals binding to cell surface receptors can regulate polymerization. Actin filaments are polar and have a fast-growing plus end and a slow-growing minus end. These filaments are flexible structures (8 nm in diameter) that are usually found as linear bundles, two-dimensional networks and three-dimensional gels rather than as single filaments. They occur throughout the cell, but concentrate most densely in the cortex, just beneath the plasma

membrane. Several different actin binding proteins (*e.g.* fimbrin, filamin, α-actinin, villin, fascin) can bind or cross-link individual actin filaments to form various types of networks with different mechanical properties. The actin rich cortex controls the shape and surface movements of most animal cells.

Actin interacts with a very important motor protein called **myosin**. Motor proteins are a class of proteins that hydrolyze nucleotides to generate different types of movement in eukaryotic cells. Myosin hydrolyzes ATP in the presence of actin and uses the energy of hydrolysis to move along actin filaments, either carrying membrane bound organelles from one location to another or moving adjacent actin filaments relative to each other. Actin-myosin interactions are crucial to muscle contraction, cell locomotion and cell division.

Microtubules

Microtubules are long hollow cylinders made of the protein tubulin. With an outer diameter of 25 nm, they are much more rigid than actin. They are also polar and have a fast-growing plus end and slow-growing minus end. In most cells, the minus ends of the microtubules are embedded in the centrosome which is the primary site of nucleation of microtubules. The centrosome lies next to the nucleus, and the plus ends extend out radially to the edge of the cell. Each microtubule is a highly dynamic structure that grows and shrinks by addition and loss of tubulin subunits during polymerization-depolymerization cycles. This behavior, called dynamic instability, plays a major role in positioning microtubules in the cell. Spatially controlling the assembly and disassembly of tubulin molecules can polarize cells (structurally orient them in a specific direction).

Motor proteins use the microtubule network as a scaffold to position membrane-bound organelles within the cell. The two types of motors associated with micro-

tubules are: **kinesin**, which moves towards the plus end and **dynein**, which moves towards the minus end. Each motor carries a distinct cargo of membrane bound vesicles filled with proteins as it moves. The membrane tubules of the ER form a network on a microtubule mesh and the Golgi apparatus is present near the nucleus. When cells are treated with a drug to depolymerize microtubules or when a cell undergoes division, the ER and Golgi collapse into small vesicles. When the drug is removed or when cell division is over, the organelles return to their original positions, dragged by motor proteins moving along the microtubules. Microtubule based organelle motility is largely responsible for most directed transport of proteins within the cell.

Intermediate Filaments

Intermediate filaments are strong and ropelike with a diameter of around 10 nm. They are polymers of a heterogenous family of fibrous polypeptides called intermediate filament proteins. The several tissue-specific forms include keratin of the skin, neurofilaments of nerve cells, vimentin of fibroblasts and desmin filaments of muscle cells. These filaments resist stretching and play a structural or tension-bearing role in the cell. Because of their organization in overlapping arrays, intermediate filament fibers can withstand much larger stretching forces than microtubules and actin microfilaments. An extensive network of intermediate filaments surrounds the nucleus and extends out to the cell periphery. These filaments extend across the cytoplasm and connect neighboring cells via focal plaques. They provide mechanical strength to the cells and carry the stresses in tissues by spanning the tissue from one cell to the next.

1.2.4 Cell Adhesion

Adhesive interactions are central in numerous biological functions like tissue assembly (during development) and identification and removal of alien organisms by the immune defense system. Many different adhesion mechanisms are possible [17] including electrostatic interactions [18, 19], adherens junctions [20, 21] and specific or non-specific adhesion molecules [22, 23, 24]. Differential intercellular adhesivity arising from type specific adhesion molecules on the cell surface can direct the movement of cells [2, 25, 26]. At least two classes of adhesion molecules have been identified: (1) those that mediate cell attachment to the extra-cellular matrix (cell-matrix adhesion molecules), and (2) those that mediate cell attachment to other cells (cell-cell adhesion molecules). Cell-cell adhesion arises due to the presence of different kinds of transmembrane protein receptors (Cell Adhesion Molecules - CAMs or cadherins) which bind to ligands from other cell membranes. Adhesion molecules also directly link to the internal cytoskeleton of the cell (mainly to actin filaments). Both ligand-receptor bonds or linkages to cytoskeletal structure can govern the strength of attachment between two surfaces.

Cell adhesion plays a more important role than mere surface binding with other cells or substrates. Adhesion usually initiates signalling pathways to activate and modulate internal cell functions. These chemical signals lead to physical changes of cellular properties like rigidity, cell motion and cell-substrate interactions. During development, many different cell types travel long distances through changing environments to reach their final destinations. Intrinsic to this process are decisions about when to migrate, the paths to be taken (which may depend on external signals), and when to stop.

The mechanism of cell mobility is still a matter of debate in developmental biology (see reviews in [27, 28, 29, 30]). Adhesion plays a key role in guiding cell motion. Adhesion guided cell migration is very important in all stages of an animal's life. It is crucial in the growth of developing embryos (*e.g.* cells migrating on substrates [31], cell sorting [2], gastrulation, epiboly, organ formation) as well as in adults (*e.g.* wound healing and the spread of cancer metastases [24, 32]). Adhesion itself cannot move cells: it helps to select the most favorable configuration amongst different possibilities explored by the moving cells [33, 34, 35]. Each cell must actively explore its neighborhood [36, 37], using protrusions [2, 38] and contractions [28, 39, 40]. In the next subsection, we give a brief description of some common mechanisms of cell locomotion.

1.2.5 Cell Migration

Most cell types have the capacity to move from one place to another in their natural surroundings. Cells can move over or through a substrate and within a tissue of other cells. Most cells require an environment where they can form attachments via their membranes but sometimes free cells can move in solution (for example, swimming bacteria, *Listeria monocytogenes*, nematode sperm). The most common type of cell motion is amoeboid (or crawling) motility, which has been the subject of scientific scrutiny since the advent of the optical microscope (see [41, 42, 43, 44, 45, 46, 47, 48] for some excellent reviews). The basic engine for crawling locomotion is the actin cytoskeleton. Cell locomotion is very complex, requiring the coordinated activity of cytoskeleton, membrane and adhesion systems. The migration of a single cell moving over a substrate divides into four distinct actin-dependent subprocesses. (1) **Protrusion** is the forward motility of the membrane at the leading edge of the cell. (2) **Adhesion** between the actin cytoskeleton and substratum converts protrusion

into movement along the substrate. (3) **Traction** is the process leading to forward movement of the cell body. (4) **Deadhesion** and **tail retraction** comprise the last step in locomotion. Whether retraction is actively motile depends on the cell type.

Protrusive structures at the leading edge of motile cells are highly dynamic and contain dense arrays of actin filaments. These membranous structures exclude from cytoplasmic organelles. **Lamellipodia** are broad, flat, sheet-like structures containing a web of actin filaments that cross-weave at about 45° to the direction of protrusion [49, 50]. **Filopodia** are thin, cylindrical needle-like projections with a tight bundle of long actin filaments oriented in the direction of protrusion [51]. In some cell types, rib-like microspikes that resemble small filopodia punctuate the lamellipodia. Amoeboid cells like *Dictyostelium* protrude using thicker processes called **pseudopods** which have a cross-linked mesh of actin filaments.

In all of these structures, the membrane tightly couples to the polymerization of actin filaments at the extreme leading edge [47, 52, 53]. The most important physical problem is the generation of protrusive force required for the membrane to move forward. Actin polymerization itself or the action of motor proteins could generate the force for protrusion. Force production requires an energy source within the cytoplasm, which ultimately derives from the chemical energy of ATP hydrolysis. In motor-based models, myosin motors attached to the plasma membrane actively walk along the actin filaments and transduce hydrolysis energy directly into force, pushing the membrane tip forward. Theoretical analyses argue that local actin polymerization is in itself an adequate energy source for extension against the mechanical resistance provided by the cell membrane [54, 55]. Polymerization of pure actin inside a lipid vesicle can deform the membrane [56]. The thermal ratchet model developed by Peskin *et al.* [57] can explain the physical coupling of

the membrane protrusion to polymerization of actin. Thermal fluctuations of the membrane or length of actin filament create gaps between the membrane edge and tip of the actin filaments. Polymerization then fills in the gaps, preventing backward movement of the membrane, thereby rectifying Brownian motion into unidirectional motion.

The plasma membrane may be too stiff to deform at the required rate by thermal fluctuations alone. Another potential source of fluctuations is thermally driven changes in the effective length of the polymerizing filaments due to temporary bending. Taking into account the elasticity of the actin polymer, Mogilner and Oster [58] formulated a model which explains several experimental results on cell protrusion. These models show that the force generated by polymerizing actin filaments has more to do with the physics of polymerization than with any other property peculiar to actin. An active process - polymerization powered by ATP hydrolysis - causes membrane deformations that lead to cell motion, which will therefore have different characteristics (amplitude and frequency) from the thermal fluctuations of a free membrane. Since the amplitude of thermally driven fluctuation is proportional to the ambient temperature, the amplitude of cytoskeletally driven cell membrane deformations will be analogous to an "effective fluctuation temperature" to which we refer in later chapters.

Motility of cells in a tissue is much more complicated to study than motion on two-dimensional substrates. The basic mechanism remains the same, but, due to the large number of interactions, the cells may receive and have to respond to multiple types of signals in order to move. Adhesion plays an important role for migration at two levels - at the single cell level as explained for a cell on a substrate; and at the level of tissues, where cell surface molecules create gradients of adhesion energy

compelling cell masses to travel down these energy gradients during global tissue reorganization. The following sections describe some examples that demonstrate the role of adhesion and migration in mediating developmentally critical processes.

1.3 Cell Sorting

As early as 1744, Trembley performed several simple experiments on the regeneration of *Hydra* including development of an adult from aggregates of dissociated cells [59]. These were among the first experiments to demonstrate that tissues could be so easily taken apart and reassembled. In the early 1900's, Henry V. Wilson showed that when a marine sponge is cut up into minute fragments, each fragment regenerates into a complete individual [60]. What would happen in the extreme situation of dissociating a tissue into its smallest viable units - cells? Wilson dissociated sponge tissue into single cells by pressing live sponges through finely woven cloth. The dense suspension of cells condensed into clusters that soon organized into tissues and eventually developed into complex sponges. These experiments suggested the importance of cell-cell adhesion in morphogenesis. Regeneration was, however, thought possible only in primitive creatures.

In 1944, Holtfreter [61] observed that when he mixed different kinds of cells from amphibian embryos, the cell types spontaneously sorted out to yield homogeneous and coherent tissues. This observation led to the idea of "tissue specific affinities" [62]. Holtfreter proposed several possible mechanisms for "tissue affinities" including differences in the degree of cell adhesiveness, "directed movement" or **chemotaxis** (cells moving in response to a chemical gradient). Steinberg [33, 63] demonstrated that the behavior of aggregates of isolated and recombined embryonic tissues does not conform to expectations based on chemotaxis, but instead closely

resembles liquid behavior. The Differential Adhesion Hypothesis (DAH) proposed by Steinberg [33] successfully explains how cellular properties can operate to determine tissue reorganization during cell sorting. The DAH proposes that (1) cells of a given type have characteristic adhesion strengths to cells of the same or different types, (2) the cells comprising an aggregate are motile and (3) the final organization of cells maximizes the strength of adhesive interaction summed over all the adhesive contacts in the aggregate. This explanation defines cell adhesion as the reversible work of adhesion (the work done when one unit of cell surface area moves from the surface of the aggregate into the interior). The reversible work of adhesion is directly proportional to minus the interfacial free energy (the change in the free energy when the surface area of a spherical cell aggregate increases reversibly by one unit at the expense of one unit of area of cell-cell contact).

Sorting transforms an array of initially disordered cells into one in which the cells form homogeneous tissue domains. This sorting is one of the key steps in the reconstruction of organs and limbs. Tissues from many different organisms exhibit this behavior, indicating that it is very general and does not depend on specific genetic pathways. Mixed populations of cells from a variety of phylogenetic groups sort, including invertebrates [64] and vertebrates [61, 65], cell aggregates and monolayer cultures [66, 67], and cells from embryonic [61, 65, 68], postnatal [69] and adult [70, 71] stages of development (for more references see [2]).

Differences in both the type and number of adhesion molecules [72, 73] drive cell sorting. Does differential adhesion directly mediate sorting in the whole animal? *In vivo* evidence has been difficult to obtain mainly because several adhesion molecules could be acting in concert and adhesion can play many roles simultaneously. Recently, however, Godt and Tepass [1] and Gonzalez-Reyes and St. Johnston [74]

obtained the long-sought *in vivo* evidence that cadherin levels can mediate sorting during development. Both groups studied follicles of the fruit fly (*Drosophila melanogaster*) ovary, which contain two types of germline cell, the oocyte and its attendant nurse cells. These form a compact package, surrounded by a single layer of epithelial follicle cells. The oocyte sits next to the follicle cells at the posterior pole of the follicle, and proper positioning is a key to setting up the anterior-posterior polarity of both the egg and the embryo that develops from it. Thus we have a small-scale model of morphogenesis - how does the oocyte know to move to the posterior pole?

By genetically manipulating the levels of expression of E-cadherin in the various cell types, they concluded that the oocyte and posterior follicle cells express higher levels of E-cadherin than do nurse cells, ensuring that the oocyte moves to the posterior pole. In follicles modified so that the posterior-most follicles do not express cadherin, the oocyte takes a random position. When follicle cells express different levels of cadherin, the oocyte moves preferentially adjacent to the cells expressing the highest levels of cadherin. Figure 1.1 shows this process in cartoon as well as a photograph of the oocyte in wild type and mutant follicles. These experiments provide a direct and dramatic confirmation of Steinberg's theory: first, that differences in cell adhesion can drive morphogenetic movements *in vivo*; and second, that differences in the level of a single cell-adhesion molecule suffice to mediate cell sorting in an intact tissue.

1.4 Engulfment

The behavior of two homogeneous tissue aggregates placed in contact with each other can elucidate the mechanisms of cell sorting. Typically, one tissue type spreads over

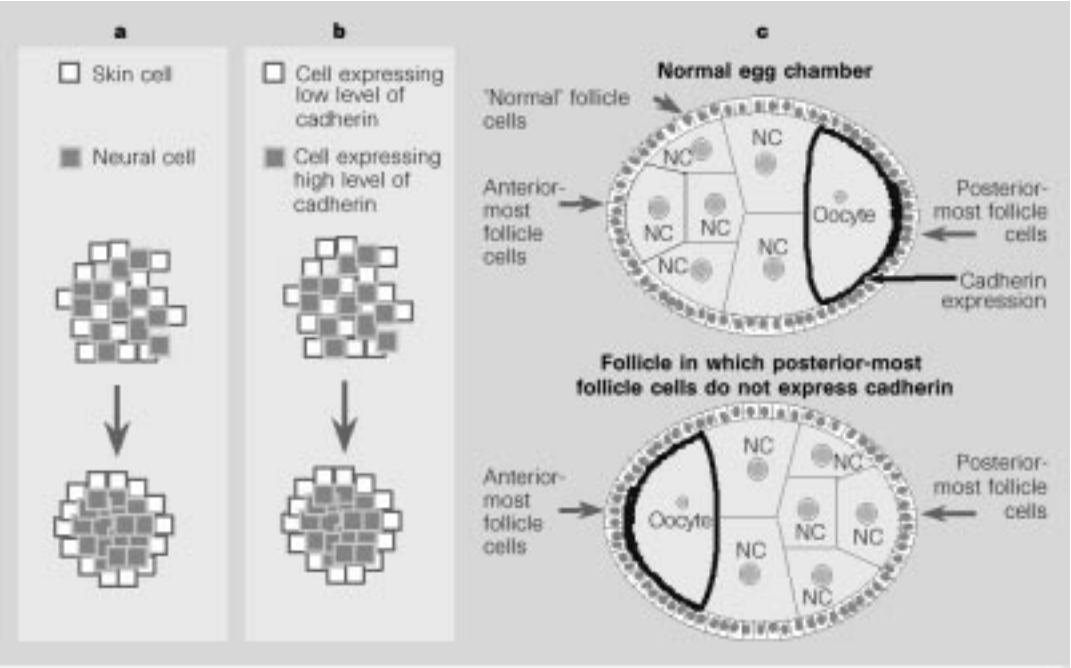

Figure 1.1. Cell sorting during development: (a) *In vitro*, cells can sort according to type, with neural cells preferentially sticking to other neural cells. Expression of different cadherins drives this sorting. (b) Cells also sort based on the level of cadherin expression, with cells expressing high levels of cadherin preferentially sorting to the center. (c) Cadherin levels can mediate sorting during development *in vivo*. The oocyte and posterior follicle cells express higher levels of E-cadherin than do nurse cells (NC) and other follicle cells, ensuring that the oocyte sits at the posterior pole (from [1]).

the surface of the other, often enveloping it completely, during the succeeding 2-3 days of culture [33, 35, 62, 75] as shown in Figure 1.2 [2]. This phenomenon is called **engulfment**. Many processes during embryonic morphogenesis resemble mutual engulfment of tissues. These include the spreading of the chick blastoderm on the inner surface of the vitelline membrane [76], the spreading of the chick embryonic epicardium over the myocardium [77], gastrulation [78], teleost epiboly [79], the elongation of the salamander pronephric duct over the lateral mesoderm [80], and the condensation of precartilage mesenchymal cells [81].

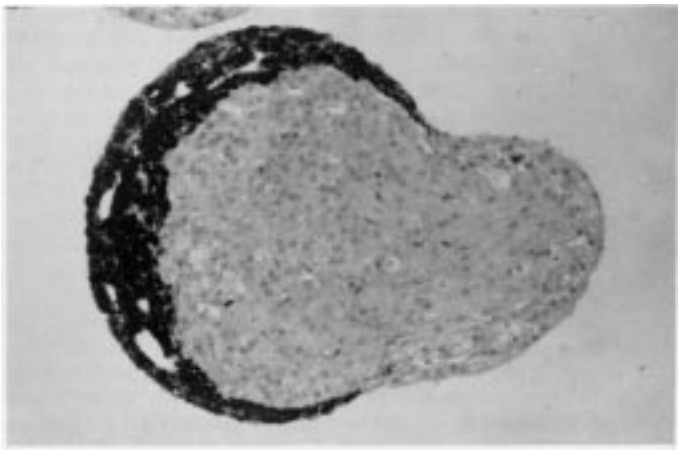

Figure 1.2. Engulfment. Spreading of 10 day old chick embryo pigmented retinal (dark) tissue over the surface of an aggregate of 10 day old heart (light) tissue (from [2]). During envelopment, the pigmented retinal tissue reduces the area available for homotypic contact while expanding contact area with the heterotypic tissue.

Most experiments have observed that the final arrangement established by spreading of two tissues in contact is the same as that generated by cell sorting of mixed cell aggregates comprising of the same two cell types [33, 35]. Engulfment experiments allow the use of tissue fragments dissected directly from the organism, without tissue dissociation which can modify the adhesive character of the cell surface [82].

Any comprehensive theory of cell sorting must explain why cohering cell populations generate the same final configurations from very dissimilar initial organizations: sorting of two randomly mixed cell types or spreading of one tissue over another when the two are placed in contact. Cells' sorting out in the same manner regardless of the initial conditions supports Steinberg's idea that global energy minimization determines the final configuration.

Differences in the intensities of cell adhesion direct the spreading of one tissue over the surface of another. These two tissues can either be of different *types* obtained from different parts of a developing embryo or they can be the same cell type expressing different *numbers* of the same adhesion molecules. Using genetically engineered cells, Steinberg and Takeichi proved that simple quantitative differences in the level of expression of a single adhesion molecule cause tissues to be immiscible and sort out or spread over one another [73].

1.5 Tissue Interfacial Tension

The equilibrium arrangement of sorting and engulfing tissues imitates the behavior of immiscible fluids: in the absence of gravity the fluid of higher surface tension surrounds the fluid of lower surface tension. (In sorting experiments, the almost neutral buoyancy of the culture medium and tissues neutralizes gravity). This resemblance suggests that tissues possess tissue specific surface and interfacial tensions, which arise from the cohesive and adhesive interactions of their constituent cells. Previous experiments [5, 6, 73, 83, 84] have established quantitative and qualitative correlations between equilibrium properties of living tissues and fluids.

Experimental studies in the past have qualitatively established the liquid properties of tissues [3, 83, 85]. A liquid is regarded as a population of cohesive mobile

subunits. The presence of surface adhesion molecules gives rise to an effective surface tension of tissues, a measurable area invariant quantity. Indeed, the rounding up of tissue fragments to minimize their surface area manifests liquid like behavior. The sorting out of intermixed phases by coalescence seems analogous to the demixing (phase separation) of immiscible fluids. When two tissues with different surface tensions come into contact, the lower surface tension tissue spreads over the surface and "engulfs" the other. Surface tensions of embryonic tissues predict their mutual envelopment behavior. In a set of mutually immiscible phases, the tendencies of one phase to spread over another are transitive (*i.e* if b tends to spread over a and c tends to spread over b, then c will spread over a) as Figure 1.3 shows schematically.

We can measure surface tension, a liquid's resistance to an increase of surface area, by deforming a droplet and then monitoring its final equilibrium shape as a function of the applied force [86]. Foty *et al.* [3, 83] have measured the interfacial tensions of several different tissue types and provided a quantitative basis for the Differential Adhesion Hypothesis. They used a parallel plate compression apparatus which recorded the force applied to a living cell aggregate and the aggregate's shape to monitor the approach to shape equilibrium. Figure 1.4 shows the profile of an initially spherical aggregate compressed between two parallel plates, after it has reached equilibrium.

Laplaces's law gives the surface tension of such a droplet:

$$\sigma = \frac{F}{\pi {R_3}^2}\left[\frac{1}{R_1} + \frac{1}{R_2}\right]^{-1}, \tag{1.1}$$

where σ is the interfacial tension between the droplet and the immersion medium, F is the measured decrease in weight of the upper compression plate, R_1 and R_2 are the two principal radii of curvature of the droplet's surface and $\pi {R_3}^2$ is the area of contact between the droplet and the parallel compression plates. The term

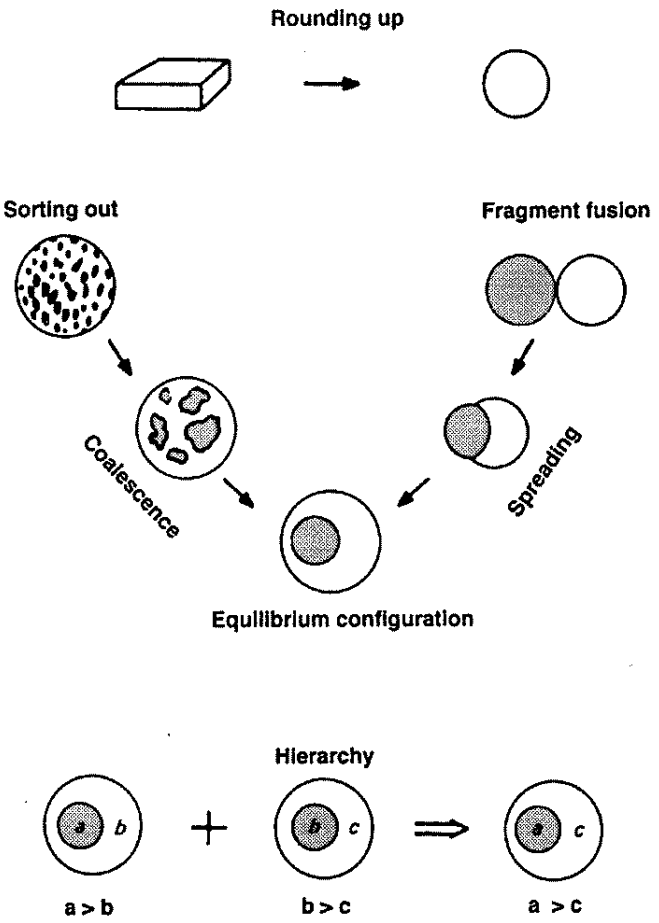

Figure 1.3. Liquid-like behavior of biological tissues. **Top**: A cell mass of arbitrary shape rounds up to form a sphere, minimizing its surface area. **Middle**: Intermixed phases sort out by coalescence. When brought into contact, the same two phases spread over one another to approach the same equilibrium configuration as sorting. **Bottom**: For mutually immiscible phases, the tendencies of one to spread over another are transitive.

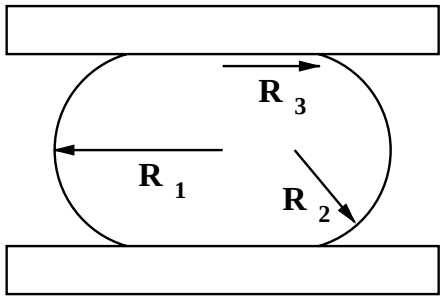

Figure 1.4. A liquid droplet compressed between parallel plates, at shape equilibrium (adapted from [3]).

$F/\pi R_3{}^2$ is the external pressure due to the compression. The measured interfacial tensions of five different tissue types from chick embryo are: limb bud mesoderm - 20.1 dyn/cm, pigmented epithelium - 12.6 dyn/cm, heart - 8.5 dyn/cm, liver - 4.6 dyn/cm and neural retina - 1.6 dyn/cm [83]. The measured values of surface tension were independent of the aggregate volume, as for liquids. To examine the relationship between tissue surface tension and envelopment behavior, Foty *et al.* mixed binary combinations of cells from adjacent tissues in the surface tension hierarchy. Neural retinal tissue envelops liver tissue which envelops heart tissue which in turn envelops pigmented epithelium. As in liquids, the body with lower surface tension always spreads over the outside surface. This hierarchy provides direct evidence of the role of surface tension due to differential adhesion in tissue organization.

Davis *et al.* [84] demonstrated that the same principles apply during amphibian gastrulation. Aggregates of *Rana pipiens* deep germ layers possess liquidlike surface tensions and their surface tension values lie in precisely the order necessary to account for germ layer behavior *in vitro* and *in vivo*. Their measurements provide direct, quantitative evidence that the intercellular adhesions governing cell flow during early stages of vertebrate morphogenesis create tissue interfacial tensions.

Since surface tension is an equilibrium property, it determines the final equilibrium configuration of a set of interacting liquids (tissues). However, it does not fix the time scale or dynamics by which these processes achieve equilibrium. In liquids, the ratio of surface tension to viscosity governs the time course of flow. Early experiments by Phillips and Steinberg [39, 87] showed that cell aggregates are viscoelastic in nature, *i.e.* they behave like elastic solids during brief deformations but like viscous liquids in long term cultures. The major components of cells also possess viscoelastic properties [85].

1.6 Role of Cell Motion

These observations of cell sorting and engulfment do not reveal the mechanisms which cause the cells to move and rearrange in the right way. Even if differences in surface tension contribute to the driving force for movement during morphogenesis, they reveal little about its time course. The kinetics of cell-sorting and tissue envelopment depend on the dynamical properties of cells and cell populations. Membrane fluctuations intimately couple to cell locomotion at the single cell level. How do membrane fluctuations work in cell populations to guide motion?

Studies of cell locomotion of eukaryotic cells have focused mainly on single cells or groups of cells on two-dimensional adhesive substrates. Typically, these studies employ non-interacting cells in well-defined surroundings, on substrates coated with different adhesive molecules with different buffer media [88, 89, 90]. Motion of cells within cellular aggregates or inside tissues has not been well studied. Cell-cell interactions and the properties of the surrounding cellular environment will influence cell behavior and may change the nature of cell motion from motion on substrates. Cell motion requires a complex series of mechanical and molecular processes such as

membrane extension, attachment to the substrate, generation of force and detachment from the substrate [44]. As the underlying processes leading to cell motion are very complicated, a detailed mathematical description is difficult. Therefore, characterizing the statistics of cell displacements can provide important information about the mechanism of cell motion without constructing a mechanistic model. Statistical studies of cell locomotion have shown that, in the absence of external biases like chemotactic sources or tissue rounding effects, cell motion is usually diffusive [6, 89, 91, 92]. The mean squared displacement is linear in time with a characteristic diffusion coefficient D:

$$\langle r^2 \rangle = Dt. \tag{1.2}$$

The distribution of speeds (V) follows the Maxwellian distribution:

$$F(V) = aV\exp(-bV^2). \tag{1.3}$$

The thermodynamics of a moving cell resemble those of a particle in a fluid undergoing thermal motion. The cell experiences random fluctuating forces from its surroundings and is damped by the viscosity of the cellular aggregate. We can write the equation of motion for the cell/particle in such a situation as the Langevin equation:

$$dv/dt = -\alpha v + F(t), \tag{1.4}$$

where v is the velocity of the particle, α is a damping constant ($1/\tau$), and $F(t)$ is the fluctuating force per unit mass, called the Langevin force. If the force is truly random then the time average of the force is zero, and the correlation function is a delta function as in Brownian motion. In Brownian motion, we cannot predict a single path but only its averaged statistical properties. One of the most important averages

is the two-time velocity auto-correlation function which measures the characteristic time beyond which the motion is uncorrelated:

$$< v(t)v(t') >= (C/2\alpha)e^{-\alpha|t-t'|}, \tag{1.5}$$

where C is the amplitude of the correlation function of the fluctuating forces, while α corresponds to the damping constant, the inverse of which is the correlation time.

Several experiments have demonstrated the analogy with fluids. The center of mass displacement of a single pigmented retinal cell of chick embryo in a three-dimensional aggregate of neural retinal cells, shows diffusive motion [91] with Maxwellian velocity distributions. Fibroblast cells observed in three-dimensional isotropic collagen gels (when the collagen fibers have no preferred orientation) [93] move diffusively. In gels with oriented fibers, cells execute a biased random walk [94]. Typically, for diffusive motion, temporal and spatial velocity autocorrelations decay exponentially with a short time constant, indicating no long range effects. Deviations may indicate memory effects (long range correlations in time) or bulk effects such as collective motion of groups of cells (long range correlations in space). Czirok *et al.* [92] found exponential velocity distributions for non-interacting cells on substrates but they did not quantify the diffusion of these cells. They explain their results with a phenomenological model based on competition for ATP among different cellular reactions. Changing the type or strength of adhesive substrates can control the rate of cell migration, fastest motion occuring for intermediate adhesion strengths. Our experiments with *Hydra* cells have shown that cells move faster in a less adhesive cellular environment and also show a novel type of statistics. We describe these results in Chapter 5.

1.7 Biomembranes

So far we have focused on cell movements and the role of tissue surface tension as well as other macroscopic properties on pattern formation in tissues. The motion of individual cells controls the dynamics of large scale tissue movements, while intra-cellular processes control cell motility itself. Physical properties of cell membranes including adhesion, tension and bending modulus can become important determinants of cell and tissue function, including cell-cell interactions, cell membrane deformations and cell movement.

A very simplified model treats a cell as cytoplasm contained by a membrane. Vesicles are closed membranes suspended in aqueous solution. Vesicles serve both experimentally and theoretically as simplified models of cells. Their equilibrium properties have been investigated extensively [15, 95, 96]. Bilayer membranes are fluid, with very small in-plane shear modulus and large compression modulus and bending modulus. The molecules in a bilayer rearrange to minimize the free energy, constrained by the fixed volume of the vesicle and the number of molecules. Because the membrane is fluid, we can sum over all the internal degrees of freedom and the free energy will depend only on the shape of the vesicle. At equilibrium, the free energy is a minimum with respect to the area. The relevant contributions to the free energy arise from the curvature. In order to bend the bilayer, a positive tension (σ_+) has to act at one monolayer and a negative tension (σ_-) at the other which result in the bending moment $M = d_m(\sigma_+ - \sigma_-)$ (where d_M is the membrane thickness). The mean curvature $H = (\frac{1}{R_1} + \frac{1}{R_2})$ (where R_1 and R_2 are the principal radii of curvature measured along two perpendicular directions) characterizes any curved

surface. The bending moment is then:

$$M = K_c\left(\frac{1}{R_1} + \frac{1}{R_2}\right), \tag{1.6}$$

where K_c is the bending elastic modulus measured in units of energy. Helfrich showed that the main contribution to the elastic free energy of a membrane is due to bending and can be described by the Helfrich Hamiltonian [97]:

$$F = \int dA \frac{1}{2} K_c (H)^2, \tag{1.7}$$

where dA is a surface element, and the integration is performed over the entire bilayer surface. If the two sides of the membrane bilayer are not identical, having the membrane assume a spontaneous curvature H_s (*i.e.* the mean curvature which minimizes the free energy) drastically reduces the bending energy. $H - H_s$ then replaces H in the previous equation. The bending or curvature modulus K_c gives the energy cost of deviating from the spontaneous curvature. In addition to bending, cell membranes can deform due to shearing or compression (which have a negligible effect for pure lipid membranes). The elastic energy per unit area characterizes the resistance of bilayers towards compression or elongation:

$$g_{comp} = \frac{1}{2}\kappa\left(\frac{\Delta A}{A}\right)^2, \tag{1.8}$$

where $\frac{\Delta A}{A}$ is the relative change in bilayer area and κ is the compressibility modulus. We can visualize shearing by considering a square piece of bilayer which is stretched in one direction by a tension σ_+ to a length $L = L_0 + \delta l$ and compressed to $L = L_0 - \delta l$ in a perpendicular direction by a tension σ_-. The area remains constant and the strain is $\lambda = (L_0 - \delta l)/L_0$. The energy (per unit area) is:

$$g_{shear} = \frac{1}{2}\mu(\lambda^2 + \lambda^{-2} - 2), \tag{1.9}$$

where μ is the shear elastic modulus.

The area, volume and total curvature of membrane vesicles are not strictly constant but can change by small amounts due to fluctuations. Membranes can deform in and out of the plane, with the lowest energy deformations usually due to bending and involving only the curvature. The extreme softness (very low bending moduli) of lipid bilayers leads to excitation of pronounced bending undulations. In equilibrium, they are purely thermal in origin but non-equilibrium contributions can arise due to complex proteins (*e.g.* ion channels and pumps) embedded in the lipid bilayer. The friction caused by coupling of the undulations to hydrodynamic flows in the surrounding aqueous medium strongly overdamps the fluctuations.

To calculate the fluctuation amplitudes, we consider a patch of membrane of dimension LxL. We describe any deflection $u(r,t)$ of the membrane as a superposition of plane waves with wavelength $2\pi/q$ where q is the wave vector. The bending energy is then a sum over all squared amplitudes of the individual modes of excitation:

$$F = \frac{1}{2}\sum\left[K_c {u_q}^2 q^4 + \sigma {u_q}^2 q^2\right]L^2, \tag{1.10}$$

where u_q is the Fourier transform of $u(r,t)$, and σ is the lateral tension arising due to the fixed area constraint of vesicles. Since each mode corresponds to a degree of freedom of the membrane, by the Equipartition Theorem the average energy per mode is $\frac{1}{2}k_BT$. Therefore the mean squared amplitude of the fluctuations is:

$$\langle {u_q}^2 \rangle = \frac{k_BT/L^2}{K_c q^4 + \sigma q^2}. \tag{1.11}$$

The amplitudes are small for small wavelengths (large q), and the long wavelength fluctuations dominate.

Biological membranes are not simple lipid bilayers but consist of a complex mixture of different kinds of lipids and proteins interacting with the cytoskeleton and

the extracellular matrix. Interactions of fluctuating membranes with polymers [98], microtubules [99] or actin shells [100] couple the curvature tension and the bending elasticity of the membrane with to rheological properties of the polymers. Biological membranes are clearly non-equilibrium structures. Manneville *et al.* [101] provide experimental evidence of the effect of the activity of transmembrane proteins on shape fluctuations of lipid membranes. Non-equilibrium features like vesicle movement under external forces can model cell movement. Cantat *et al.* [102] have studied vesicle dynamics induced by an adhesion gradient using a hydrodynamics approach by considering the coupling of the flow within the membrane to the bulk fluid.

We compare a cell in an aggregate of other cells to a vesicle in liquid. Cell membranes deform due to cytoskeletal activity (instead of the temperature induced fluctuations of vesicles) and the effective viscosity of the surrounding tissue opposes the relaxation of the membrane. Analysis of cell membrane fluctuations using the theory for vesicles can give us important insights into the role of the various physical parameters.

1.8 Research Outline

At the coarsest level of description, we can view tissues as liquids. They show similar properties and analogous behavior. At a finer level, the analogy breaks down - individual cell behavior in tissues depends on their finite size, deformability and strong intercellular interactions. At an even finer scale, we can describe each cell in terms of lipid vesicles. Can we formulate a consistent framework for studies of cells and tissues in terms of the various physical analogies? We must establish how far we can push the physical analogies, and where they must break down. To elu-

cidate the role of physics during morphogenesis and tissue rearrangements, we pick examples where we can simplify the picture and identify some local processes that resemble pure physical phenomena. We then try to model these processes using minimal physical parameters. Several simple *in vitro* experiments with developing tissues crudely mimic developmental processes and clarify certain aspects of biological development.

Our research has focussed on the quantitative study of some of the processes governing cellular rearrangement. The kinetics of cellular reorganization help establish a thermodynamic basis for the behavior of cells and define the limits of physical theories. In Chapter 2, we introduce a lattice based statistical mechanical model for simulating cell and tissue motion. Chapter 3 deals with experiments and modeling of cell sorting. In Chapter 4 we study tissue engulfment. In Chapter 5, we quantitatively characterize cell displacements and membrane fluctuations using methods from statistical mechanics. In Chapter 6, we characterize the tension in some intracellular membranes and investigate its role in membrane dynamics.

CHAPTER 2

POTTS MODEL SIMULATIONS

2.1 Introduction

Biologically motivated experiments identify details that do not necessarily explain their underlying mechanisms. An understanding of the essential features of a given phenomenon requires construction of a simplifying model. Most models try to formulate a minimal set of assumptions needed to quantitatively describe the experimental observations to a desired degree of accuracy. Mathematical models can show which experimental parameters are most important in determining a particular behavior.

One requirement of a good model is that the number of *ad hoc* assumptions or parameters should be minimal. The model parameters should be experimentally measurable quantities - both inputs to the model and outputs which can be tested. A powerful model should: (1) Simplify the picture to give a concise description. If a simple model mimics a highly complicated process, the model captures the essential features. This similarity should be both qualitative and quantitative. If the number of adjustable parameters in the model is too large, tweaking them can produce almost any result, reducing the usefulness of the model. (2) Have predictive power. The model should apply to situations where experiments haven't been done. The model's predictions should be able to guide future experiments which in turn can check the model's validity.

The principal usefulness of any theory is its predictions and, even if several theories can create similar patterns, we can distinguish them by the different experiments they suggest. Our goal is to implement a physical model with a minimal set of parameters that explains experimental observations of sorting, engulfment and cell motion.

2.2 Cellular Models

Of the numerous attempts to model cellular pattern formation phenomena like cell sorting, tissue engulfment, *etc.* most fall into two categories: 1) Cellular automaton models represent cells as one or more discrete units with rules to describe their interactions. These methods focus on individual cell properties such as cell adhesion and the number of neighboring cells. Physical and geometrical concepts such as energy, volume and contact angles are important and interactions are local. Differential adhesion is most conveniently implemented using cellular automata. 2) Continuum employ differential equations that describe the temporal and spatial variation of a "field" (concentration or force field). Cells are usually modeled as a density field. Effects can be long range. These models effectively describe global effects such as differentiation or cell movements in response to chemical fields (chemotaxis).

In the following, we briefly review some common models of biological pattern formation. We then compare the different approaches to motivate the particular model that we have chosen. The two prevailing views of pattern formation in embryology are the Turing chemical pre-pattern approach and the mechanochemical approach developed by Oster, Murray and colleagues.

2.2.1 Chemical Pre-Pattern Model

Alan Turing, in a seminal paper in 1952, proposed a dynamic mathematical developmental model [103]. He suggested that reaction-diffusion systems obeying physical laws could produce various stable patterns. A set of chemical substances, called morphogens, reacting with each other and diffusing through tissue may account for morphogenesis. Spatially inhomogeneous patterns can evolve by a diffusion driven instability or Turing instability, when two morphogens diffuse with different diffusion constants. Even minor fluctuations in uniform concentrations of morphogens could lead to such instabilities. Murray [104] gives several examples of the Turing reaction-diffusion approach to modeling pattern formation, such as animal coat patterns, hair patterns in *Acetabularia* whorl, and head and tentacle formation in *Hydra*. In the chemical pre-pattern approach, pattern formation and morphogenesis take place sequentially. First the chemical concentration pattern develops, then the cells sense it and differentiate accordingly.

2.2.2 Mechano-Chemical Model

The mechanochemical approach considers the role that mechanical forces play during morphogenetic pattern formation. Pattern formation and morphogenesis occur simultaneously as a single process. The chemical patterning and the form-shaping movements of the cells interact continuously to form the desired spatial patterns. Such mechanisms have the potential for self correction. Embryonic development is usually stable with the embryo compensating for many external disturbances. Mechano-chemical models depend on measurable quantities such as cell/matrix densities, traction forces, tissue deformation, *etc.*, and are very amenable to comparison with experiments at least in principle. The dynamics of these models results in stable

states (static or dynamic patterns) which mimic the stability of embryonic development to perturbations. The following quote from Wolpert [105] provides a clear justification for the need for a mechanical approach: "It is clear that the egg contains not a description of the adult, but a program for making it, and this program may be simpler than the description. Relatively simple cellular forces can give rise to complex changes in form; it seems simpler to specify how to make complex shapes than to describe them."

One of the earliest examples of the use of a mechanochemical model is the work of Odell *et al.* [106]. Their model explains the folding of embryonic epithelia. They observed that if a cell that was part of a ring or layer contracted, it would stretch the other cells in the layer. They hypothesized that stretching the cells beyond some point induced a contraction resulting in a smaller than original apical surface with the volume remaining constant. This cascade effect of reduction in apical surface would cause a buckling in the cell sheet producing an invagination, which resembles gastrulation in the sea urchin, ventral furrow formation in *Drosophila*, and neurulation in amphibians. They also emphasized the importance of not assigning to each cell an autonomous (genetic) program of shape change which would be evolutionary implausible.

Pattern formation takes place even in the absence of specific morphogens and chemical gradients. Movement of cells requires a guiding mechanism and a driving force. Cell-cell surface adhesion can provide both, as discussed in Chapter 1.

2.2.3 Vertex and Center Models

Several models have attempted to simulate surface energy driven cellular patterns using discrete cellular automata. Early models had point-like cells (consisting of a single lattice site) rearranging on a lattice [107, 108, 109]. Later modifications

have taken into account the geometry and topology of the patterns [110, 111, 112], long range effects of surface tension [113] and forces between cells using molecular dynamics simulations [114]. Dirichlet domains or Voronoi polygons represent cells. A cell is labeled by a center and defined as the subset of the space that is closer to it than to all other centers. Domains are convex and cover the space. In a center model, the dynamics are specified artificially as a function of the fictitious centers [115]. In vertex models, the membrane follows a set of slowly relaxing vertices [40]. Such models allow flexible cell shapes as in simulations of *Fundulus* epiboly [40], but are not able to define intercellular gaps or free surfaces.

The dynamics in the vertex and center models depend on the local force balance. Forces are introduced on the boundaries and the models simulate cell motion, shape changes and neighbor exchange but are realistic only for tightly packed tissues with no free boundaries. No geometrical model can consistently describe both two- and three-dimensional loose and compact aggregates. Instead we choose a statistical mechanical description to specify an energy on a lattice, which allows us to model arbitrary shaped cells and aggregates. The Potts model, which we describe next, successfully describes cellular patterns, treating gaps and free boundaries in a natural way.

2.2.4 Potts Model

In 1952, Potts introduced the Potts model as a generalization of the Ising model to more than two components [116] with discrete degenerate spin values. In the early 1980's, the Q-state Potts model was developed to study cellular pattern coarsening in metallic grains [117]. The interior of a grain consists of a lattice of atoms (spins), and the grain boundaries are the interfaces between different types of atoms or different crystal orientations. Each site on the lattice has a spin σ. A domain with

the same σ values defines a grain or bubble and each grain has a different spin. A free energy proportional to the total area of grain boundary defines a surface energy on the lattice and the Potts model minimizes the total surface energy. The interaction energy is zero for like spins and one for unlike spins. The total energy is the Potts Hamiltonian:

$$H = \sum_{i,j}[1 - \delta_{\sigma(i)\sigma(j)}], \tag{2.1}$$

where i and j are neighboring lattice sites. The model also describes coarsening in soap froth [118, 119].

The hexagonal pattern of two-dimensional arrays of soap bubbles of equal area resembles a cell sheet [120]. Surface tension driven boundary length minimization takes place both in soap froth and tissues. An important difference is that cells have a finite length cutoff - given by the cell size. Soap froth has unconstrained bubble areas. Like bubbles, biological cells have an elastic surface and bulk compressibility. Unlike bubbles, cell membranes do not merge during rearrangement. In biological patterns, a constraint on cell size stabilizes cells and introduces a characteristic length scale. The cytoskeleton regulates membrane rigidity and can cause anisotropy in cell shape. Viscosity and elasticity also depend on the time scale of the applied forces [39]. Further, the energies on the cell boundaries depend on the particular cell types. In the next section, we extend the Potts model to simulate biological cells.

2.3 Extended Potts Model

Glazier and Graner [121] extended the Potts model to include area constraints to fix cell sizes and type-dependent boundary energies (adhesion energies) to simulate differences in adhesion molecules. Minimization of the total adhesion energy drives

the evolution. Since we use this model extensively in our work, we describe it below in more detail.

2.3.1 Adhesion Energy

As discussed in Chapter 1, differential cellular adhesivity can direct the movement of cells. Cells stick to each other with the help of adhesion molecules distributed on their surfaces, and have a free energy associated with cell-cell contacts which reversibly attach or detach during cell rearrangement. The **adhesion free energy** $F(A) - F(0)$ is the integrated mechanical work between the attached state, with contact area A, and the separated state. The **surface free energy** J between two surfaces is defined as the adhesion free energy per unit contact area: $\partial F/\partial A$. It is equal to the reversible work required to increase the surface by a unit area. For sticky cells J is negative: F decreases when cells adhere. A surface free energy can also be defined with an external medium (for example, culture medium, air, substrate and extracellular matrix [19]). We can assign a potential energy to a cellular pattern if the adhesion energy is proportional to the contact area between the two cells. The local energy gradient drives cells as long as microscopic thermal fluctuations allow adhesive links to break and re-establish.

To formalize the notion of adhesive energy for a cell aggregate, we consider the total adhesion energy. We can write the total adhesion energy E_{adh} associated with a given configuration as a sum over cells $i = 1, ..., N$ or over cell pairs (i, j):

$$E_{adh} = \sum_{(i,j)} A_{ij} J_{ij} + \sum_{i} A_{iM} J_{iM}, \tag{2.2}$$

where A_{ij} denotes the contact area between cells, A_{iM} the contact area with the external medium and J_{ij}, J_{iM} the surface energies of these interfaces. For a heterogeneous aggregate of two cell types d and l, we can write equation 2.2 in terms of

macroscopic quantities summed over all the cells:

$$E_{adh} = \gamma_{dM} I_{dM} + \gamma_{lM} I_{lM} + \gamma_{dl} I_{dl} + \sum_{allcells} A_i \frac{e_{ii}}{2}, \tag{2.3}$$

where I_{dM}, I_{lM} and I_{dl} are the total interface areas. The surface energies, J_{ij}, relate in the following way to define the three relevant surface/interfacial tensions [122, 4]:

$$\gamma_{ld} = J_{ld} - \frac{J_{dd} + J_{ll}}{2}, \tag{2.4}$$

$$\gamma_{lM} = J_{lM} - \frac{J_{ll}}{2}, \text{ and} \tag{2.5}$$

$$\gamma_{dM} = J_{dM} - \frac{J_{dd}}{2}. \tag{2.6}$$

The surface tensions are not equivalent to a biological membrane's internal tension which appears as part of the volume constraint λ (defined in Section 2.3.2) and the surface area constraint Λ (defined in Section 2.5). The surface tensions represent the difference in energy between heterotypic and homotypic interface per unit area of membrane (or lattice bond). These relative costs do not change if we add a given constant to J_{ij} and $J_{ii}/2$.

We can, in principle, experimentally measure the surface energies J_{ij}, but not derive them from microscopic mechanisms (for discussion, see [19], [123]). The hierarchy of the J_{ij} determines the effect of cell adhesion; the relative values of the J_{ij} determine the actual minimum energy configuration obtained, while their absolute values and the dissipation only affect the time scale of the relaxation.

Cells in a pattern move down the local energy gradient. During cell sorting, the energy gradient is not entirely smooth, *i.e.* on the way to global energy minimization, cells and cell clusters have to move through transient states that have a higher configuration energy than the previous state. The cells have to traverse local minima in the energy to finally reach the global minimum. An aggregate of cells with a group of well rounded clusters represents a local minimum. To further

lower the energy the clusters have to deform in order to move and coalesce, thereby raising the energies of the intermediate steps. Cells move with the help of membrane deformations which enable them to escape from the local minima.

The surface energies determine the local roughness of the energy landscape and the dynamics, the surface tensions describe the configurations with absolute minimum energy *i.e.* the stable equilibrium states. Figure 2.1 shows schematic examples of each typical case. When γ_{dM} and γ_{lM} are negative, cells do not aggregate. In most cases, the surface tensions γ_{dl}, γ_{dM} and γ_{lM} are positive. The minimum energy occurs when the cells demix to form two homotypic clusters. The two clusters are in contact together and with the medium. The three interfaces form spherical caps and meet along a triple line (circle) of contact. In the plane normal to the edge, the three surface tensions considered as vectors along the interface, add to zero at equilibrium, obeying the Young condition (explained in more detail in Chapter 4, Figure 4.2), which fixes the contact angle at the interface.

Any equilibrium must satisfy the Young condition. If one surface tension is greater than the sum of the two others, no triple intersection can be stable and the more energetically costly interface disappears. If $\gamma_{dM} > \gamma_{dl} + \gamma_{lM}$, the dark-medium interface disappears and the light cells surround a single dark cell cluster, a typical cell sorting case, which we shall study in more detail in the following chapter. In this situation, the inequality $J_{dM} - J_{dl} > J_{lM} - J_{ll}$ constrains the surface energies.

2.3.2 Energy Hamiltonian and Dynamics

We simulate surface energy driven cell motion as in the regular lattice based Potts model. A spin $\sigma_{i,j,k}$ characterizes each lattice site and the domain which includes all lattice sites having the same spin constitutes a cell σ (Figure 2.2). Each cell has an associated cell type $\tau(\sigma)$, for example, neural retinal and pigmented

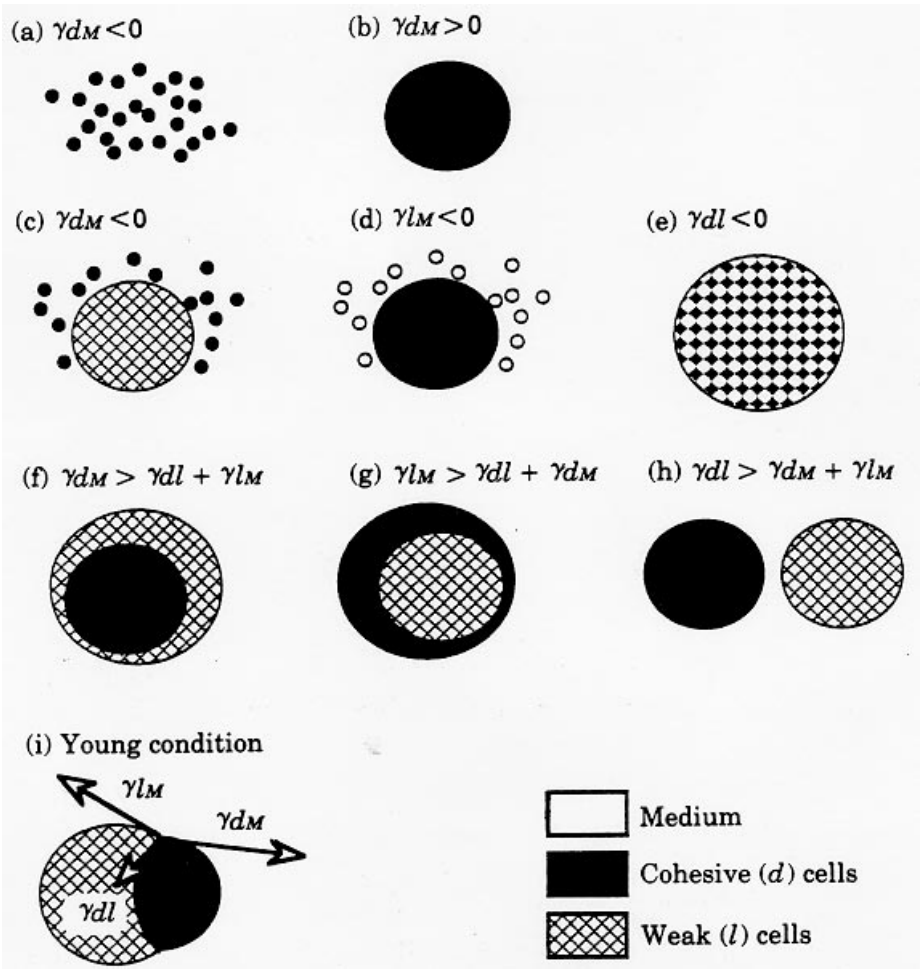

Figure 2.1. Surface tensions determine the equilibrium configuration with minimum global energy (from [4]).

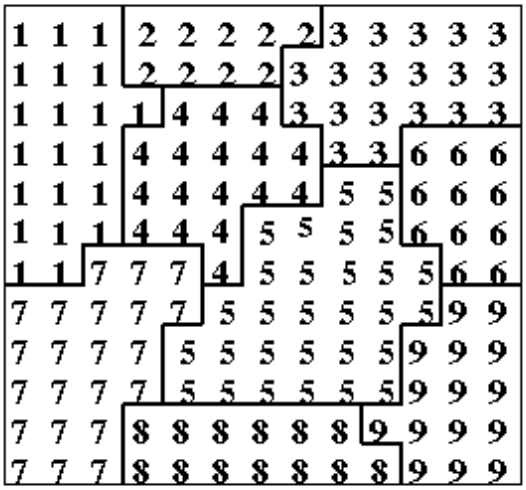

Figure 2.2. Diagram showing the lattice pattern for a two-dimensional Potts model simulation. The numbers show spin values at each lattice site. All sites having the same spin constitute a cell; the thick lines are the cell boundaries.

epithelium in chick embryo. Bonds between like spins have zero energy, that is, the energy inside a cell is zero. Bonds between unlike spins (at cell boundaries) have a cell type dependent surface energy $J(\tau, \tau')$. In addition, biological cells have a fixed range of sizes which we include in the form of an elastic constraint with elastic constant λ, and a fixed target volume, $V(\tau)$, which depends on the typical size of the particular cell type.

In this description of the cell, all lattice sites belonging to a given cell are identical. The cell membrane and cytoskeleton have no independent existence. The membrane is the boundary between two cells. Coupling strengths are distributed uniformly over the cell surface, so we cannot model inhomogeneities appearing in the cell at a microscopic level, *e.g.* inhomogeneous distribution of adhesion molecules on the cell membrane and changes in membrane properties due to the polymeriza-

tion of cytoskeletal actin. Further, we do not take into account time-dependent adhesivities.

We define the total pattern energy of the cell configuration as the sum of the contact adhesion energies and volume constraints:

$$H = \sum_{i,j,k} \sum_{i\prime,j\prime,k\prime} J(\tau(\sigma), \tau(\sigma'))(1 - \delta_{\sigma,\sigma\prime}) + \lambda \sum_{\sigma} [V(\tau(\sigma)) - v(\sigma)]^2 \qquad (2.7)$$

where $v(\sigma)$ is the volume of a cell σ. Large deviations of the cell volume from the pre-assigned target volume $V(\tau(\sigma))$ increase the configuration energy via the second term. Our code neglects the volume contribution for any cells with zero target areas. The volume constraint, therefore, enables the cells to conserve volume and encodes all bulk cell effects, *e.g.*, membrane elasticity, cytoskeletal properties and incompressibility. Thus, the energy is the sum of local membrane contact energies and volume energies associated with membrane elasticity and osmotic pressure. Because of the surface energy term, each cell usually contains slightly fewer than $V(\tau)$ lattice sites. We set the target area V_M of the culture medium to be zero, which in our code leaves the volume unconstrained.

Because we are dealing with a square lattice, the surface energy per unit boundary length depends strongly on the orientation (anisotropy). The ratio of the highest to lowest surface energy as a function of orientation measures the anisotropy. Increasing the range of interaction reduces this ratio [119]. For the simulation, we employ a third-nearest-neighbor square lattice to reduce the effects of lattice anisotropy. The pattern evolves in a probabilistic manner (Monte Carlo dynamics) using Maxwell-Boltzmann thermodynamics. At each simulation time step, we select a lattice site (i, j, k) at random and propose a substitution between this lattice site and one of its neighbors (also selected at random). We accept the substitution with

the following success probability:

$$\Delta H \leq 0 \quad \rightarrow \quad P = 1, \tag{2.8}$$

$$\Delta H > 0 \quad \rightarrow \quad P = \exp(-\Delta H/T), \tag{2.9}$$

where ΔH is the increase in total pattern energy produced by the proposed spin change. This algorithm differs slightly from the standard Metropolis algorithm which allows arbitrary spin substitutions. However, the probability of a completely mismatched flip is so low that the change, besides being biologically realistic since the cells do not form disconnected patches, increases greatly the speed of the calculations without affecting the statistics [121, 124]. T corresponds to the amplitude of the cell membrane fluctuations, not the much smaller amplitude thermal fluctuations. So T is an effective fluctuation temperature and has nothing to do with the actual temperature of the tissues. We define one Monte Carlo step (MCS) to be as many time steps as there are lattice sites. Since we change only one spin at a time, the cells move gradually, rather than in jumps as in some previous models [115]. The cell center of mass executes a random walk with Maxwellian velocity distributions (as discussed in Chapter 5). The diffusion constant is proportional to the probability of spin flips. Therefore, we can see that cell mobility depends on both the temperature and the net energy gain. From the point of view of the simulation only the value of the ratio $\Delta H/T$ is important. Increasing the temperature is equivalent to decreasing the surface energies by the same factor.

Since we perform the simulations at nonzero temperatures, cells may not be simply connected. Further, cell boundaries may crumple if the boundary energy and temperature are comparable. The crumpling and dispersal are artifacts of the simulation and are not biologically realistic, therefore, we **anneal** for a few Monte Carlo steps at $T = 0$ before calculating any statistics or displaying the pattern.

Annealing gets rid of most of the disconnected regions and makes the cell boundaries compact.

Using the large-Q Potts model, we can describe cells as objects of finite size with measurable volume, surface area and boundary curvature - which translates to membrane shape. In the Potts model, relative contact energies and boundary curvatures drive all motion. The model is "realistic" in that the position and diffusion of membrane (boundaries) determine the dynamics, as they do for real aggregated cells. The model has some limitations. All lattice sites in a cell are equivalent. The membrane and cytoskeleton have no independent existence, the boundaries between cells define the membranes. The two terms in the Hamiltonian contain all cellular properties. We also assume cell isotropy *i.e* cell surface molecules like adhesion molecules are uniformly distributed over the cell surface. Further, we don't take into account time-dependent adhesivity, the appearance of cell polarity, or variations in membrane elasticity and cytoskeletal fluctuations.

As we describe in the next two chapters, we have used the Potts model to examine the effects of differential adhesion only, separately from chemotaxis, reaction-diffusion and cell differentiation. If the model can produce results analogous to experiments, we can conclude that differential adhesion is the main factor, and that the observed pattern formation requires no other cooperative phenomena.

2.4 External Field

To compare with experimentally observable fluid properties like viscosity, we need to measure the effective viscosity of the simulated cellular aggregate. Typically, we measure the viscosity of simple fluids by dropping a heavy object and measuring its terminal velocity. Here, we include in the Hamiltonian, a term for the effect of

gravity and cause a "heavy" cell to drop down within the aggregate:

$$H = H_o + g\Sigma y(\sigma_{i,j,k}) \tag{2.10}$$

The gravity acts only on a single cell in the aggregate. The cell moves down in the y-direction. We measure the average velocity of the cell as the mean distance covered over the number of Monte-Carlo steps.

The force due to Stokes' law gives the terminal velocity at which a sphere falls through a fluid:

$$\frac{4}{3}\pi a^3 \Delta\rho g = 6\pi\eta v a. \tag{2.11}$$

The effective viscosity in the simulations is proportional to the ratio between gravity and velocity. Plotting the velocity (v) versus applied gravity (g) thus gives us an estimate of the viscosity.

Figure 2.3 shows a plot of v *vs.* g for a typical aggregate. The graph is linear, the inverse of the slope being proportional to the viscosity.

We find that the effective aggregate viscosity (η) is highest for the most cohesive cell type (d in d) and lowest for the least cohesive type (l in l). The viscosity follows the hierarchy: $\eta_{dd} > \eta_{ld} > \eta_{dl} > \eta_{ll}$, consistent with our intuition that the more cohesive tissues will be more viscous since they possess stronger bonds that are harder to break. Qualitatively, experiments show the same ordering. Forgacs *et al.* conducted experiments to measure the viscoelastic properties of living tissues from chicken embryo [85]. They found that the most cohesive pigmented epithelial tissues had the largest viscosity and the least cohesive neural retinal tissues had the smallest viscosity.

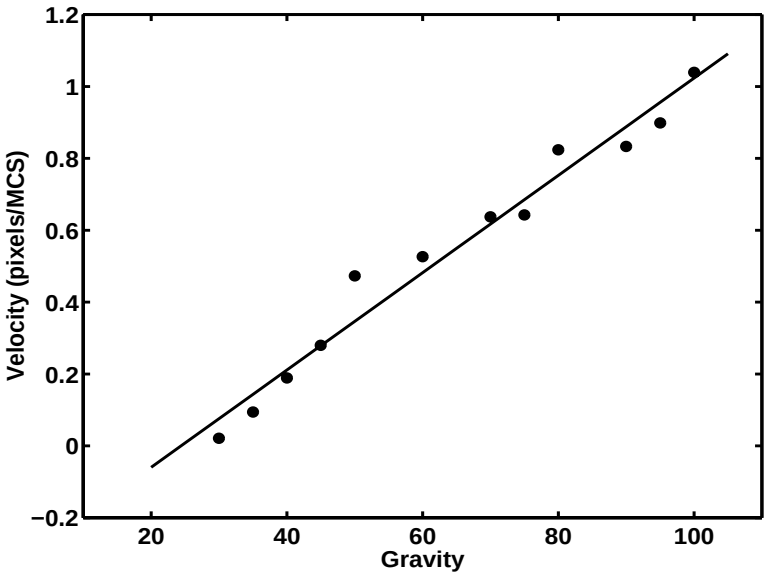

Figure 2.3. Graph of velocity *vs.* gravitational strength for a cell in a typical simulated aggregate. The solid line is a linear fit with slope $1.35\text{x}10^{-2}$ pix/MCS.

2.5 Negative Energies

The present model with the Hamiltonian from section 2.3 effectively captures the global features of tissue rearrangement, *e.g.* cell sorting, engulfment *etc.* It compares adequately with experiments, both qualitatively and quantitatively. However, it fails to describe correctly the dynamics of single cells moving within the aggregate as described in Chapter 5.

The surface energy values (J_{ij}), in the present model, are positive, so the cells can minimize their energy both by reducing their total surface area (becoming spherical or shrinking) and by forming more cohesive contacts. The surface energies thus perform a dual role - as adhesion energies as well as surface tensions of the cell membrane. These values are positive, and hence greater than the intracellular energy values (zero by definition). Surface energy values, therefore, define an inward compressive force on the cell surfaces rather than a binding with other cells. In order

to make the $J_{i,j}$s true binding energies, we have to assign them negative values. In real cells, surface isn't easy to create or destroy, whereas in the Potts model, it is. We therefore need to explicitly constrain the surface area of cells to prevent them from breaking up to increase the number of more adhesive contacts.

In the simulation, the most cohesive (dark) cells have the highest diffusion constant. When a spin flip involves a dark-dark boundary, the energy change is smaller than during a light-light boundary change: $\Delta E_{dd} < \Delta E_{ll}$. Therefore, the probability for an adverse change (fluctuation), $P = \exp(-\Delta E/T)$, is greater for dark-dark boundary changes, making the more cohesive cells more mobile. This hierarchy contradicts experimental observations in *Hydra* cells (see Chapter 3), where the most cohesive cells are the least mobile. This experimental hierarchy is intuitively more acceptable, as stronger adhesive bonds should be harder to break and hence inhibit cell motion.

One solution to the above problem is to use negative surface energy values and add another term to the Hamiltonian which separately constrains the surface area (perimeter in two-dimensions):

$$H = H_o + \Lambda\Sigma[S(\tau(\sigma)) - s(\sigma)]^2, \tag{2.12}$$

where Λ is an adjustable parameter (Lagrange multiplier) which determines the strength of the perimeter constraint, $S(\tau)$ is the target surface area and $s(\sigma)$ is the surface area of each cell. This term takes account of the fact that the area of the cell envelope remains roughly constant and Λ is the tension counteracting the membrane expansion. The J_{ij} values act only as coupling strengths. For a cell with volume $4/3\pi r^3$, we set the surface area greater than $4\pi r^2$ (for a rigid sphere) to allow cell deformations.

Simulations of cell sorting with the extended Hamiltonian 2.12 give the same qualitative equilibria as with the old Hamiltonian 2.7. However, the dynamics change: the rates at which the different cell types move depends on whether the energies are negative or positive (see Chapter 3 and Chapter 4).

2.6 Velocity Correlations

Experiments with *Hydra* cells have shown that cells within a tissue need not move diffusively [125], as observed for cells on substrates (which are diffusive beyond a persistence time). Within cellular aggregates of some types of tissues, we find that the velocity distribution is non-Gaussian and cell velocities are correlated (Chapter 5). Without any external correlations, the cells in the simulation diffuse randomly (like Brownian particles) and the velocity distributions are perfectly Gaussian (Chapter 5). To understand from a physical perspective, the source and effects of correlations observed in the experiments, we modified the Hamiltonian to introduce velocity correlations.

The modified Hamiltonian is:

$$H = H_o + \zeta\Sigma[U(\tau(\sigma)) - u(\sigma)]^2. \tag{2.13}$$

We introduce temporal correlations in the velocity by making the target velocity, $U(\tau(\sigma))$, at each step equal to the velocity at the previous step. $u(\sigma)$ is the instantaneous velocity of cell σ if we accept the proposed spin flip. The parameter ζ controls the strength of the velocity correlation term. If $\zeta = 0$ the velocity is uncorrelated and if $\zeta = \infty$, the trajectory is ballistic. We seek to understand whether temporal correlations can give rise to spatial correlations between the velocities of neighboring cells and to some unusual phenomena like spiraling. In experiments, we find both temporal and spatial correlations in cell velocities and non-diffusive

motion. Does the strength of temporal correlation affect the strength of spatial correlations and can it give rise to non-diffusive motion? Chapter 5 presents results using this modified Hamiltonian.

CHAPTER 3

CELL SORTING

3.1 Motivation and Previous Work

Certain classic experiments with chicken and *Hydra* cells show nearly pure differential adhesion driven cell sorting [2]. Dissociation of tissues into single cells destroys any long range chemical gradients. When we allow such a suspension of cells to aggregate, the cells reorganize into homogeneous tissues similar to those of normal embryos. According to the Differential Adhesion Hypothesis [33], the cells rearrange themselves into a configuration that minimizes their interfacial energy. However, the Differential Adhesion Hypothesis does not say anything about the dynamics of the energy minimization. Some basic questions remain to be answered. What is the time course of sorting? Can a physical model explain the dynamics?

The kinetics of cell sorting depends on the dynamical properties of cell populations. The intrinsic mobility of each subunit (a cell) and how it responds to external and internal stimuli from other cells, substrates, adhesion molecules and its own cytoskeletal apparatus determines the time-rate of sorting. As in liquids, the important quantities are viscosity, surface tension and the effective fluctuation temperature (assuming quasi-thermodynamic behavior). What are the limits to which the liquid analogies hold for biological tissues? In liquids, the smallest subunit is a microscopic molecule, whereas in tissues, it is a cell. How does the presence of the mesoscopic length scale of a cell modify the picture?

The finite size of cells can have the following effects: (i) Cells have a surface, which allows a position-dependent surface energy whose gradient drives motion. They have a well defined shape which causes geometrical constraints (like trapping within nearest neighbors), especially in multicellular environments like dense tissues. A cell has to displace some of its nearest neighbors in order to move past them. Sulsky *et al.* [115] present an evolution equation for an incompressible cellular pattern with a surface energy and derive the Stokes equation for an incompressible fluid. They find an additional non-differentiable term due to the cell topology. Its one-sided derivatives exist when cells exchange neighbors through a four-sided vertex (called $T1$ switch). This singularity has no equivalent in hydrodynamics. (ii) On microscopic scales, cells have several internal degrees of freedom which are not present in liquids. Moreover, a cell has an internal energy source which allow it to move actively by changing shape - it is "self driven". It can explore neighboring configurations with the help of membrane fluctuations in the form of contractions and protrusions. (iii) Thermal agitation is not enough to allow micron sized cells to explore ergodically the entire configuration space. Therefore, without active fluctuations, the final energy state can be a metastable local energy minimum.

Mombach *et al.* [5] compared cell sorting experiments to simulations. They found that the length of the heterotypic interface decreases logarithmically in time. In this chapter, we study in detail the kinetics of sorting experiments in chicken embryo and *Hydra* cells and compare it to physical models and simulations. We also characterized the growth of clusters to compare to a fluid model of phase separation. Sorting rates in *Hydra* has not been quantified before. We observed quantitatively two-dimensional images of the process of cellular reaggregation in three-dimensional

aggregates from embryonic and *Hydra* tissues. We verified that our experimental results agree with our computer simulations based on the DAH to limited accuracy.

3.2 Experiments

The main goal of our experiments was to obtain clean quantitative data on the time rate of sorting. We used tissues both from chick embryo and *Hydra*. We designed the experiments to observe only the effects of adhesion in different tissue types. Therefore, one main goal was to eliminate pre-existing chemical gradients to eliminate chemotactic effects.

3.2.1 Cell Sorting in Chicken

We used cells from chicken embryos because they are cheap and easily available compared to mammalian embryos and because the cells in the individual tissues remain adhesive and motile even after dissociation and reaggregation. We used cells from eyes (pigmented and neural retinal), liver and heart tissue. The neural retinal, liver and heart cells are translucent and therefore combining any of these two required fluorescent staining of one of the tissue types. In the first 6-8 days of development the eyes have only two cell types: neural retinal (translucent) and pigmented epithelial (almost black). A combination of pigmented and neural cells, therefore, provides a very good contrast for imaging with simple bright-field microscopy.

We conducted experiments on 6-8 day old chicken embryos using standard techniques [126] (see Appendix A for the full protocol). We separated the neural retinal and pigmented retinal layers from the eyes of chicken embryos and dissociated them into single cells. We mixed the two cell types in ratios ranging from 3 to 10 neural cells for one pigmented cell. The pigmented cells have typical volume of 5.8 times the volume of the neural retinal cells. The dissociation and random remixing de-

stroys any pre-existing diffusible chemical gradients [126]. We cultured the mixture in cell medium in a controlled temperature shaking water bath at 37°C. After 8-12 hr, when the cells adhered to form compact aggregates, we transferred some aggregates to be cultured singly in specially designed observation chambers. We observed the aggregates with an inverted optical microscope (Olympus IMT2). During observation, we maintained the culture flask at 37°C with the help of a heater and temperature sensor feedback mechanism. The microscope connected to a CCD camera (Hammamatsu C2400) which connected to an S-VHS Video Recorder and then to a computer. We monitored sorting by capturing images and digitizing at regular time intervals.

Figure 3.1 shows a few representative images. The images obtained from the experimental aggregates are two-dimensional vertical projections of a three dimensional structure. The aggregates ranged in diameter from 150 to 400 μm with 2 x 10^4 to 1 x 10^6 cells. Initially, the aggregate has a random distribution of neural (light) and pigmented cells (dark). After about 12 h, an external monolayer of light cells forms along the boundary of the aggregate and the dark cells partially sort into larger clusters. After about 72 hr, the aggregate becomes spherical with the neural retinal cells surrounding an internal core of pigmented epithelial cells. The experimentally measured surface tensions for pigmented and neural cell aggregates are 20.1 and 1.6 dyne/cm respectively, as discussed in Chapter 1 [3, 83]. Thus the behavior of the aggregate agrees with the surface tension values: just like in immiscible liquids, the tissue with lower surface tension (less cohesiveness) spreads over the more cohesive tissue, reflecting the dominance of differential adhesion.

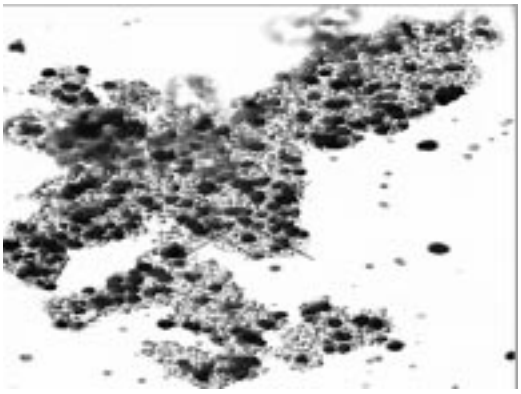

t = 5 hr

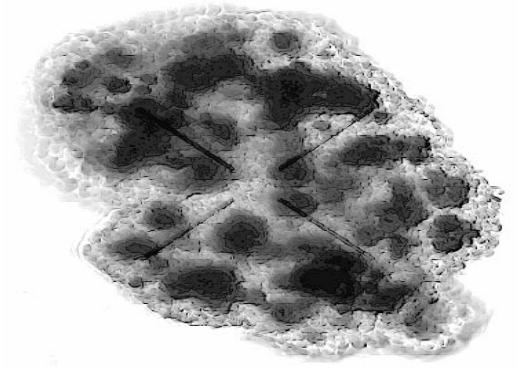

t = 10 hr

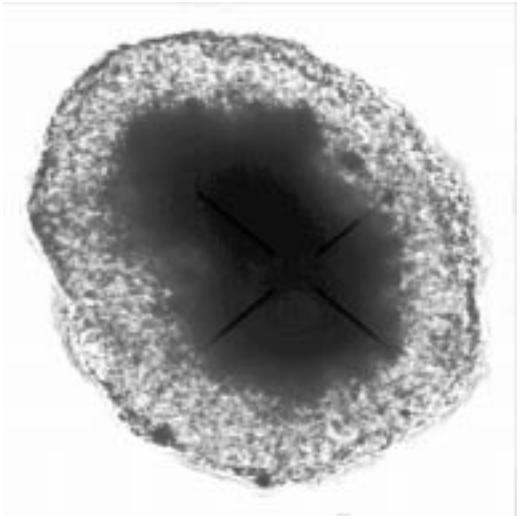

t = 72 hr

Figure 3.1. Cell sorting. Time sequence during the sorting out of two intermingled cell types from chick embryo: neural retinal (light cells) and pigmented retinal (dark cells). The final aggregate is 200μm in diameter.

3.2.2 Effect of Cytochalasin

One of the principal means of locomotion of vertebrate cells in tissue culture involves a "ruffled" or "undulating" membrane located at the advancing edge of the actively locomoting cell. Actin dynamics at the cell surface causes membrane ruffling or formation of lamellipodia [49, 53, 127]. These structures contain actin filaments undergoing polymerization-depolymerization cycles. The drug Cytochalasin-B reversibly inhibits the activity of the ruffled membrane and hence the motile activity of the cells [128]. Inhibition of locomotion is rapid and complete at concentrations of 1-10 μg/ml. The cytochalasins, a family of metabolites excreted by various molds, paralyze many kinds of vertebrate cell movement. The cytochalasins bind specifically to the fast growing plus-ends of actin filaments, preventing the addition of actin molecules there, and therefore membrane extension [129].

Are membrane fluctuations required for cells to reach the minimum energy configuration, or is cell rearrangement during sorting a passive process driven solely by the adhesion energy gradient? Observations of cell sorting in the presence of Cytochalasin can answer this question. Mombach *et al.* [5] studied the effect of Cytochalasin B on sorting. Aggregates placed in culture medium containing 10 μg/ml concentrations of Cytochalasin, sorted partially [5, 126], as seen in Figure 3.2. The dark cells did not sort out to the center of a spherical aggregate. Instead, they formed clusters in unrounded aggregates without an external light cell layer, presenting a local order very different from the global order found in the normal case. This arrangement of tissues resembles that found in control aggregates (no Cytochalasin-B) of intermediate stages of sorting. These observations show that membrane fluctuations are not essential for partial sorting but are required to reach the final state of global minimum energy.

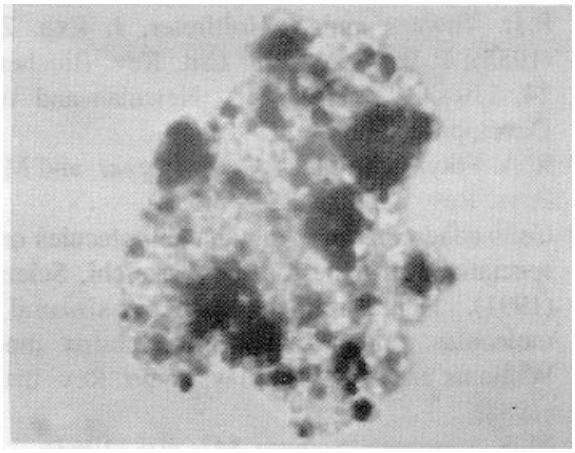

Figure 3.2. Partially sorted aggregate of neural retinal and pigmented retinal cells of chick embryos cultured in medium containing Cytochalasin-B. Image at 83 h after the start of aggregation. Adapted from [5]

However, several experiments show that the degree of sorting in the presence of Cytochalasin depends on the cell types employed. Cell sorting is completely inhibited in some tissue type combinations: chick embryo heart-pigmented retinal aggregates [126] or liver-heart combinations [130] (as opposed to the partial sorting described above). Inhibition may depend on the magnitude of the difference in cohesive strengths of the cell types employed. According to several experiments [35, 83], pigmented retinal cells are considerably more cohesive than neural retinal cells, but heart, pigmented retinal and liver tissues differ only slightly from one another in their strengths of cellular adhesion. The neural-pigmented pair, therefore, has a higher surface tension difference as compared to liver-heart and heart-pigmented pairs. One possible explanation for the absence of sorting with the latter cell type combinations could be that the differences in adhesiveness are too slight to result in observable sorting under conditions without active cellular locomotion.

Some evidence suggests that, in addition to affecting cell motility, Cytochalasin-B interferes with cellular adhesion by affecting some surface properties of the plasma

membrane. Sanger *et al.* [131] observed that cells from some embryonic tissues did not aggregate well or round up in the presence of Cytochalasin. Armstrong [126] and Steinberg [130] observed that Cytochalasin hampered the aggregation and rounding of chick embryo tissues, including neural retinal and limb-bud mesoderm to different extents. Steinberg also observed that fusion of two aggregates of the same tissue type did not proceed to completion. These observations suggest that the addition of Cytochalasin may change the absolute as well as relative surface tensions of tissues. The partial sorting could result from the combination of the two factors - inhibition of cell motility and changes in adhesion properties leading to changes in relative surface tension. We will discuss this issue in greater detail in light of our observations on tissue engulfment in Chapter 4.

In the case of partial sorting, the Young condition for surface tensions is satisfied, which is not true for an aggregate in normal medium. So, the ratios of the surface tensions must have changed. A light cell monolayer does not form, as both dark and light cells want to be in contact with the medium and with each other. Of course, the cell motility also has been inhibited, so clusters cannot move to reach the minimum energy state and dark cell clusters that are in the interior of the aggregate, are trapped.

3.2.3 Cell Sorting in *Hydra*

Hydra is a useful model because (i) It is a simple organism with only two main cell types. (ii) A dissociated and reconstituted mixture of *Hydra* tissues eventually regenerates to form a functional animal. For our studies on *Hydra* we use two species - *Hydra vulgaris* (or brown hydra) and *Hydra viridissima* (or green hydra). *Hydra* is a freshwater polyp with a very simple body plan. It consists of a cylindrical body column with two layers of cells (inner - **endoderm** and outer - **ectoderm**) sepa-

rated by extracellular matrix - **mesoglea**. Figure 3.3 shows a single *Hydra*. Green *Hydra* are very convenient because their endodermal cells auto-fluoresce, eliminating the need for any kind of fluorescent labeling. Cell aggregates of *Hydra* made by dissociating the tissues into a suspension of single cells and then reaggregating them by centrifugation can regenerate a complete adult in one week [64], illustrating the re-establishment of morphology at the cellular and tissue level.

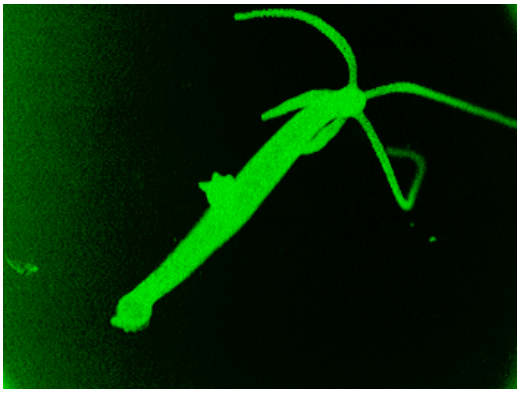

Figure 3.3. Adult *Hydra* (*Hydra viridissima*). Cylindrical body column with two layers of cells. Inner layer - **endoderm**; outer layer - **ectoderm**. The endodermal layer is autofluorescent. The body is about 1mm in width.

In the first 12 hours the aggregate rounds up to form a spherical aggregate with the ectodermal and endodermal cells sorting out to form layers. Within 24 to 72 hours this bilayer separates from the rest of the cells in the interior which are expelled to form a cavity. Qualitative changes in the contact surfaces between individual cells, the formation of mesoglea between the layers [132] and the appearance of gap junctions and other junctions within the endodermal and ectodermal monolayers [133] probably stabilize the cavity. In the next three to four days, multiple heads start forming on the aggregate. The aggregate eventually elongates behind each head and separates out into individual *Hydra*.

The regeneration of *Hydra*, in some ways, resembles embryogenesis in higher animals. Formation of an internal cavity surrounded by an epithelial sheet is analogous to formation of the blastocoel in an embryo, which later undergoes gastrulation. Morphogen gradients can organize complex patterns of cell responses during morphogenesis. *Hydra* tissues also secrete chemical morphogens which establish a spatial structure. Reaction-diffusion mechanisms, which lead to the formation of complicated patterns in higher animals, may be responsible here for breaking the spherical symmetry of a *Hydra* aggregate and elongating the body column. As in other animals, *Hydra* cells differentiate into multiple types. The formation of tentacles may be analogous to the extension of digits in vertebrate limbs [104] and with dendrite growth in neurons, which may result from instabilities in certain types of reaction-diffusion models [134]. *Hydra* tissues are also very good models for wound healing studies. Living *Hydra* have immense regenerative properties - they heal regardless of how they are cut, incised or injured. They can demonstrate cell movements and the effect of different chemicals during healing. A basic understanding of structure formation in *Hydra* will be invaluable to the study of more complex organisms.

For cell sorting experiments, we use normal *Hydra vulgaris* maintained in a disease free culture at 18°C. We dissociate several whole animals into single cells and reaggregate them using the standard protocol described in Appendix B. We observe aggregates and take time-lapse images for the first 12 hours. Figure 3.4 shows the time evolution of the mixed aggregate. As before, we see the entire aggregate rounding up and endodermal cells clustering to the inside of the aggregate. The imaging procedure for aggregates from both kinds of *Hydra* is exactly the same as in chicken experiments. All the images are two-dimensional projections of the actual three-dimensional aggregate.

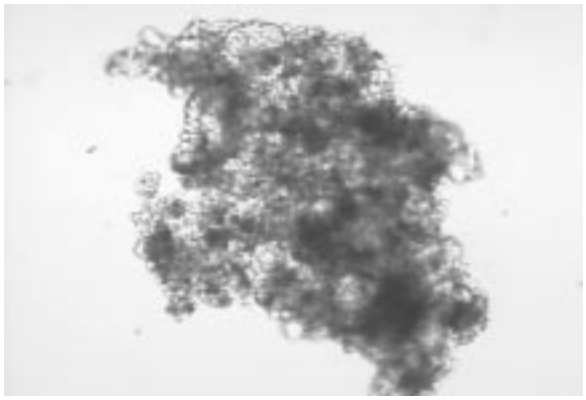

t = 0 min

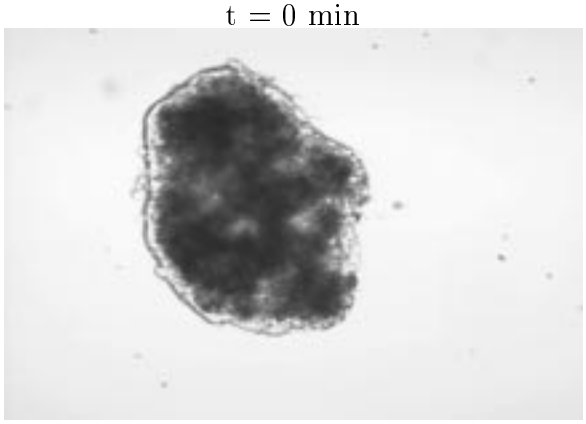

t = 123 min

t = 1213 min

Figure 3.4. Time sequence of cell sorting in three-dimensional *Hydra* tissues during regeneration. The dark cells are endodermal and light cells are ectodermal. The last aggregate is 380 μm long and contains a partially formed cavity.

Rieu *et al.* [6] have observed *Hydra* cell sorting in flat quasi-two-dimensional aggregates. The two-dimensional setup allows for clearer visualization of individual cluster shapes and dynamics. Figure 3.5 shows cell flows during sorting of endodermal and ectodermal cells. We see that displacements of nearest neighbors show correlations and cells move as coherent groups. The coherent motion leads to internal rounding of the endodermal clusters and circular flows of ectodermal cells around endodermal clusters. When two dark clusters come close enough to coalesce, they must squeeze out the intervening light cells. These studies show the presence of hydrodynamic-like flows in cellular aggregates and reinforce the analogy with liquids. Presumably, similar mechanisms are at work even in three-dimensional aggregates. However, the two-dimensional experiments do not lead to the formation of a single internal endodermal cluster [6]. Several separate endodermal clusters persist possibly due to the reduced freedom of motion in two dimensions.

Recently, Kataoka *etal*. [7] imaged the entire three-dimensional process of sorting using Magnetic Resonance Imaging (MRI) techniques. Figure 3.6 shows the time sequence of MRI images of a regenerating cell aggregate. The quantitative dynamics are similar to the two-dimensional case, discussed in the next sections.

3.3 Image Analysis

We captured images from the microscope using S-Video and then digitized them. Image analysis used a combination of MATLAB and FORTRAN programs. We used histo-equalization and thresholding to select **dark**, **medium** and **light** regions corresponding to the two cell types and culture medium (with intensity values 0, 128 and 255 respectively). To find the boundary between the dark and light cell regions, we used the criterion that the intensity profile of the digitized image should have

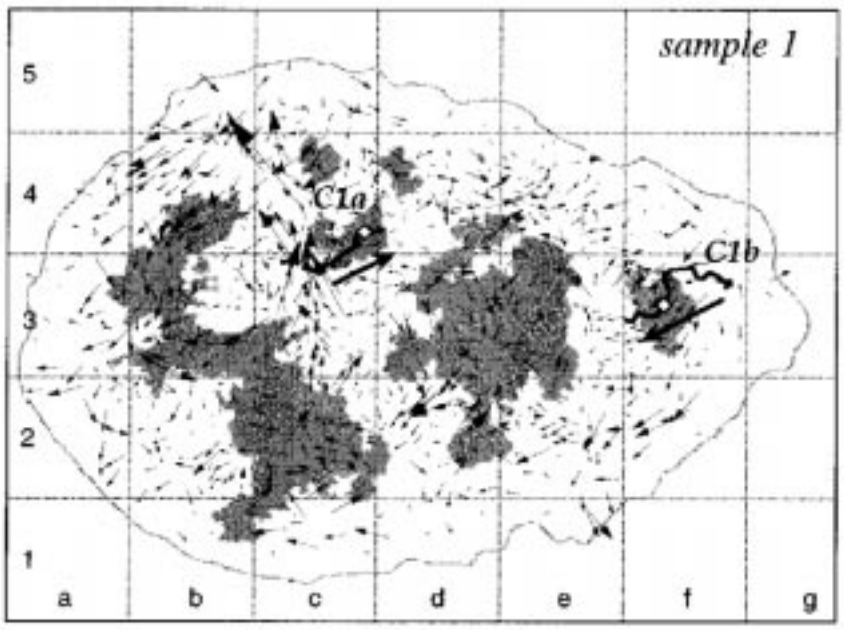

Figure 3.5. Cell displacements during cell sorting in a two-dimensional *Hydra* aggregate. The dark patches are endodermal cells and the outer curve denotes the boundary of the ectodermal aggregate. Arrow sizes are proportional to cell displacements during the time interval 120-150 min after aggregate formation. Adapted from [6]

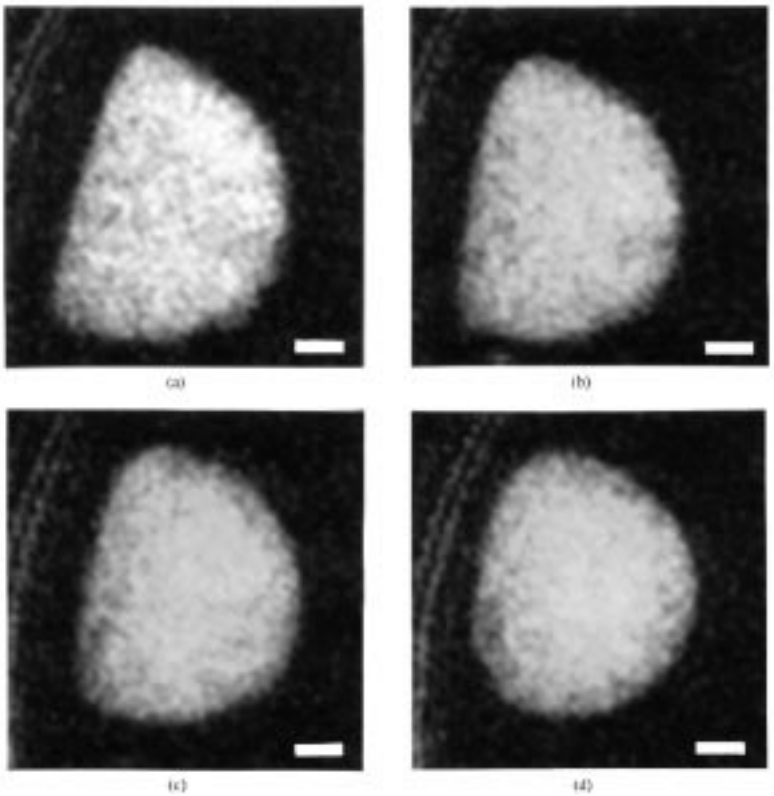

Figure 3.6. Time series of MRI images of a three-dimensional regenerating *Hydra* aggregate. (a) 15 min, (b) 30 min, (c) 60 min, (d) 240 min. Scale bar is 200 μm. The resolution is 5 μm x 5 μm in the horizontal plane and 50 μm in depth. Adapted from [7]

the largest slope at the boundary. Figure 3.7(b) shows a typical intensity profile across a row in the image of an aggregate in Figure 3.7(a). We calculated the local slope at each point across the profile and chose the points with maximum slope as the boundary. We then used a boundary tracing algorithm implemented using FORTRAN and MATLAB to locate the dark-light, dark-medium and light-medium boundaries. The program also determined areas, radii of gyration of dark clusters and number of clusters at every time step.

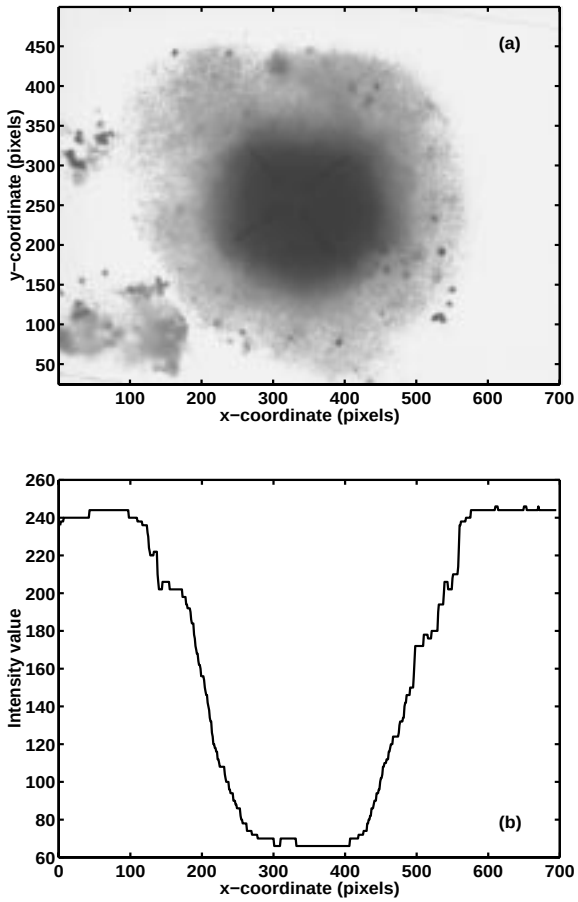

Figure 3.7. Discrimination of dark-light interface. (a) Image of a typical aggregate (pigmented and neural retinal cells). (b) Intensity profile across a row (y = 250) within the image matrix

3.4 Simulations

We have simulated cell sorting using the extended large-Q Potts model on a cubic 100^3 element lattice to compare quantitatively with experimental results. These simulations used positive surface energies and the Hamiltonian of Equation 2.7. (In this section, we describe our initial simulations, in Section 3.6 we present the results from more sophisticated simulations using negative surface energies). We defined two cell types, more cohesive cells with less surface energy referred to as dark (d), and less cohesive cells with more surface energy or light (l) cells. The light cells represent neural retinal cells from chick embryo or ectodermal cells from *Hydra*. The dark cells represent the pigmented retinal cells from chick or endodermal cells from *Hydra*. In addition, we also simulate a surrounding fluid medium as a single cell of another cell type (M) with zero target area so that it has an unconstrained volume. Thus the cell type parameter $\tau(\sigma)$ can have three values *d, l, and M*. To eliminate fragmentation of cells, we anneal the simulation briefly at $T = 0$ before calculating statistics.

For complete sorting, the tissue interfacial tensions are constrained by the equation [83]:

$$\sigma(d,d) > \frac{\sigma(d,d) + \sigma(l,l) - \sigma(d,l)}{2} \geq \sigma(l,l). \tag{3.1}$$

The surface energies must accordingly obey the inequalities:

$$0 < J_{dd} < \frac{J_{dd} + J_{ll}}{2} < J_{dl} < J_{ll} < J_{lM} = J_{dM}. \tag{3.2}$$

The values of surface energies assigned to the cells and medium are: $J(1,1) = 7$; $J(1,2) = J(2,1) = 5$; $J(1,3) = J(3,1) = 8$; $J(2,2) = 2$ and $J(3,3) = 16$. These result in surface tension values of $\sigma(l,l) = 4.5$ for the light-medium interface, $\sigma(d,d) = 7.0$ for the dark-medium interface and $\sigma(d,l) = 0.5$ for the dark-light interface,

yielding a ratio between light-medium and dark-medium interfacial tensions of 0.64. The experimental surface tensions for liver and heart cell aggregates from chick embryo are 4.3 $\pm$ 0.1 and 8.3 $\pm$ 0.1 dyn/cm respectively, which yield a ratio of about 0.52 [85, 83]. The ratio for *Hydra* ectoderm and endoderm is estimated to be 0.6 [135]. However, heterotypic tissue interfacial tensions (*e.g.* dark-light) have not been measured experimentally.

We measure the fractional boundary lengths which depend on the relative sizes and numbers of the different cell types. We therefore set the relative cell sizes in the simulation equal to the experimental values. Neural retinal cells (in spherical form) have an average diameter of ~ 5 μm (± 0.3 μm) and the pigmented retinal cells ~ 9 μm (± 1.6 μm), which yields a volume ratio of ~ 5.8. (Although cells are not entirely spherical in the aggregate, the volume ratio still holds). In the simulation too, we set the ratio of the target volumes of light and dark cells to 5.8 with light cells having a typical target volume of 100 sites and dark cells having a volume of 580 lattice sites. We set the volume constraint parameter to be $\lambda = 1$. To simulate normal sorting we set the fluctuation temperature $T = 32$, giving typical fluctuations of $\sim$1 lattice site corresponding to experimentally observed fluctuations of about 1 μm for *Hydra* cells of 5-10 μm diameter [125].

To compare with the same quantity as in the experiment, we project the aggregate onto a plane by scanning the columns of the three-dimensional matrix. A column with at least one dark cell generates a dark site on the projected plane, a column with only lighter cells generates a light site and a column with only medium generates a medium site. With this algorithm, all dark cells in the aggregate are visible. This method fairly closely approximates the experiments, as the light cells

are translucent and the aggregates small. Figure 3.8 shows projections of a three-dimensional aggregate at successive times in the simulation.

Figure 3.9 shows a two-dimensional simulation on a small lattice with all the cells and cell boundaries visible. We can see clearly that cell boundaries are represented quite realistically and observe the shape changes as cells move and exchange neighbors. The aggregate remains spherical. In general, the two-dimensional simulation of sorting is slower than the three-dimensional simulation because fewer degrees of freedom result in trapping of heterotypic cells. In three dimensions, cells are free to move in all directions and contact is not restricted to a plane.

3.5 Results and Comparison

We simulated cell sorting using an initial configuration of two randomly intermixed cell types and compared the results with the experiments. In Figure 3.10, we reproduce the time evolution of the boundary lengths of normal and partial sorting respectively. Points represent the average of 2-6 different aggregates. We rescaled the time in the simulation to real time in the experiment by the best coincidence between order parameters at early and late stages. These results show that the time scale for sorting is logarithmic. In normal sorting, the light-dark boundary decreases as both cell types segregate, while the light-medium boundary increases and the dark-medium boundary decreases to zero as a result of the formation of the light cell layer, until they reach plateaus once the aggregation is complete (*i.e.* the cells have sorted out and the aggregate as well as the inner core of dark cells has rounded). The formation of the external monolayer of light cells is much faster (10 hr) than the characteristic time scale for complete sorting (72 hr).

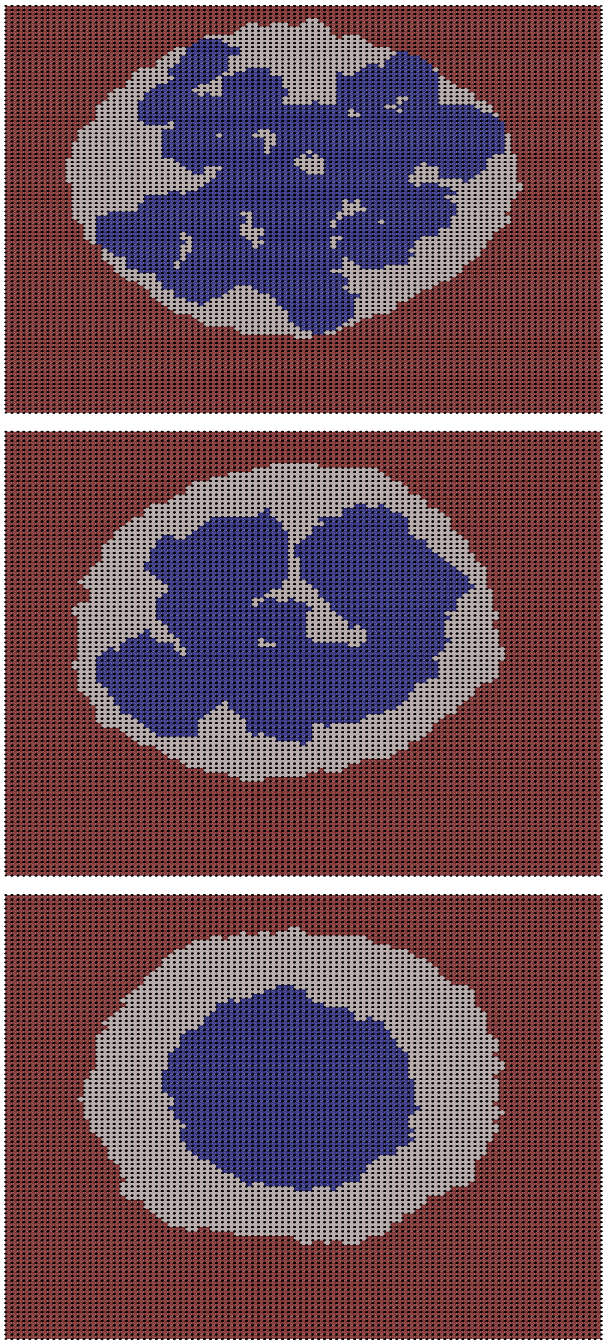

Figure 3.8. Simulation of cell sorting for dark (more cohesive) and light (less cohesive) cells. The figures show a two-dimensional projection of a three-dimensional aggregate at times 10 MCS, 1000 MCS and 8000 MCS from top to bottom. The lattice size is 100x100x100 pix^3, each dark cell is about 8 pix in diameter, and the temperature is T = 32. The outer dark region is medium. We do not show light-light or dark-dark cell boundaries.

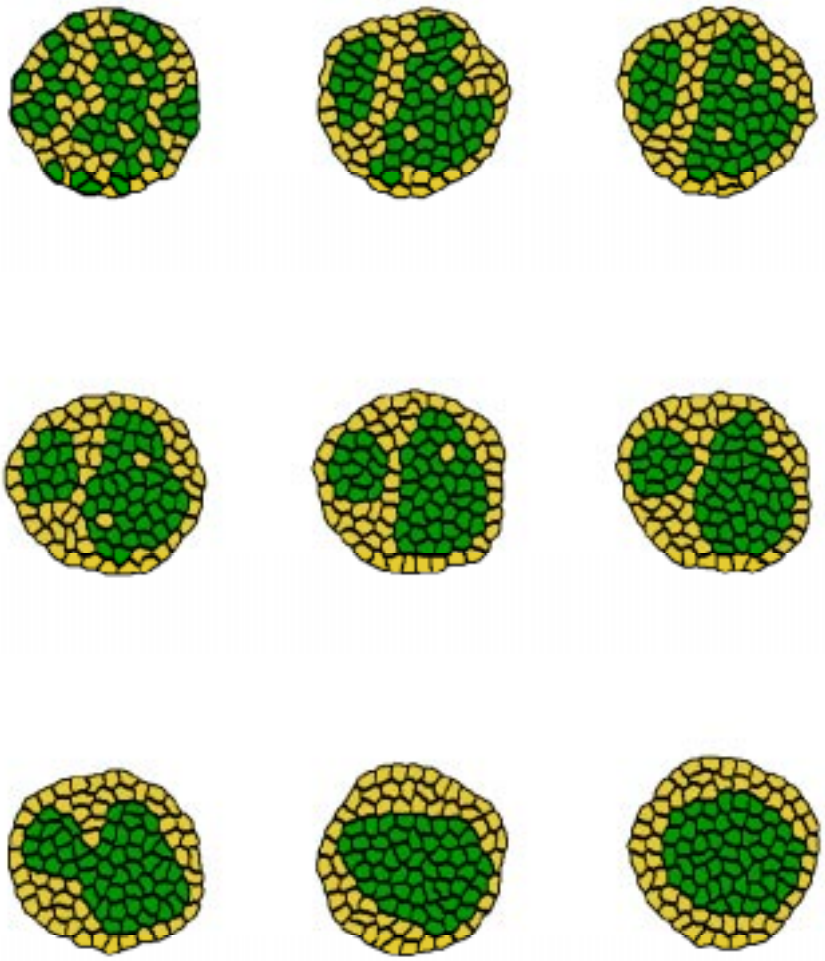

Figure 3.9. Simulation of cell sorting on a two-dimensional lattice (300 x 300). The temperature is T = 10 and the times are 1, 2, 4, 15, 17, 21, 23, 37 and 141 MCS from left to right and top to bottom.

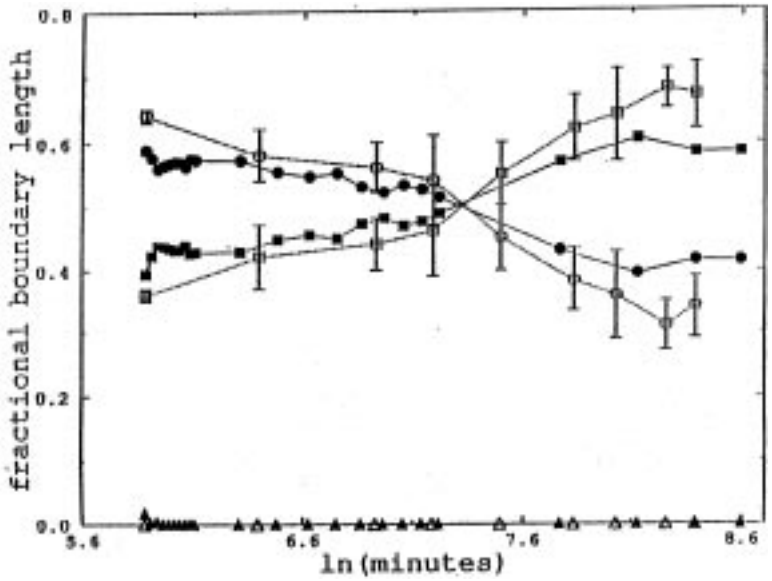

Figure 3.10. Time evolution of boundary lengths for cell sorting experiments (open symbols) and simulation (closed symbols). *Circles*: boundary between dark and light cells. *Squares*: boundary between light cells and medium. *Triangles*: boundary between dark cells and medium. Adapted from [5]

We measured boundary lengths for larger aggregates (300 - 500 μm in diameter) than those observed by Mombach *et al.* ($\sim$ 200 μm) [5]. In Figure 3.11, we plot the time evolution of the boundary lengths between pigmented and neural cells for a typical aggregate and observe the same logarithmic behavior.

Figure 3.12 shows a time series of the interfacial length between *Hydra* endodermal and ectodermal cells during sorting. We find that cell sorting in *Hydra* is a logarithmic process, just as in chicken embryos, and as predicted by the Potts model simulations. An important difference, however, between the time scales of sorting in *Hydra* and chicken, is that, as seen from the graphs, *Hydra* cells take on the order of 5-6 hours to sort whereas chicken aggregates of comparable size take up to 4-5 days. The faster sorting times are consistent with the much faster *Hydra*

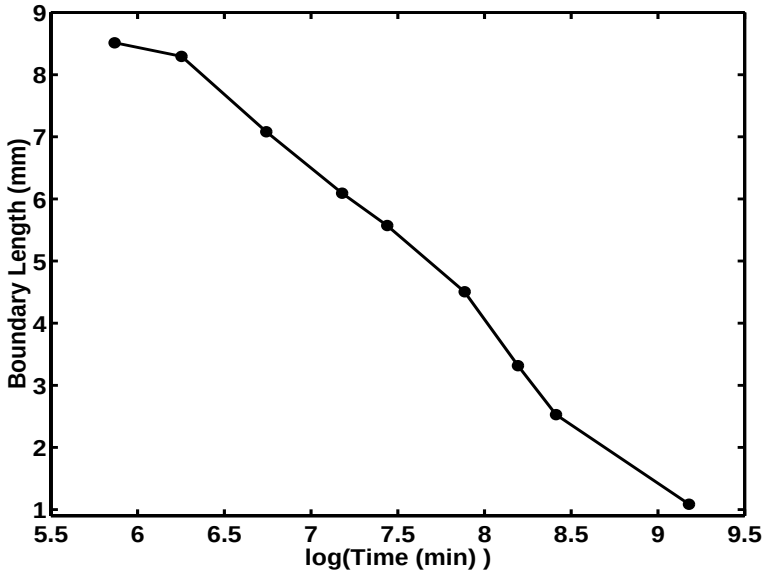

Figure 3.11. Time evolution of boundary length between pigmented and neural tissues for cell sorting experiments in chicken embryo

cell velocities (average velocity of $\sim 100\mu$m/hr) *vs.* chicken cell velocities (average velocity of $\sim 2\mu$m/hr).

Kataoka *et al.* [7] also showed logarithmic time evolution of boundary lengths in three-dimensional observations of sorting in *Hydra* (Figure 3.13). Their results indicate that the same dynamics do indeed hold in three dimensions as well as in two-dimensional projections.

Figure 3.14 shows the decrease in boundary length for a three-dimensional simulated aggregate. Simulations using the Potts model (with the lattice and parameters described in Section 3.4) show the same logarithmic time evolution of boundary length during sorting as seen in experiments with chicken and *Hydra* cells.

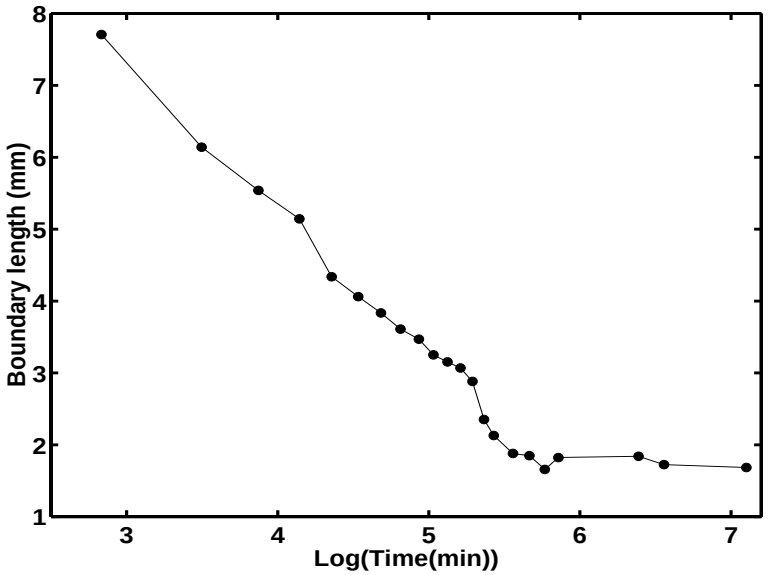

Figure 3.12. Time evolution of boundary lengths for cell sorting in *Hydra* cell aggregates. The graph shows the evolution of boundary between ectoderm and endoderm. The flat tail when the boundary lengths stopped decreasing indicates complete sorting.

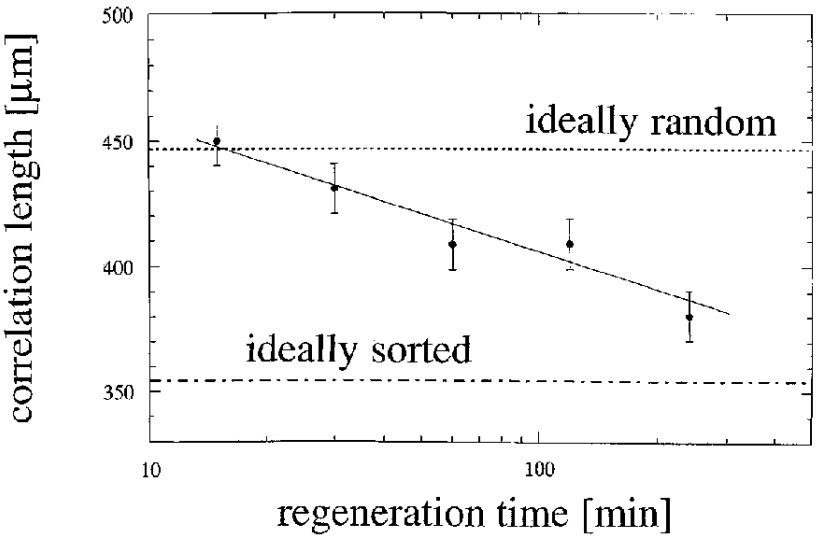

Figure 3.13. Time evolution of the correlation length or the mean distance between endodermal cells during sorting in three-dimensional *Hydra* aggregates as obtained from MRI images. Adapted from [7]

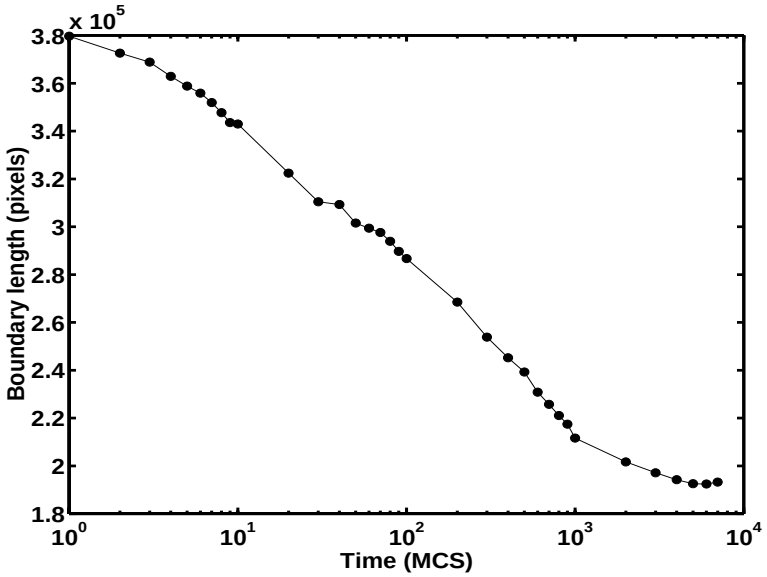

Figure 3.14. Time evolution of boundary lengths for cell sorting in three-dimensional Potts model simulation. The values of the various parameters are: $J(1,1) = 7$; $J(1,2) = J(2,1) = 5$; $J(1,3) = J(3,1) = 8$; $J(2,2) = 2$; $J(3,3) = 16; \lambda = 1; T = 32$.

3.6 Simulations with Negative Energies

The simulations with positive energies suffice to model cell sorting but fail to reproduce single cell diffusion accurately. In Chapter 5, we present a detailed description of these results and a comparison with experiments. To correct the diffusion, we modified the Hamiltonian (Equation 2.12, as explained in Chapter 2) to use correct negative binding energies with a surface area constraint (perimeter in two dimensions) as well as a volume constraint (area in two dimensions). We simulated cell sorting in two dimensions with the modified Hamiltonian to test whether it reproduced the dynamics correctly. The values of coupling constants were: $J(1,1) = -7.33$; $J(1,2) = J(2,1) = -8.33$; $J(1,3) = J(3,1) = -0.667$; $J(2,2) = -11.33$. These values yield the same values of interfacial tensions as used for the earlier sim-

ulations. We set the area constraint to $\lambda = 1$, the perimeter constraint to $\Lambda = 1$ and the temperature to T = 10. Figure 3.15 shows that the sorting pattern is normal.

Figure 3.16 shows that the decrease in boundary lengths between dark and light cells is also logarithmic in time. The logarithmic decay is consistent with previous simulations and experiments and shows that changing the Hamiltonian in this way does not change the observed sorting dynamics. These modifications make the simulation more realistic. The surface area and volume constraints control the cell shapes. The spin-spin coupling acts only as an adhesive interaction.

A comparison of the time rate of cell sorting for different values of the area and perimeter constraints highlights some properties of the simulation. Figure 3.18 shows the effect of changing the temperature on the evolution times. At zero temperature, the pattern freezes and does not sort. At T=1 and T=2, sorting is extremely slow, but a light-cell monolayer does not form within our observation time. T=5, T=10 and T=20 represent a regime where sorting is normal. However, contrary to what we would expect, sorting at T=20 is slower than at T=10. Thermal fluctuations start to dominate. The effect is very clear for T=40 and T=80. Strong thermal fluctuations prevent the lattice from reducing its light-dark heterotypic boundary length. The boundary length reaches a plateau before formation of a light monolayer. The cell boundaries appear highly crumpled and a few cells escape into the outer medium. The simulation temperature represents the cytoskeletal fluctuation amplitudes of the cell membrane. Normal sorting requires optimum values of membrane fluctuations. We discuss the effect of membrane fluctuations in different cell types in Chapter 5.

Figure 3.19 shows the effect of changing the area constraint λ on the evolution times. Sorting is slowest for the largest values of λ and sorting time decreases

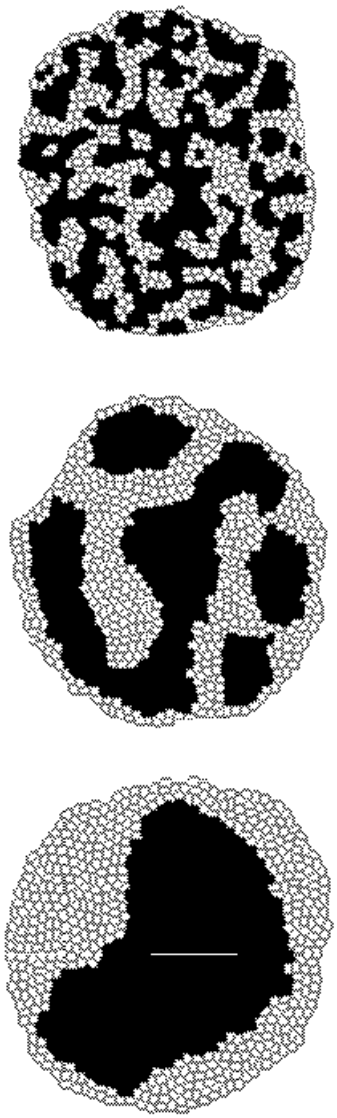

Figure 3.15. Two-dimensional simulation of cell sorting using negative energies: (a) Time = 2000 MCS. (b) Time = 80000 MCS. (c) Time = 640000 MCS. The values of various parameters are: $J(1,1) = -7.33$; $J(1,2) = J(2,1) = -8.33$; $J(1,3) = J(3,1) = -0.667$; $J(2,2) = -11.33$; λ=1; Λ=1; and T=10.

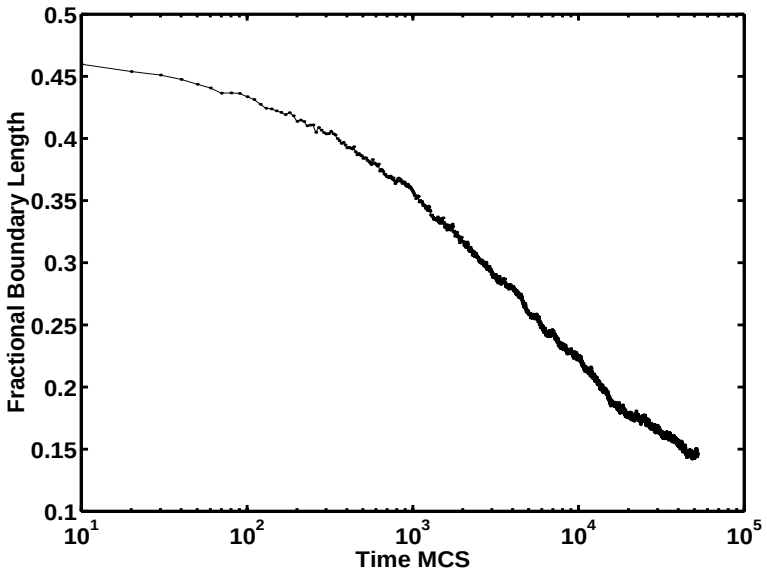

Figure 3.16. Logarithmic time evolution of dark-light boundary length for cell sorting in simulated two-dimensional aggregates with perimeter constraint and negative energies. The values of various parameters are: $J(1,1) = -7.33$; $J(1,2) = J(2,1) = -8.33$; $J(1,3) = J(3,1) = -0.667$; $J(2,2) = -11.33$; λ=1; Λ=1; and T=10.

smoothly as a function of λ. The pattern did not freeze for any of the observed values, but may do so for much larger values. Qualitatively, the area constraint makes the cell more rigid and less likely to shrink. Consequently, the cell areas were closer to the target area (35), for higher λ values. For low λ's (0.01, 0.2), the cell boundaries appear very flexible and the cell areas are quite far from the target area. The cells keep shrinking as the simulation proceeds (for λ=0.01, the cell area falls to 15; for λ=0.2, the cell area falls to 23). Cells do not disappear even for very small values of λ, as they do in the positive energy simulations, because of the perimeter constraint which does not allow the cells either to disappear or break up. The cells become flaccid and very deformable in order to maximize their boundary.

We also studied the effect of varying the perimeter constraint Λ. Figure 3.20 shows the evolution of boundary lengths for different values of Λ with T and λ

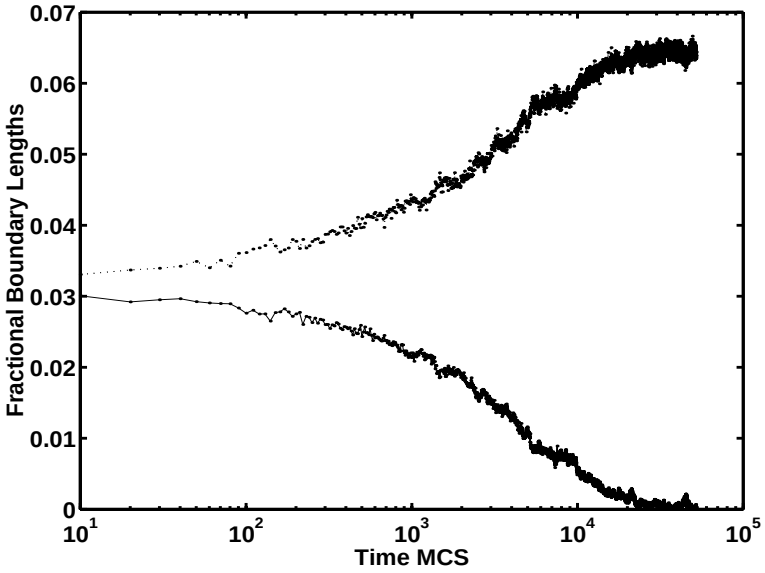

Figure 3.17. Time evolution of dark-medium (lower) and light-medium (upper) boundary length for cell sorting in simulated two-dimensional aggregates with perimeter constraint and negative energies. The values of various parameters are: $J(1,1) = -7.33$; $J(1,2) = J(2,1) = -8.33$; $J(1,3) = J(3,1) = -0.667$; $J(2,2) = -11.33$; λ=1; Λ=1; and T=10.

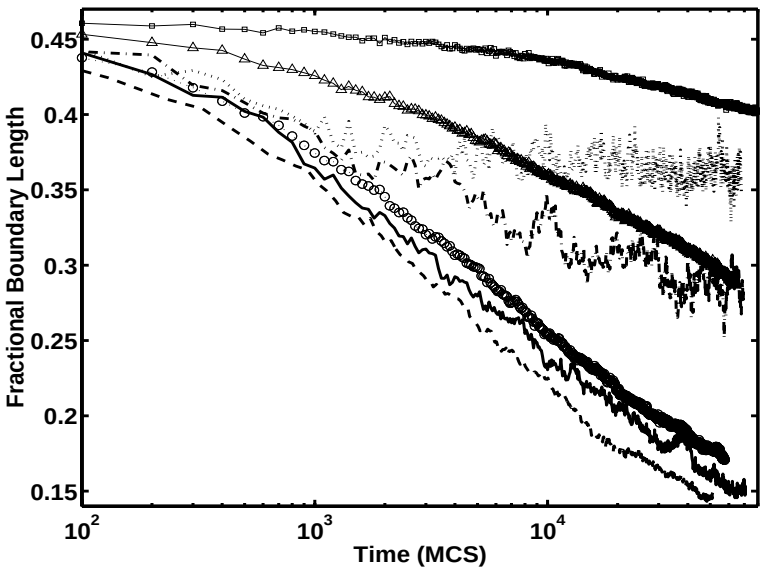

Figure 3.18. Time evolution of dark-light boundary lengths at different temperatures in simulated two-dimensional aggregates with perimeter constraint and negative energies. The various parameters are: $J(1,1) = -7.33$; $J(1,2) = J(2,1) = -8.33$; $J(1,3) = J(3,1) = -0.667$; $J(2,2) = -11.33$; λ=1; and Λ=1. The temperatures are: T=1 (squares), T=2 (triangles), T=5 (circles), T=10 (dashed line), T=20 (solid line), T=40 (dash-dotted line), and T=80 (dotted line).

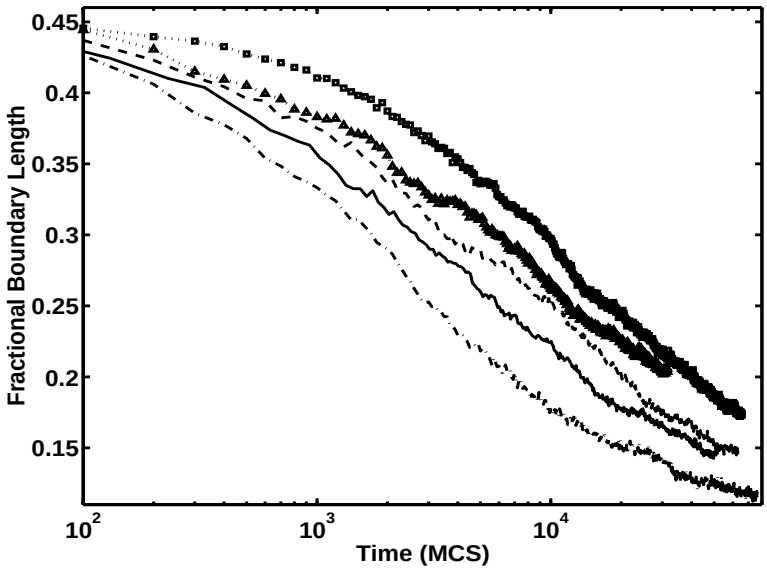

Figure 3.19. Time evolution of dark-light boundary lengths for various values of λ in simulated two-dimensional aggregates with negative energies. The values of the parameters are: $J(1,1) = -7.33$; $J(1,2) = J(2,1) = -8.33$; $J(1,3) = J(3,1) = -0.667$; $J(2,2) = -11.33$; Λ=1; and T=10. The values of λ are: λ=10 (squares); λ=5 (triangles); λ=2 (dashed line); λ=1 (solid line); and λ=0.2 (dash-dotted line).

fixed. For Λ=10, the pattern almost freezes, with hardly any change in boundary length. Λ=5 results in a very slow evolution, the monolayer does not form completely. For Λ = 2, 1 and 0.2, we observe normal sorting. When Λ=2, typical cell perimeters (140) are much larger than the target perimeter (125), due to the weak perimeter constraint. The perimeter constraint plays the role of the bending and shear elasticity of the cell membrane; higher values prevent the cell from stretching or deforming. Low values allow greater flexibility.

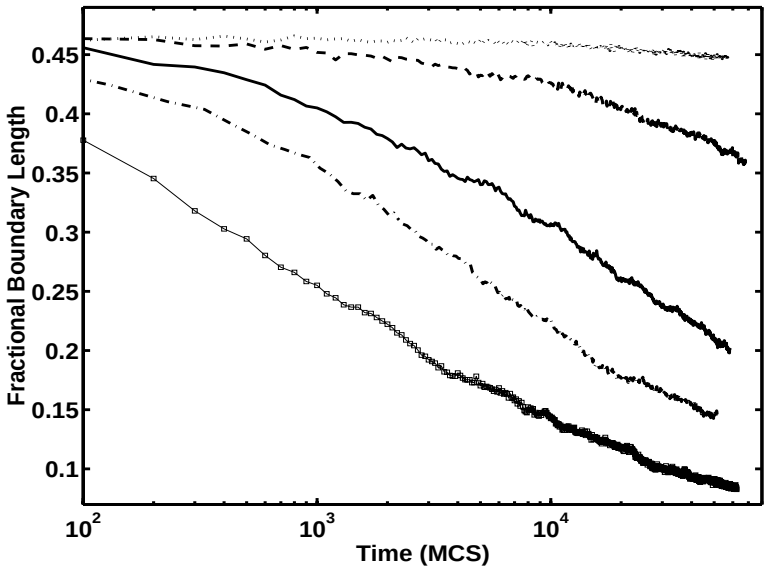

Figure 3.20. Time evolution of dark-light boundary lengths for various values of Λ in simulated two-dimensional aggregates with negative energies. The values of the parameters are: $J(1,1) = -7.33$; $J(1,2) = J(2,1) = -8.33$; $J(1,3) = J(3,1) = -0.667$; $J(2,2) = -11.33$; λ=1; and T=10. The values of Λ are: Λ=10 (dotted line); Λ=5 (dashed line); Λ=2 (solid line); Λ=1 (dash-dotted line); and Λ=0.2 (squares).

The agreement between simulation and experiment suggests that differential adhesion is the main mechanism involved in cell sorting. The adhesion energy landscape has moderate local minima, which the cells overcome with the help of cytoskeletal fluctuations, to reach the final state of global energy minimum. In spite of the large number and variety of specific molecules involved in the innumerable

chemical and signaling pathways, a simple factor - the relative surface energies - governs the macroscopic motion and final configuration of cellular aggregates. This effect of surface adhesions/surface tensions on sorting seems to be a property of a wide variety of tissues [84, 83] and therefore independent of the specific molecules involved. At this level of description, the nature of the molecules is irrelevant, except in the degree of adhesion they generate. The interactions of cell adhesion molecules on and between cell membranes and with the substrate give rise to forces. These forces determine the extent of tissue immiscibility and spreading and generate measurable surface and interfacial free energies. The same forces can arise from different specific molecules, but lead to the same morphogenetic patterns. The agreement in kinetics also suggests that the assumptions of time invariant adhesions and thermodynamics are reasonable. We can predict from simulations that increased cell membrane rigidity or cell turgidity (osmotic pressure) will slow sorting, while floppy cells with large surface to volume ratio will sort rapidly.

That the relative values of a single physical parameter, the tissue surface tension, should alone be capable of explaining all cases of tissue sorting and spreading, seems an over-simplification. But, regardless of what other properties cells have and how these properties change due to cell signalling and interactions, if the cells remain mobile cohesive units, their adhesive interactions will constantly act as a set of unavoidable physical determinants compelling them to shift positions at every opportunity to increase their binding intensities. Cells are constantly moving, breaking and remaking bonds as they change their neighbors. If they encounter cells with which they form stronger bonds, they tend to stick, while if the bonds are weaker, the probability of detachment is greater. Through repetitions of this process, as long as the cell membrane fluctuations are strong enough to break bonds

and weak enough not to overwhelm the energy gradients, the cell population approaches a configuration in which it maximizes the total intensity of bonds and its interfacial free energy represents nearly a global minimum.

3.7 Phase Separation

Comparison with the Potts model simulations can at best be semi-quantitative. The simulation essentially reproduces the energetics of the evolution. Extracting experimental quantities like viscosity which is crucial in determining the dynamics of sorting, is not very easy. To better understand the mechanism of cell sorting we consider an hydrodynamic analogy. Cell sorting is qualitatively similar to the phase separation of two immiscible liquids. We can characterize cells as materials with fluid properties. The aggregate viscosity is much larger than water, so cells are too big to diffuse efficiently under thermal agitation. Surface tension driven flow and active fluctuations of cell membranes govern the dynamics.

During the time evolution of developing patterns, a common growth mechanism is the coalescence or fusion of interacting domains, especially in tissues and liquids where the coalescence of two clusters or drops governs the morphology and kinetics. In liquids, coalescence is hydrodynamic, driven by the interfacial tension σ between the two phases and damped by the viscosity η of the more viscous phase [136, 137]. Experiments with fluids under reduced gravity provide some very general results for fluid droplet coalescence [138]. To what extent does the theory for fluids apply to biological tissues? We have experimentally measured the size distribution and growth law for cell clusters during sorting. We wish to develop an hydrodynamic model for cell sorting similar to that for fluids. Can we generalize the fluid analogy for embryonic tissues to interpret the kinetics of sorting?

When we thermally quench a homogeneous mixture of two fluids (from its one phase region to the two-phase region) through its critical temperature at its critical concentration, it phase separates, in **spinodal decomposition**. The domains of the two phases nucleate and grow. Figure 3.21 shows the evolution of the pattern by droplet coalescence during spinodal decomposition [8].

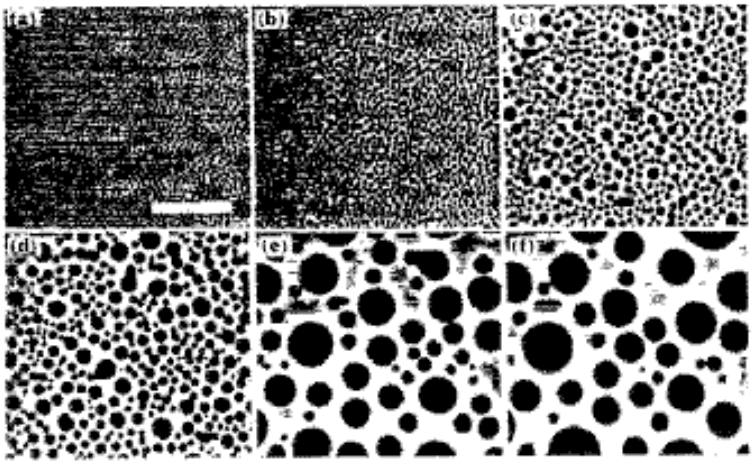

Figure 3.21. Pattern evolution during spinodal decomposition in OCL/OS (oligomeric mixture), at intervals 2s, 9s, 60s, 120s and 1110s respectively after quenching through the phase-separating temperature (150°C). Adapted from [8]

Two alternative regimes of coarsening are possible. When the volume of the minority fraction ϕ is lower than a threshold, the domain size grows as:

$$R \propto t^{1/3}, \tag{3.3}$$

where R is a characteristic domain size and t is the elapsed time [139]. The domains grow as spherical drops. Recent experiments [140] show that for $0.1 < \phi < 0.3$, the mechanism of Brownian drop motion and coalescence can explain the $t^{1/3}$ growth. Droplets of the minority phase diffuse due to thermally activated Brownian motion. When two droplets collide, they recombine to form a drop of larger size. Hydrodynamic interactions do not play an important part in this regime. (When

$\phi < 0.1$, the mechanism is a Lifshitz-Slyozov growth which also yields $R \propto t^{1/3}$.) Smoluchowski first considered the Brownian mechanism for coagulation of colloids and Binder and Stauffer [141] and Siggia [136] applied it to phase separation.

For large volume fractions ($\phi > 0.3$), coalescence creates a complicated interconnected network of droplets. The droplets collide and coalesce due to attractive hydrodynamic interactions [138]. The domains of the minority phase grow and the coarsening law is linear in time. The **tube instability** explains the linear growth rate. For concentrated mixtures, spinodal decomposition results in the initial formation of an interconnected mixture. We can idealize the interconnected structure as a long fluid tube of radius R. The capillary pressure at any point along the interface will be approximately σ/R. However, this pressure must match that in the bulk fluid given by the Navier-Stokes equation which is roughly $\eta\Delta\mathbf{v}$. Dimensional analysis then leads to the growth law:

$$R \sim \frac{\sigma}{\eta} t. \tag{3.4}$$

These results hold for three dimensional fluids. In two dimensions, which we will not discuss here, somewhat different results obtain [142, 143].

3.7.1 Growth Law for Dense Aggregates

In this section, we show evidence that mixtures of two types of tissues can behave like phase separating liquids, qualitatively and quantitatively. The liquid droplets correspond to individual cells and when two highly adhesive cells come in contact, they adhere to each other and change shape to form a larger spherical cluster, just as two droplets merge to form a bigger droplet of larger radius. Cells are in very close contact with each other. To move within the aggregate, they need to squeeze

past other neighboring cells. This type of motion could lead to some hydrodynamic interactions similar to those found in liquids.

To examine growth laws, we considered the cell sorting experiments with neural retinal and pigmented epithelial cells which we described before. Figure 3.22 shows the growth of pigmented clusters in neural retinal tissue.

The image analysis was the same as before. We calculated the radius of gyration of each of the cell clusters at every time step. We took the average value and plotted it as a function of time. The smaller clusters grew larger until only one large cluster of dark cells survived. Figure 3.23 shows that the cluster sizes grow linearly in time, in agreement with the theory for the case of large volume fractions. We fit the data to:

$$L = A + Bt, \tag{3.5}$$

with A = (32.3 $\pm$ 5) μm and B = (2.7$\pm$0.3) μm s^{-1}.

We can thus understand cell sorting as a consequence of the fusion of cells and cell clusters. We can describe it in terms of an effective tissue viscosity and surface tension, both of which depend on the degree of cell adhesion. As cells move, they constantly rupture and reform their bonds with other cells. The greater the binding energy of the adhesion molecules, the more stable the bonds will be. The friction experienced by the cells (which directly relates to the viscosity) will be proportional to the number of adhesion molecules on the surface.

The rate of sorting should depend on the particular tissue types used. By conducting experiments on several tissue-pairs (*e.g* liver-pigmented, neural-liver *etc.*), we should be able to obtain sorting rates for the different cases. The values obtained from the linear growth law yield the binding energies between cells [144].

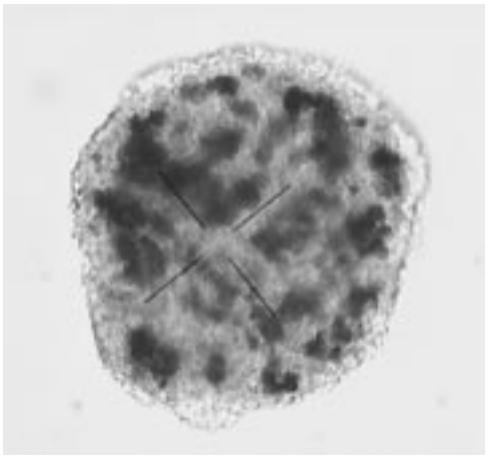

t = 38 hr

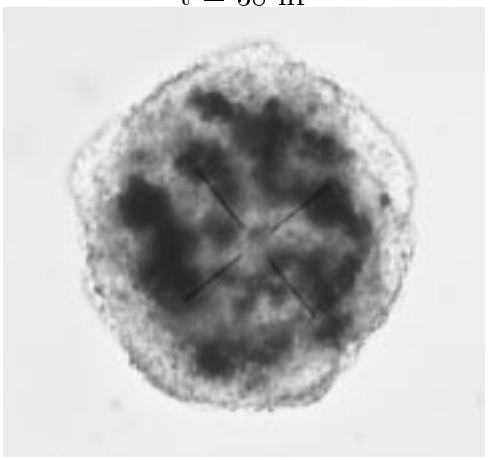

t = 64 hr

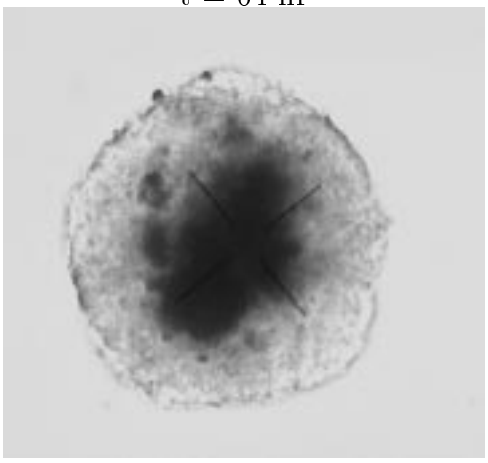

t = 88 hr

Figure 3.22. Sorting out of pigmented (dark) and neural (light) cells. The dark cell clusters coalesce and grow to form eventually a fully sorted aggregate with only one large cluster.

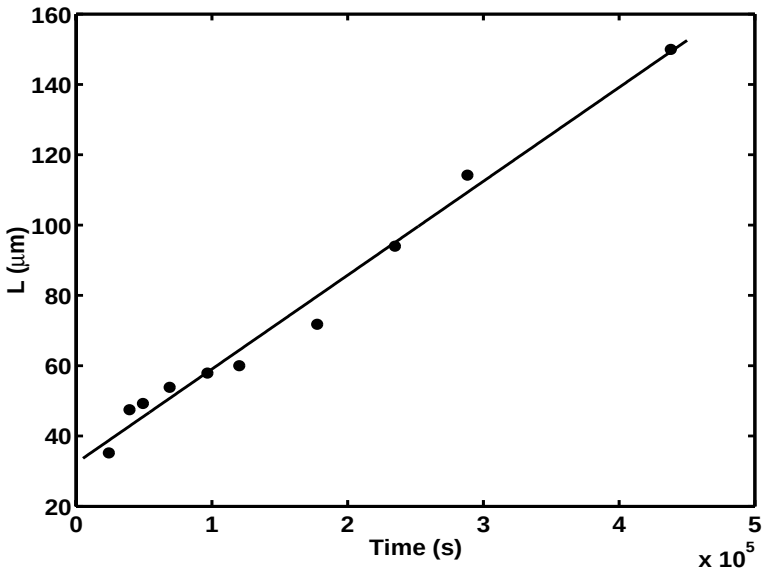

Figure 3.23. Growth of mean size of pigmented cell clusters in neural aggregate as a function of time. The graph shows a linear growth law.

3.7.2 Phase Diagram

We estimate the volume fraction of the tissues from the surface fraction of the minority phase. To calculate the surface fraction, we analyze the digitized images as explained before. We separate the dark cells, light cells and surrounding medium into distinct regions with a single grey level value for each. We then count the total area of the dark and light phases to give the surface fraction f. This value depends on the value of threshold chosen to identify the different regions. To make the process more consistent, we choose the threshold in such a way that the boundary between dark and light cells is at the point of highest contrast (as explained in Section 3.3). However, the relation between the surface fraction f and the volume fraction ϕ is not simple. We cannot extract ϕ from the earlier pictures of the time evolution where the dark clusters are scattered. In the last picture of the fully sorted tissue, we can get a crude estimate of the volume fraction by assuming that

the aggregate roughly resembles two concentric spheres. We then obtain:

$$\phi = f^{3/2}. \tag{3.6}$$

The time taken to complete sorting will depend on several factors: the surface fraction of dark cells, the size of the aggregate and the particular cell types used (since they have different adhesion properties). We conducted several sorting experiments with aggregates of different sizes and with varying fractions of dark cells. The number ratios for neural retinal cells to pigmented retinal cells ranged from 10:1 to 50:1. Our goal was to study the size of the aggregate versus the surface fraction of dark cells with respect to the time taken for complete sorting. Did aggregates of all sizes and surface fractions always sort? We also wanted to determine the growth rate at low volume fractions.

Figure 3.24 shows a plot of aggregate sizes as a function of volume fraction of dark tissue 76 hr after aggregate formation (circles and bullets) and 120 hr after aggregation (stars). We see that all small aggregates, with high or low volume fractions have sorted completely (denoted by open circles). On the other hand, most large aggregates ($> 8\text{x}10^4$ μm^2) are only partially sorted (denoted by solid bullets). Only the large aggregates that have about 30% surface fraction of pigmented cells have sorted fully. We also see that after 120 hr, even some large ($\geq 8\text{x}10^4$ μm^2) aggregates (denoted by crosses) have sorted out completely. The largest such aggregate ($16\text{x}10^4$ μm^2) has a surface fraction of 0.22 which corresponds to a volume fraction $\phi = 0.1$ that is 10%. From these data, a threshold of 30% below which phase separation is not complete, as for liquids, seems unlikely. However, we need to test this threshold with experiments using very dilute concentrations of dark cells in large neural aggregates. Preliminary experiments show that due to the very low mobility of cells in tissue, growth of dilute aggregates is extremely slow and quan-

titative results with adequate scaling are difficult to obtain. As cluster sizes grow, the diffusivity decreases. Clusters do not grow much over the time that we can keep aggregates alive.

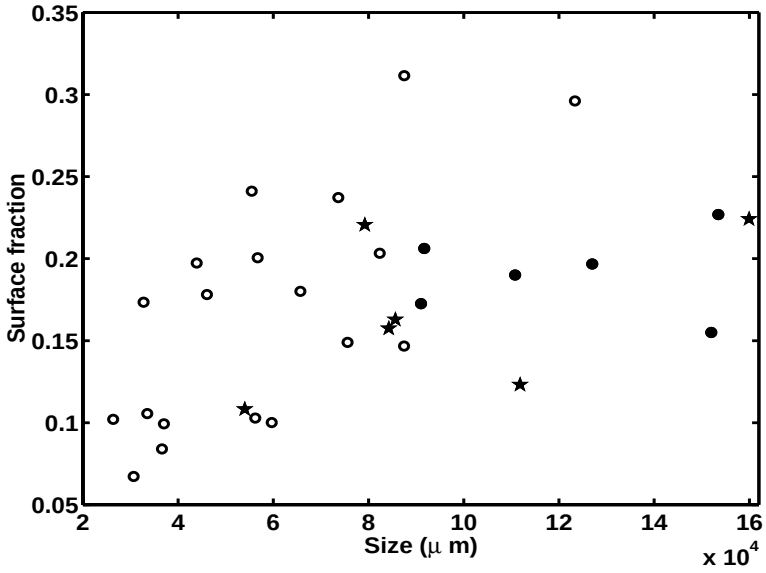

Figure 3.24. Graph depicting degree of sorting of aggregates of various sizes as a function of the fraction of dark (pigmented epithelium) cells. *Open circles:* Fully sorted aggregates 76 hours after aggregate formation. *Bullets*: Partially sorted aggregates after 76 hours. *Stars*: fully sorted aggregates 120 hours after aggregate formation

3.7.3 Preliminary Simulations

The several types of simulation of the phase separation of binary fluids include molecular dynamics and lattice Boltzmann approaches which take into account the detailed hydrodynamic contributions [145]. Some of them are inconsistent with scaling arguments based on dimensional analysis (as described in Section 3.7). For example, Ma *et al.* [145] found a growth exponent of 0.6 ± 0.1 for the domain size, not 1. Do cells and tissues really behave like liquids, even if the they happen to follow the same growth laws? Potts model simulations may be able to answer this question.

A comparison of the growth laws for dense and dilute simulated cell mixtures with those found for liquids and real tissues will be very useful and may provide valuable insight into how cells behave. We have performed preliminary simulations (using the original positive energy Hamiltonian, Equation 2.7) of sorting in two-dimensional aggregates with varying concentrations of dark (more cohesive) cells. Simulations in three dimensions (which are computationally very intensive) and using the negative energy Hamiltonian are the subject of current research.

In Figure 3.25, we plot the heterotypic interface length as a function of time for three different concentrations of dark cells: 30%, 50% and 70%. We see that the time scale of sorting is logarithmic for all cases. The aggregate with (50%) concentration has an interconnected dark cell cluster almost throughout the sorting. The aggregates with 30% and 70% of dark cells form isolated clusters of dark and light cells respectively.

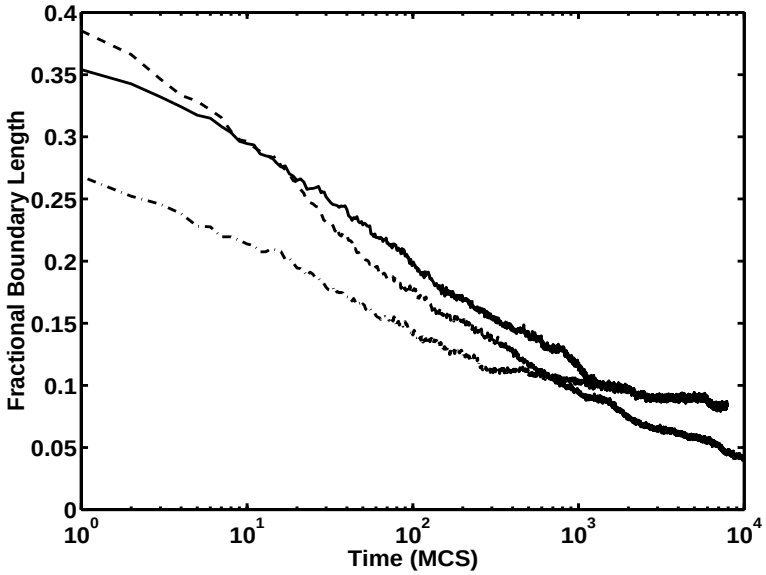

Figure 3.25. Fractional boundary length of the heterotypic (dark-light) interface for different concentrations of dark cells. *Solid*: concentration is 30%. *Dashed*: concentration is 50%. *Dotted*: concentration is 70%.

In Figure 3.26, we show the final images of the aggregates after the sorting simulations. When the concentration is 30%, the dark cells form several large clusters which are well separated from each other. The boundary length between dark and light is still decreasing slowly as we can see from the solid curve of Figure 3.25. However, from about 1000 MCS, when most of the small clusters have fused into a few large clusters, the curve has a smaller slope than before. Eventually, the cells may sort out, but they will take an extremely long time. Or, they may remain stuck in a metastable local minimum. At a concentration of 50% dark cells, sorting is complete by 10000 MCS. The boundary length (dashed curve) is still decreasing due to rounding of the inner cluster. For a dark cell concentration of 70%, an outer light monolayer forms as expected, but the fewer light cells in the interior of the aggregate trap within the large mass of dark tissue. In some ways, we see a reversal of positions due to the peculiar two-dimensional geometry. Again, the cells do not sort out on the observed time scales, and may stick in a local minimum.

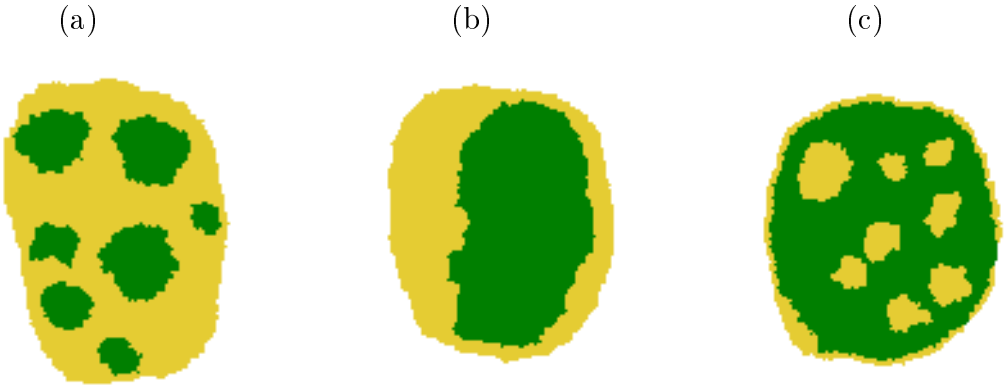

Figure 3.26. Simulation of cell sorting in 2D aggregates: (a) Concentration of dark cells is 30%. (b) Concentration is 50%. (c) Concentration is 70%.

Future work will involve simulation of cell sorting for varying concentrations of dark cells in large three-dimensional aggregates. We expect that, in three-dimensional aggregates, we will not observe the formation of these metastable states at low and high concentrations. The extra degree of freedom should allow the cell clusters to connect to each other and facilitate sorting. For extremely low concentrations, we may observe trapping. We have yet to determine the critical concentration below which aggregates do not sort. We will also repeat our analysis of the growth rate of the characteristic wavelength (or domain size) for the simulations in two and three dimensions to compare with the theory for fluids.

CHAPTER 4

TISSUE ENGULFMENT

4.1 Introduction

Any two immiscible liquids in contact have a characteristic interfacial tension. Because a change in the area of the interface has a cost in terms of free energy for fluids at equilibrium, the interface will have a well defined shape. In other words, the degree of mutual spreading of contiguous liquids or the engulfment of one liquid (or tissue) by another, will depend on the relative strength of the interfacial tension between the two liquids compared with the tensions at the interfaces of the two liquids with their other bounding medium [9] (Figure 4.1). Because the relative balance of adhesive interactions at the various interfaces determines the extent of spreading, the adhesion or de-adhesion of a cell population to different bounding surfaces can drive its motion [146].

Individual cells also exhibit fluid properties and can locomote along adhesive substrates by interfacial tension. This phenomenon is called **haptotaxis** [31]. However, a single cell can move along its substrate by haptotaxis only if the substrate becomes progressively more adhesive with distance *i.e.* in the presence of an adhesion gradient. On the other hand, the liquid-like spreading of the tissue as a whole along a substrate, much like the spreading of a film of oil on water, can explain the concerted movement of a cell population. The substrate needs to be adhesive, but need not contain an adhesion gradient.

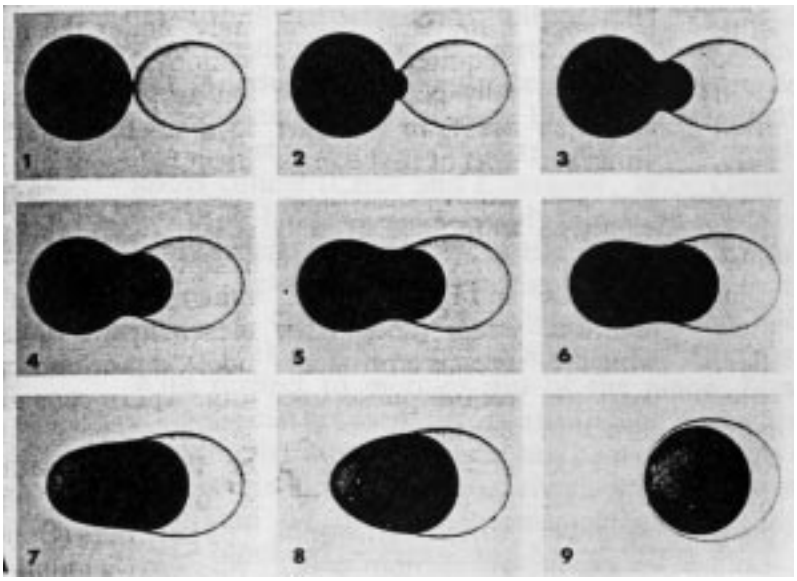

Figure 4.1. Photographs of the stages of complete engulfment of water plus 1% malachite green (black drop) by a drop of polyglycol oil, suspended in silicone oil. Frames 1 to 6 show the penetration of the aqueous phase into the oil phase, and frames 7 to 9 show the subsequent relaxation of the deformed water drop into the oil drop. The total elapsed time is 0.9 sec. The diameter of the polyglycol oil is 0.8 mm. Adapted from [9]

In this chapter, we present the first quantitative studies of experiments and computer simulations of engulfment in embryonic chicken tissues. We measure comparable parameters in both cases and establish that differential adhesion is the key mechanism driving tissue spreading. We also compare engulfment with the coalescence of liquid drops using the theory for liquids. The simulation predicts that engulfment does not require active fluctuations of cell membranes. We test this hypothesis by carrying out engulfment in the presence of Cytochalasin-B and at reduced tempreratures.

4.2 Theoretical Background

We treat the two types of tissues and the culture medium as analogous to three liquid phases. In Figure 4.2, we show schematically three phases, α, β and γ, occupying the dihedral angles between locally planar interfaces ($\alpha\beta$, $\beta\gamma$, and $\alpha\gamma$), which meet at the three-phase line. The **contact angles** α, β and γ are named after the phases they contain. We have:

$$\alpha + \beta + \gamma = 2\pi. \tag{4.1}$$

At equilibrium, the net force on any element of the three-phase line vanishes. Resolving this force in directions that are along the $\alpha\beta$, $\beta\gamma$, and $\alpha\gamma$ interfaces and are perpendicular to the three-phase line, we have:

$$\sigma^{\alpha\beta} + \sigma^{\beta\gamma}\cos\beta + \sigma^{\alpha\gamma}\cos\alpha = 0, \tag{4.2}$$

$$\sigma^{\alpha\beta}\cos\beta + \sigma^{\beta\gamma} + \sigma^{\alpha\gamma}\cos\gamma = 0, \tag{4.3}$$

$$\sigma^{\alpha\beta}\cos\alpha + \sigma^{\beta\gamma}\cos\gamma + \sigma^{\alpha\gamma} = 0, \tag{4.4}$$

$$\tag{4.5}$$

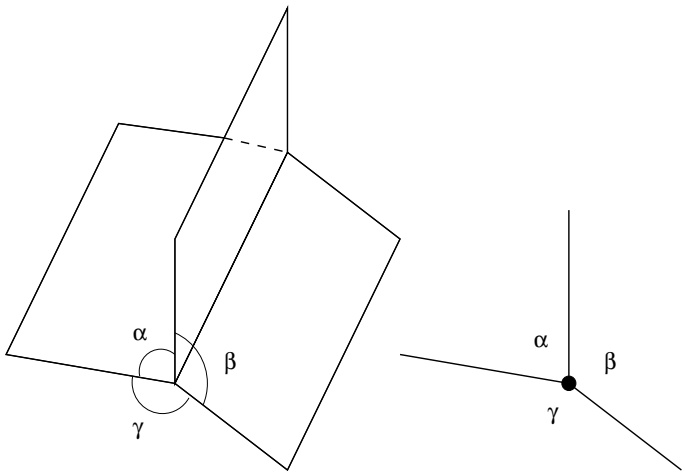

Figure 4.2. Schematic diagram of three fluid phases α, β and γ, meeting in a three-phase line

where $\sigma^{\alpha\beta}$ is the tension of the $\alpha\beta$ interface. From Equations 4.1 and 4.5, we can obtain the generic relations:

$$\frac{\sigma^{\alpha\beta}}{\sigma^{\beta\gamma}} = \frac{\sin\gamma}{\sin\alpha}, \tag{4.6}$$

and similarly for the other tensions. That is, we can only determine ratios of surface tensions, rather than the tensions themselves, in terms of the contact angles. The physical reason is that the forces on any element of the three-phase line would still balance with the same contact angles, if we multiply all the tensions by a common factor. Solving Equation 4.5, we obtain the cosine of the contact angles as:

$$\cos\beta = \frac{(\sigma^{\alpha\gamma})^2 - (\sigma^{\alpha\beta})^2 - (\sigma^{\beta\gamma})^2}{2\sigma^{\alpha\beta}\sigma^{\beta\gamma}}. \tag{4.7}$$

From Equations 4.6 and 4.7, we see that the interfacial tensions and the supplements of the contact angles form the sides and angles of a triangle (Figure 4.3). This triangle is called **Neumann's triangle**. The three interfacial tensions satisfy the triangle inequalities [147]:

$$\sigma^{\alpha\gamma} < \sigma^{\beta\gamma} + \sigma^{\alpha\beta}. \tag{4.8}$$

The largest of the three tensions must be less than the sum of the other two. When this condition is met, the equilibrium configuration is that shown in Figure 4.2. When the largest of the three tensions ($\sigma^{\alpha\gamma}$) *equals* the sum of the other two, the Neumann triangle degenerates to a line (Antonow's Rule).

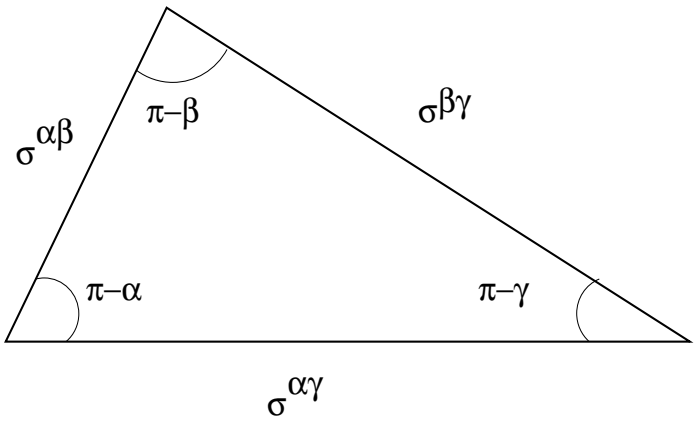

Figure 4.3. Schematic representation of Neumann's triangle

When two immiscible liquid drops suspended in a third immiscible liquid come into contact, three equilibrium configurations which depend on the **spreading coefficients** are possible. Suppose we consider the situation in which two drops (phases 1 and 3) with radii b_1 and b_2 come into contact in the liquid medium (phase 3). In this situation, we have three interfaces - the 12, 23 and 13 interfaces. The basic assumption is that the three interfacial tensions σ_{ij} solely determine the final equilibrium (gravity, fluid motion and inter-particle interactions do not determine the equilibrium configuration, though they may play an important role in attaining equilibrium). We define the spreading coefficient as:

$$S_i = \sigma_{jk} - (\sigma_{ij} + \sigma_{ik}). \tag{4.9}$$

The three possible sets of values for S_i are:

$$S_1 < 0, S_2 < 0, S_3 > 0, \tag{4.10}$$

$$S_1 < 0, S_2 < 0, S_3 < 0, \tag{4.11}$$

$$S_1 < 0, S_2 > 0, S_3 < 0. \tag{4.12}$$

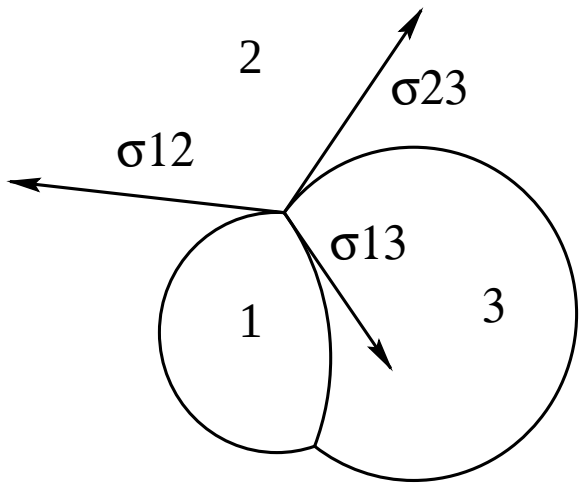

Figure 4.4. Schematic diagram of two drops of phase 1 and phase 3 immersed in medium of phase 2. The arrows indicate the three interfacial tensions σ_{12}, σ_{13} and σ_{23}.

Our experiments fall in category (4.11) in which we observe complete engulfment. Phase 3 completely absorbs phase 1 to form a spherical drop with two spherical interfaces (23 and 13). The external radius of this compound drop is:

$$r_{23} = ({b_1}^3 + {b_3}^2)^{1/3}. \tag{4.13}$$

Engulfment occurs by two competing processes: (i) the penetration of phase 1 into phase 3 under the action of a positive capillary pressure difference:

$$\Delta p_{13} = 2(\sigma_{12}/b_1 - \sigma_{23}/b_3), \tag{4.14}$$

across the 13 interface; and (ii) the spreading of phase 3 over phase 1 under the action of S_3.

The second condition (4.12) is the case of partial engulfment. The three interfacial tensions form the sides of a Neumann triangle with the 12, 13 and 23 interfaces in equilibrium along a 123 line bounding the three phases, as explained earlier. If the last condition (4.12) holds, the 13 interface cannot form spontaneously, and the drops remain separated.

4.3 Experiment

4.3.1 Basic Protocol

We have conducted experiments on tissue engulfment with different combinations of cell aggregates from chicken embryos - neural retinal, heart and liver cells. Let us first consider the case of heart and neural retinal cells. We dissected these tissues from chicken embryos and dissociated them using the standard protocol described in Appendix A. Using the fluorescent dye DiI, we stained the heart cells. We then made spherical aggregates with stained (heart) and unstained (neural retinal) cells and centrifuged two aggregates at a time to make adherent pairs (one stained and one unstained) for observation. (See complete protocol in Appendix A). We transferred each aggregate pair to one well of a 24-well cell-well plate for observation under the microscope.

We took images using the microscope-video-computer setup as described in Chapter 3 and saved them digitally on the computer every 30-60 min to obtain two-dimensional projections of the three-dimensional aggregates. We viewed the fluorescent aggregates by exciting the dye molecules with light of wavelength 460 nm. (The emission wavelength is 580 nm). Simultaneously, we used regular white light illumination of reduced power to see faintly the non-fluorescent aggregate. In

the images, then, the fluorescent aggregate is the brightest, the second aggregate has an intermediate level of brightness and the surrounding medium is the darkest. We histo-equalized the images and thresholded to bin them into three intensity regimes: **dark**, **medium** and **light**. We then located the boundaries of both aggregates as well as the boundary of the interface between the two. Since the fluorescence is bright, we can easily locate the sharp interface between the fluorescent and non-fluorescent aggregate using a boundary tracing algorithm. We used FORTRAN and MATLAB programs for the image analysis.

4.3.2 Use of Cytochalasin

We wanted to observe whether engulfment does indeed occur in the absence of active fluctuations of the cell membrane. The ability of Cytochalasin to inhibit active cellular motion makes it useful for investigating the movement of cells in three-dimensional cell aggregates. We use Cytochalasin-B in our experiments to suppress membrane activity (see Chapter 3 for more details). We modify the medium by adding Cytochalasin-B which we have first dissolved in DMSO (di-methyl sulfoxide). We carry out the entire experiment, after the formation of aggregates, in the presence of Cytochalasin-B, allowing enough time for the drug to diffuse into the cells and inhibit actin polymerization. After we have fused the aggregates together, we move them from regular medium into medium containing Cytochalasin-B. The rest of the steps are unaltered. We carried out the experiment at several different concentrations of Cytochalasin-B ranging from 0.1μg/ml to 10μg/ml. In some cases, we allowed the aggregates to engulf normally for a few hours and then placed them in medium containing Cytochalasin-B.

Cytochalasin inhibits the actin dynamics of the cells at the leading edge, thus affecting the cells' ability to move. Will tissue engulfment proceed without active

cell motility? Is engulfment really a surface tension driven flow? If the values of the relative surface tensions are not affected, then the tissues should still engulf, according to the theory of differential adhesion. However, at least minimal fluctuations might be essential to allow the cells to overcome viscous drag. The surface tensions may also change as we discuss in Section 4.4.4.

4.4 Results

4.4.1 Experiment

Figure 4.5 shows a time series of images of a pair of heart and neural aggregates. The bright, stained tissue is the heart tissue and the darker unstained aggregate is the neural tissue. As we can see in the first frame (5 hr after we made the two aggregates adhere), the heart tissue forms a convex interface with the neural tissue, indicating that the neural tissue has a lower surface tension, agreeing with Foty *et al.* [83]. In later time steps, we see the neural retinal aggregate "engulfing" the heart aggregate. Eventually, after about 72 hr, the neural tissue completely surrounds the heart tissue. The heteroptypic interface (between the heart and neural tissues) grows and the contact angle between these two phases decreases. Qualitatively, the sequence of images looks analogous to the images of engulfment of a water drop by oil, (Figure 4.1). During the intermediate stages, the heart aggregate elongates a little (as does the water droplet) under the effect of the opposing forces of surface tension and drag.

An important difference is that oil-water engulfment is orders of magnitude faster than the tissue pair engulfment. The total time in the former is 0.9 s while the latter takes 72 hr. This time reflects that cellular tissues have viscosities that are much higher than those of normal liquids. Forgacs *et al.* [85] have measured the viscosities of several types of chicken embryonic tissues, in the range of 10^5 Poise, many orders

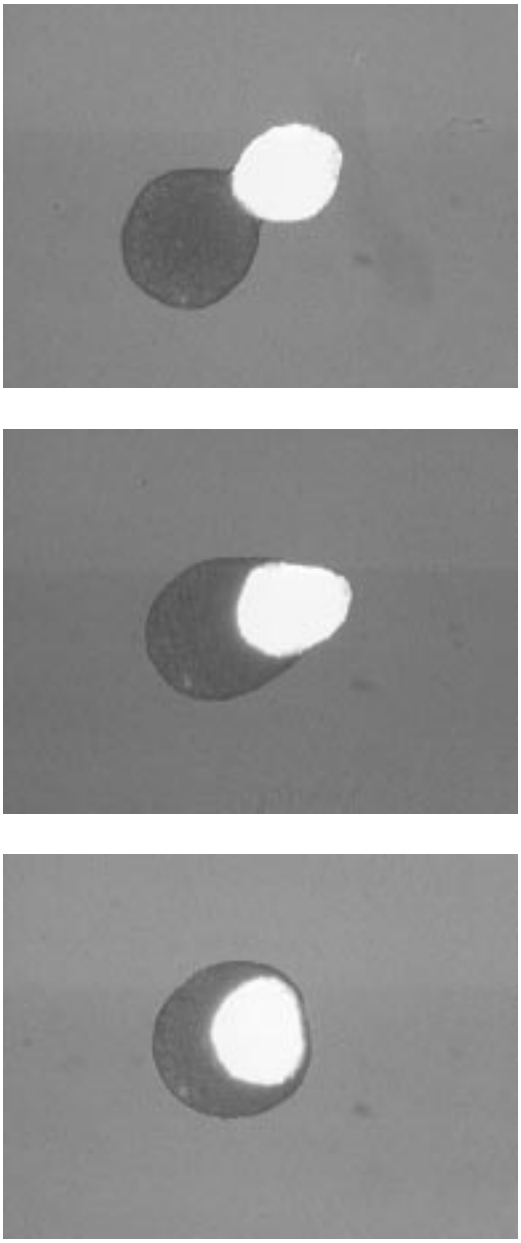

Figure 4.5. Complete engulfment of heart tissue (bright sphere) by neural retinal tissue (dark sphere) from chick embryo. Elapsed time is 9 hr. The heart tissue is 325 μm in diameter.

of magnitude larger than the viscosity of water (10^{-2} Poise.) The surface tension of water (at 20°C) is 72.8 dyne/cm. The interfacial tension of mineral oil and water is about 30 dyne/cm, the same order of magnitude as the effective surface tensions of embroynic tissue aggregates; the surface tension of heart is 8.5 dyn/cm and that of neural retinal tissue is 1.6 dyn/cm. These values indicate that the extremely high viscosity of the tissues slows down engulfment compared to liquids. *In vitro*, slowing limits the size of aggregates that we can use to study complete engulfment, since aggregates remain viable only for 2-3 days. Larger aggregates take longer to engulf, but we have not systematically studied the quantitative effect of aggregate size on the rate of engulfment. The growth of the interface should be linear in time irrespective of aggregate size. The length parameter will depend on the particular geometry of the situation, the slope of the curve between the appropriately scaled length parameter and time should be equal to the surface tension to viscosity ratio.

4.4.2 Simulations and Comparison

We simulated engulfment using the Potts model. The initial condition was a light and dark aggregate in contact. The light is the less cohesive aggregate and the dark is the more cohesive. The surface tension ratio (between the dark-medium and light-medium interfaces) matched that determined from independent experiments on neural retinal and heart tissues from chick embryo. As expected, the light tissue slowly engulfs the dark tissue (Figure 4.6). The results shown are for three-dimensional aggregates. In two dimensions, we observe much slower engulfment, because the interface of the three phases is a point rather than a line. Only this point directly experiences the surface tension caused by the light-medium dark-medium energy difference. As time evolves, this point (spin) has to pull the entire

mass of engulfing tissue. In three dimensions, a one-dimensional line of cells drags a two-dimensional monolayer, therefore the cell motions are less constrained.

To compare the results of the experiments with the simulation, we plotted in both cases a length parameter which depends on the geometry of the observed drops. For the sake of simplicity, let us consider the fusion of two drops of a viscous liquid. When placed in contact, the two drops (each of radius a), slowly fuse together to form a larger drop with radius $2^{1/3}a$. Coalescence or fusion is driven by surface tension and damped by viscosity. We may describe the beginning of such fusion for highly viscous liquids by [148]:

$$x^2 = \frac{3a\sigma t}{2\pi\eta}, \tag{4.15}$$

where a is the radius of each drop, t is the time, x is the radius of the circle of contact between the spheres, σ is the interfacial tension, and η is the viscosity of the drop material. The time course of the engulfment of two immiscible, viscous liquids is unsolved. However, when spreading dominates (which is a reasonable first assumption), engulfment is similar to fusion, and Equation 4.15 ought to be an applicable approximation. Then σ would be the interfacial tension between the two tissue types. Heterotypic interfacial tension of tissues is difficult to measure. However, one theoretical model [149] predicts:

$$\sigma_{12} = \sigma_1 + \sigma_2 - 2(\sigma_1\sigma_2)^{1/2}, \tag{4.16}$$

where σ_{12} is the interfacial tension between the two tissues and σ_1 and σ_2 are the surface tensions of the tissues with respect to the suspending medium.

We measured the interface between the two tissues and plotted the length parameter $z = 2\pi x^2/(3a)$ *vs.* the time t. We find that in both cases z grows linearly in time (Figure 4.7; (a) experiment, (b) simulation). This growth differs greatly

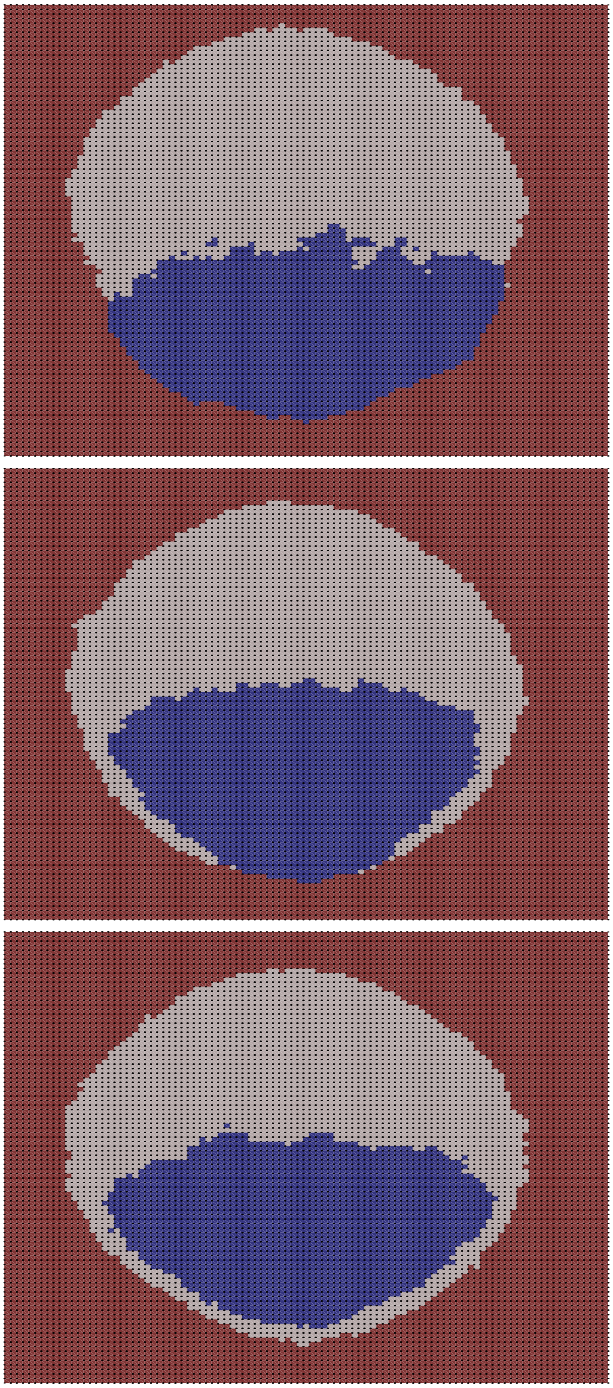

Figure 4.6. Engulfment of more cohesive tissue (dark sphere) by less cohesive tissue (light sphere) as obtained from Potts model simulation. The times are 20, 7000 and 10000 MCS respectively from top to bottom. Figures show two-dimensional projections of three-dimensional aggregates.

from the logarithmic decrease in interfacial length observed during sorting. The energy landscape in this situation is smooth, without the local minima present in the cell sorting case. The linear growth rate is reasonable, since the time evolution is spontaneous.

Calculations of the slopes for the interfacial growth rate may provide a method to convert real time (seconds) to simulation time (MCS), which we could not do earlier. If we know the spatial conversion between μm and pixels (which we can calculate by matching cell sizes in the simulations and experiments), then, equating the respective slopes for engulfment should fix the number of Monte Carlo Steps per second.

We also varied the temperature of the simulations and observed the effect on the rate of growth of the interface. As expected, engulfment slows down with reduced temperature, but does not freeze entirely until we reach T = 4. With values ranging from T = 10 to 32, the growth rate is approximately linear; the slope of the curve decreases as engulfment takes longer to complete (Figure 4.8). We also find that the graphs are not exactly linear; as engulfment proceeds, it gradually slows down. This effect is more pronounced at lower temperatures and could be due to the ever-increasing mass of the light cell layer that the cells at the interface have to drag. At T = 20, we notice that two distinct slopes appear: at later times, the rate of growth is slower.

We expect that the lower temperatures in the simulation correspond to different concentrations of Cytochalasin-B in the experiment. Cytochalasin inhibits membrane fluctuations, while reducing the temperature in the simulations reduces the amplitude of the fluctuations of the simulated cells. We describe in Section 4.4.4 the effect of Cytochalasin on the engulfment of tissues.

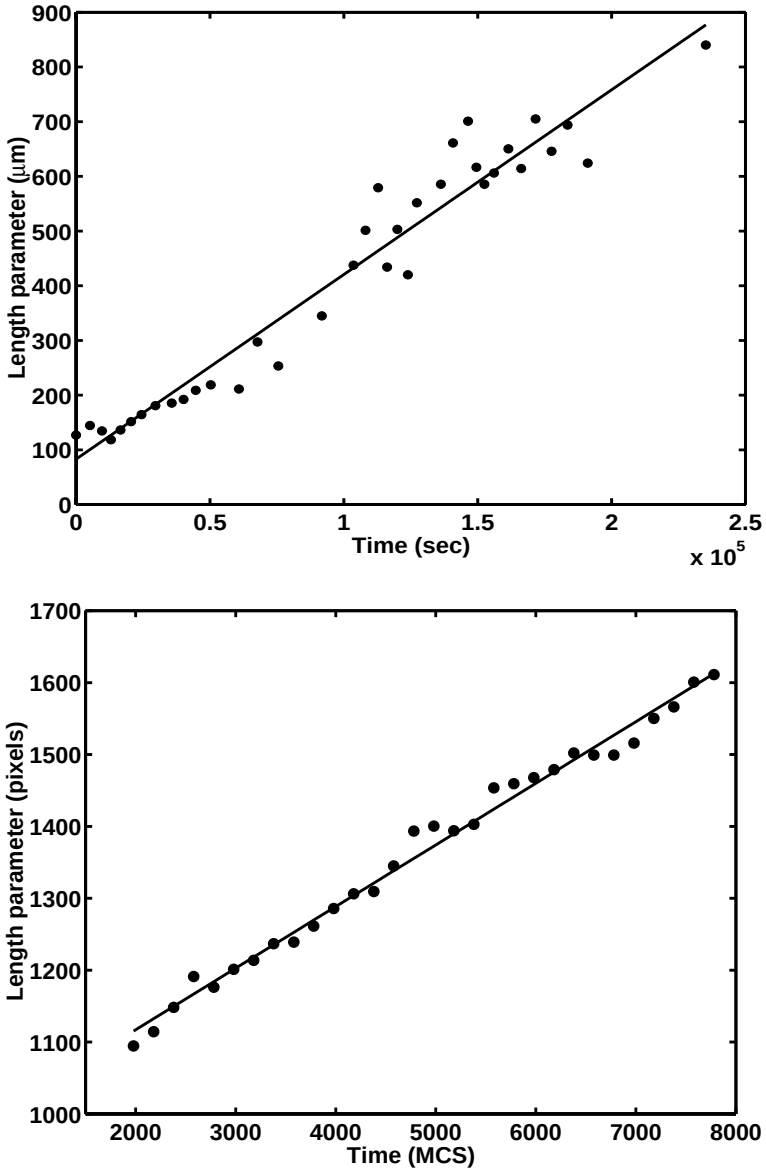

Figure 4.7. Top panel: Length parameter (z) of heterotypic interface during the engulfment of heart and neural tissue from chick embryo. The solid line is a linear fit with a slope of 3.38x10^{-3} μm/s. Bottom panel: Length parameter (z) of heterotypic interface during Potts model simulation of engulfment. The solid line is a linear fit with slope 8.96x10^{-2} pixels/MCS.

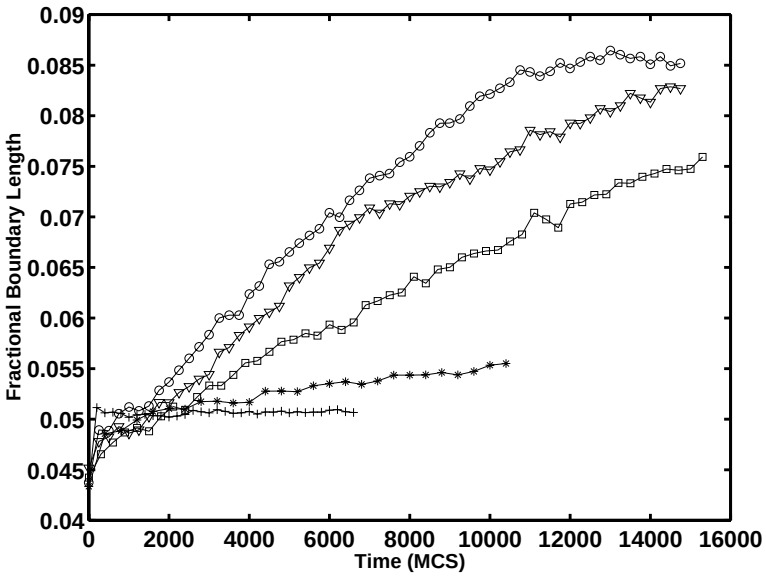

Figure 4.8. Rate of growth of the heteroptypic interface length in simulated aggregates: Effect of varying the temperature; *crosses*: T = 4, *stars*: T = 10, *squares*: T = 15, *triangles*: T = 20, *circles*: T = 25

4.4.3 Liquid Drop

We are unaware of any systematic study of the kinetics of coalescence of two liquid drops. A quantitative comparison of the engulfment of tissues and the coalescence of liquid drops would be very instructive.

For an approximate idea of what to expect, we digitized the images of the time series of the coalescence of oil and water droplets from the paper by Torza and Mason [9]. We calculated the length of the interface between the oil and water as well as the total perimeter of the water droplet. In Figure 4.9 we show the rate of growth of the length parameter z as a function of time. Except for the last point, the length grows linearly in time as predicted by Equation 4.15. (At later times, growth appears to slow down slightly, similar to what we see in simulations). To a first approximation, then, we can describe tissue engulfment as analogous to coalescence of liquid drops. The last step shows a sharp increase in interfacial length as the

oil droplet "swallows" the water droplet. This type of discontinuity resembles the discontinuity when a drop of water from a faucet after swelling gradually, suddenly pinches off.

A more accurate comparison would require the exact hydrodynamic relation for the rate of coalescence in terms of the interfacial tension and the two viscosities. Simulating coalescence in liquids would also be important. Several molecular dynamics and lattice Boltzmann simulations [150] of binary liquids have examined the growth of interfaces. These simulations systematically included the effects of surface tension and wetting on liquid-liquid interfaces [151]. Rupture and fusion of two-dimensional liquid drops have been addressed in [152]. However, we have not found a treatment of the case of two liquid drops suspended in a third liquid. Most previous studies have been two-dimensional due to computational constraints.

4.4.4 Effect of Cytochalasin

If we add Cytochalasin-B to the cell suspension before aggregation, it affects the aggregation properties of the cells and we do not obtain tightly bound aggregates. We therefore added Cytochalasin to the medium after the cells had aggregated to quasi-spheres and aggregates of the two types had fused together. After we placed the aggregates in medium containing Cytochalasin-B, we monitored their progress and that of control aggregates (no Cytochalasin in the medium), as before.

For aggregate pairs that have just started engulfing, Cytochalasin freezes the engulfment and the heterotypic interface stops moving. Initially, when the aggregates fuse, the interface is such that the tissue with higher surface tension is convex and starts to invade the tissue with lower surface tension (Figure 4.10). After the addition of the drug, the interface flattens. The contact angles change at the point of intersection of the three phases and remain static. In the drug-free case, the contact

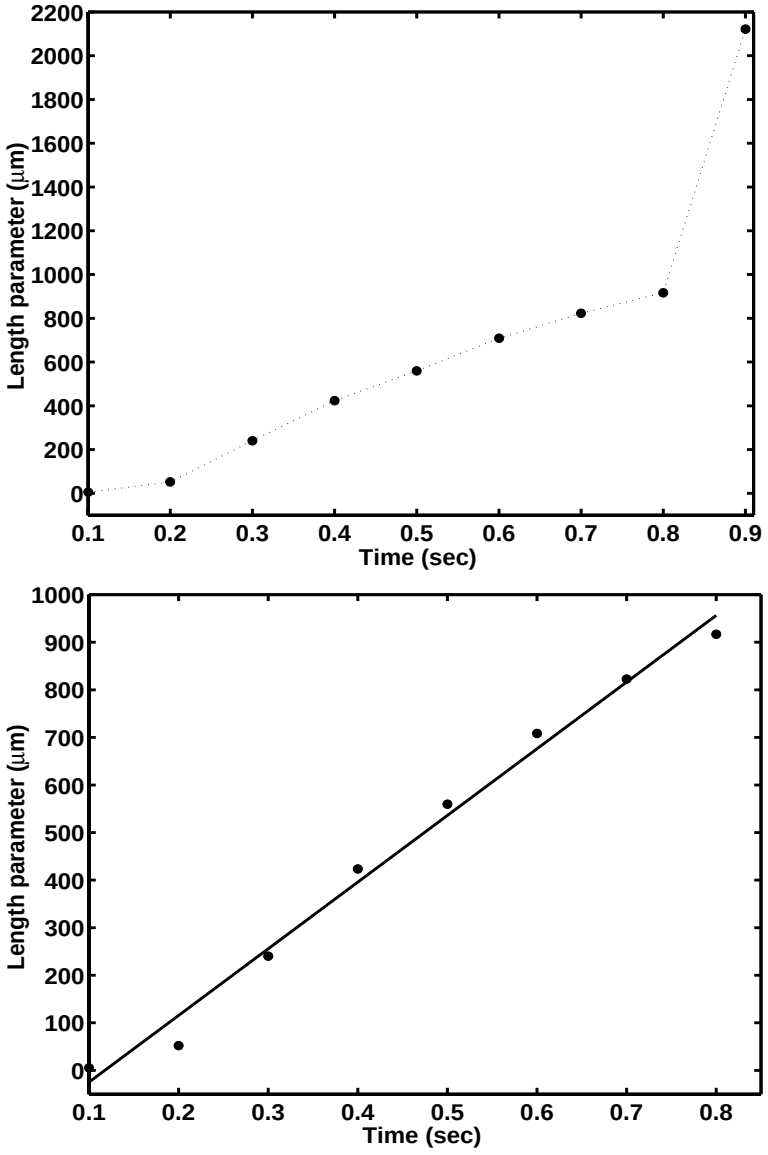

Figure 4.9. Rate of growth of the length parameter (z) for oil-water coalescence. The top graph shows the entire time series. The bottom graph shows a linear fit for the first eight points with a slope of $1.40\text{x}10^3 \mu$m/s.

angle containing the tissue phase with greater surface tension decreases continuously to zero when engulfment is complete. This effect is even more dramatic when we treat a tissue pair that is already halfway through engulfment (Figure 4.10). The invading tissue retracts and the curved interface becomes noticeably flat.

This change in shape of the interface reflects changes in the relative surface tensions of the two tissue pairs. Under normal conditions, the interface between the tissue phases is not in equilibrium, therefore it moves until it achieves equilibrium. Under the influence of Cytochalasin-B, the triple interface between the liquid medium and heart and neural tissues appears to be in equilibrium. Surface tension in tissues is the consequence of adhesion molecules on the cell membrane. The adhesion molecules are transmembrane proteins that also link to the cell cytoskeleton. Cytochalasin-B disrupts the actin cytoskeleton of the cells, which in turn binds to the adhesion molecules on the cell membrane through several actin binding proteins (*e.g.* talin, vinculin, α-actinin). Therefore, disrupting the actin cytoskeleton will interfere with the adhesion properties of cells and change the effective surface tensions of the tissues. Measurements of effective surface tensions of genetically modified cell lines (using the method of Foty *et al.* [83]) have shown that these values indeed change on the addition of Cytochalasin and other cytoskeleton disrupting drugs. However, we have not yet made corresponding measurements on chicken tissues, which would illuminate our results.

4.5 Future Work

The contact angle is a parameter that smoothly decreases to zero during complete engulfment. Further analysis of the experimental and simulation results will characterize the time dependence of contact angles at the interface of the two tissues and

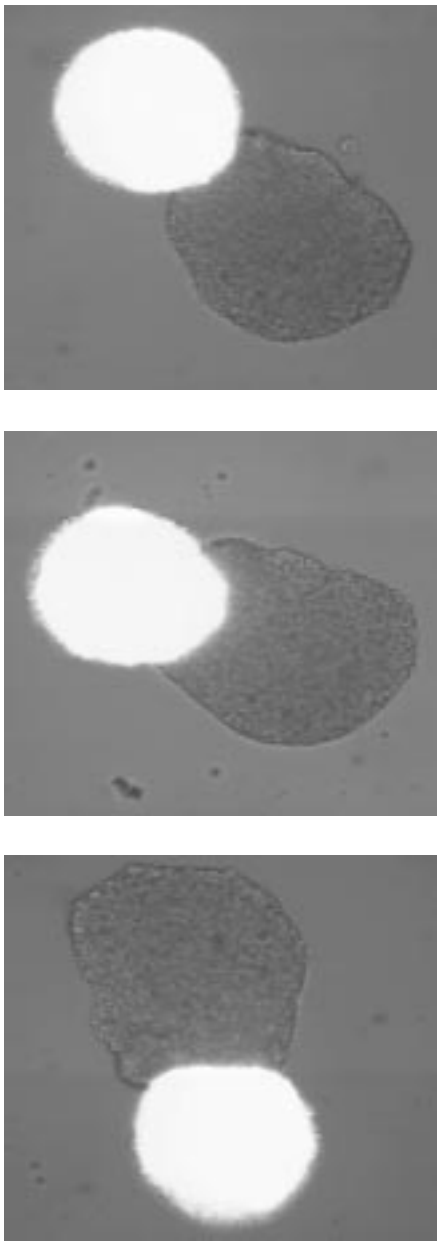

Figure 4.10. Effect of the drug Cytochalasin-B on engulfment. The top two images show the initial stages of normal engulfment. The last image shows the effect of treating the tissues with Cytochalasin-B.

compare with liquids. Repeating our work for different tissue type combinations is important to establish that the liquid analogy indeed holds for a wide variety of tissues. Preliminary experiments with *Hydra* tissues show that ectodermal aggregates engulf endodermal aggregates. The ectodermal tissue should have a lower surface tension as expected from cell sorting and some reaggregation studies. We had more difficulty obtaining quantitative results with *Hydra* because forming clean spherical aggregates was difficult.

The Potts model simulations of engulfment allow us to study a wide variety of tissue behaviors. After establishing a reasonable level of comparison between experiments and simulations, we can use the model to predict the results of experiments that are more difficult to carry out in the lab. Further simulations could study the dependence of engulfment rates on relative surface tensions and on the relative sizes of the two tissue spheres and comparisons with the corresponding experiments. We could also investigate the dependence of the contact angles at the triple-interface on surface tension values.

CHAPTER 5

SINGLE CELL MOTION

5.1 Introduction

In this chapter, we explore the thermodynamics of cell migration and membrane fluctuations in tissues. Qualitatively, the shape and structure of a cell depend greatly on whether it is on a substrate or within an aggregate. The pictures in Figure 5.1 show embryonic chicken cells partially spread out on the surface of a culture plate. Most of the cells have thin, translucent extensions from the main cell body which are called **lamellipodia**. Cells use lamellipodia to attach to the substrate and move as we can see for the cells in the lower left corner and the upper left of the images. The polymerization of actin filaments takes place at the leading edge of such membrane protrusions and drives the cell forward.

In Figure 5.2, we see the group of cells at the corner of an aggregate. At the very edge, a few cells have flattened extensions (lamellipodia) onto the culture vessel whereas cells are rounded up inside the aggregate and their boundaries are hard to distinguish. Cell-cell interactions dominate rather than cell-substrate interactions. Clearly, the dynamics of cell locomotion will depend greatly on the immediate environment.

Only a few authors have studied the behavior of cells within aggregates of other cells [6, 91, 153], and none to our knowledge have studied the cell deformations. Sev-

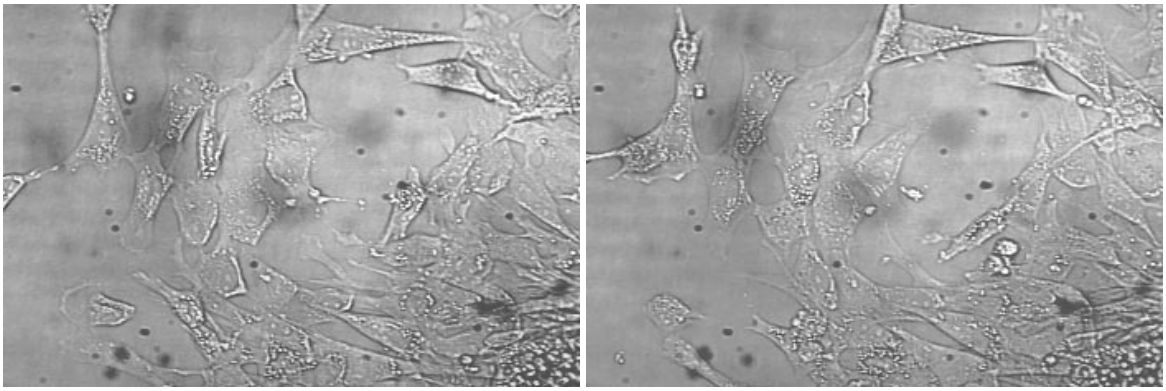

Figure 5.1. Chick embryo cells spread out over the surface of a culture plate (the surface has not been treated with any protein). The images are a few minutes apart. We can see that the cells stretch and move with the help of lamellipodia. Magnification is 1000x.

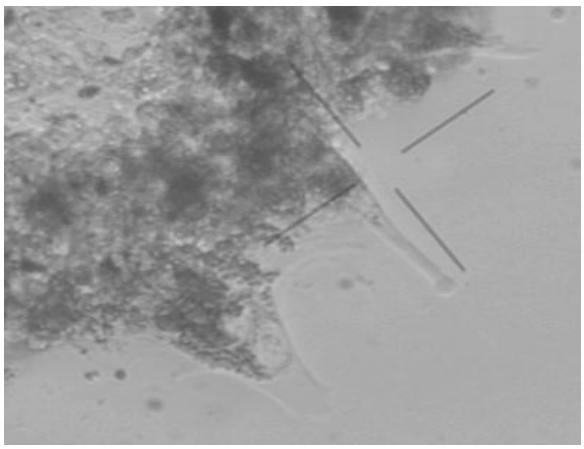

Figure 5.2. One corner of an aggregate of pigmented and neural retinal cells (from chick embryo) showing flat extensions at the edge. Magnification is 1000x.

eral factors influence the motion of cells within tightly packed aggregates of other cells. During *in vitro* cell-sorting or *in vivo* [1] cellular reorganization in embryos, cells directly contact other cells of the same or different types. Cells moving in a compact aggregate of other cells are strongly interacting subunits, where each subunit's (cell's) movement depends on the others. How each cell moves depends strongly on its environment. Many factors, including adhesion (due to adhesion molecules on the surface of all cells), internal cytoskeletal dynamics (polymerization - depolymerization of actin filaments) [45], elasticity of the cell membrane and collective motion due to the close packed nature of the aggregates, affect cell motion. Both displacements and deformations may depend on the individual cell properties as well as tissue properties (cell-cell adhesion [46, 58, 154], correlations due to close-packing of cells in the aggregates). Cells may then migrate as coherent groups (for instance if adhesion is strong), or independently of each other (if homotypic adhesion is weak) [39].

We study, simultaneously, displacements and deformations of endodermal cells in two-dimensional aggregates of dissociated *Hydra* cells. Extensive experiments on sorting out of *Hydra* cells [64, 155] have shown that, from initial random mixtures of the two tissues, endodermal cells sort to the center of the aggregates and ectodermal cells form a surrounding layer (as described in Chapter 3). Indirect measurement of relative surface adhesivity show that the adhesion energies are in the order $E(\text{endo}-\text{endo}) < E(\text{endo}-\text{ecto}) < E(\text{ecto}-\text{ecto})$ [155]. Here, the endo-endo contacts are the strongest [135].

To study the motion of individual cells, Rieu *et al.* tracked cell trajectories within two-dimensional *Hydra* aggregates [6]. They have shown that cell motion during sorting consists both of random and coherent parts. Rounding of the aggregate

and internal endodermal clusters induces coherent motion. We focus on a simpler experiment to analyze the motion of endodermal cells in non-sorting environments (mainly one cell-type aggregates). We could then avoid the large scale coherent flows generated by the sorting and study the microscopics of the motion independent of the global sorting-out.

In this chapter, we describe the statistical properties of the two-dimensional motion of single endodermal *Hydra* cells in two different aggregate types - endodermal and ectodermal. We chose a two-dimensional geometry mainly for ease of observation and the need for long time sequences. We had two main goals: First, very few studies have attempted to obtain a complete physical description (dynamics and thermodynamics) of cell motion. Can a statistical physics framework describe biological cell motion? We know little about the statistical mechanics of single cell motion in different types of cellular aggregates. Do the surroundings affect the observed statistics or do they only alter specific parameter values? Second, we wanted to characterize the dynamics of cell deformations within aggregates, and to learn how they relate to cell displacements.

5.2 Experimental Protocol

5.2.1 Strain and Culture

Hydra viridissima shows good contrast between unstained endodermal and ectodermal cells due to the presence of symbiotic algae inside endodermal cells [156]. We cultured *Hydra* supplied by Dr. H. Shimizu (National Institute of Genetics, Mishima, Japan) at 18°C in Loomis' solution [64], fed them four times a week with freshly hatched *Artemia nauplii* shrimp and transfered them to fresh culture solution five hours after feeding. We starved the animals for 24-36 hours before experiments.

5.2.2 Preparation of Dissociated Cell Aggregates

We carried out mechanical dissociation and reaggregation of *Hydra* cells in dissociation medium (DM) at 4°C according to the method of Gierer *et al.* [64]. After removing the heads and feet from a group of 8-10 animals, we separated the inner and outer layers of the body column using Procaine-HCl [157], and dissociated the tissues using a standard protocol. We minced the tissues separately, almost completely dissociated them into single cells by gentle shearing by repeated pipetting. We held the cell preparation (5-8 ml) at 30 min. in DM at 4°C to sediment and sheared it again. We then filtered it using a $53\mu m$ nylon mesh (NRK, Tokyo, Japan) and centrifuged it at 250 g for 5 min to sediment and collect the epithelial cells. We observed two situations: (A) endodermal cells in an endodermal aggregate and (B) endodermal cells in an ectodermal aggregate. For case (A), we used pure endodermal aggregates and for case (B), we mixed a small percentage of endodermal cells ($\sim 10\%$) into ectodermal aggregates.

5.2.3 Microscopy

We cut the pellets into fragments about 1 mm in diameter and clamped them between cover-glass pairs with 25 μm width spacers to form essentially two-dimensional aggregates. We placed the cover-glass assembly in a Petri dish containing medium and observed it with a confocal microscope (Olympus, IX70-KrAr-SPI). We imaged the auto-fluorescent endodermal cells to track the cells' center-of-mass and membrane fluctuations. Only about 50% of the endodermal cells are autofluorescent when illuminated with light of 568 nm. In regions of pure endodermal aggregates where only some endodermal cells are fluorescent they can be tracked. We ensured that the aggregates under observation were rounded and that the tracked cells were

in the center of the aggregates (to avoid large scale external flows due to rounding of the aggregate).

We recorded the two-dimensional motion of several sets of cells for both case (A) and (B), with each set containing 15-30 cells in the field of view. We took images at intervals of 30 s (1 min in some cases) during 40 to 80 min typically with an Olympus 20X objective lens (10X in some cases). We digitized the images directly using Olympus dedicated software and stored them on the computer. The resolution was about 0.15 μm/pix, finer than needed to track center of mass motion and enough to characterize large scale membrane fluctuations for cells of 10 μm diameter.

5.2.4 Image Processing

We analyzed the images using NIH-Image software to obtain the time series of the center of mass of each cell. We used the x and y coordinates of the center of mass of each cell to study cell displacements and their relevant statistics. To analyze the cell shape changes, we saved images from NIH-Image as text files of intensity images and used FORTRAN and MATLAB to calculate the cell contours and other statistics. We extracted cell contour from the intensity profile as follows: We chose the value for the intensity threshold to be the point at which the profile had maximum slope. We obtained the cell contour by binary thresholding - we considered intensity values above the threshold to be outside the cell and values below the threshold to be within the cell. Determining the cell contour was then simple. To characterize deformations, we studied the amplitude (ϕ) and direction (θ) of maximum and minimum deformation between two successive time intervals. We calculated these quantities as follows: (i) For each time t, we calculated 18 cell diameters $d_i(t)$ along every 10° fixed direction i. (ii) We calculated the amplitude of deformation during

time intervals of $\Delta t = 30$s along the direction i as $\phi_i(t) = d_i(t+\Delta t) - d_i(t)$. (iii) We kept as working parameters the time series of the amplitudes $\phi_{max}(t)$ and $\phi_{min}(t)$, and their corresponding orientations $\theta_{max}(t)$ and $\theta_{min}(t)$.

5.3 Center of Mass Motion

As previously stated, we used unstained *Hydra* endodermal and ectodermal cells. Comparison of transmission and fluorescence images of a single endodermal cell on a solid substrate (Figure 5.3 a,b) shows that the auto-fluorescent symbiotic algae uniformly fill the cytoplasm. The ectodermal cells, only visible by transmission, (c) are lighter than the endodermal cells (a). Within aggregates, cell contours become indistinguishable in transmission at 20X magnification (d). In fluorescence, we can clearly see cell displacements and deformations in time-lapse images (Figure 5.3 e,f). These motions appear random, but watching larger areas of the samples over a longer time, we often observed cell flows and collective motion in some parts of the aggregates.

Figure 5.4 shows the trajectories of a set of endodermal cells in an endodermal aggregate for a typical experiment. Endodermal cells in an ectodermal aggregate show similar trajectories. Some cells seem more diffusive (with many random displacements, as the short arrows in the lower left of the figure show) while others approach ballistic behavior (displacement proportional to time, as the long arrows on the upper right indicate). Several neighboring cells in parts of the aggregate display highly correlated motions. Qualitatively, we can see this correlation in time-lapse images as regions of the aggregate moving together collectively. Looking more closely at individual trajectories, we can see intervals of random cell motion alter-

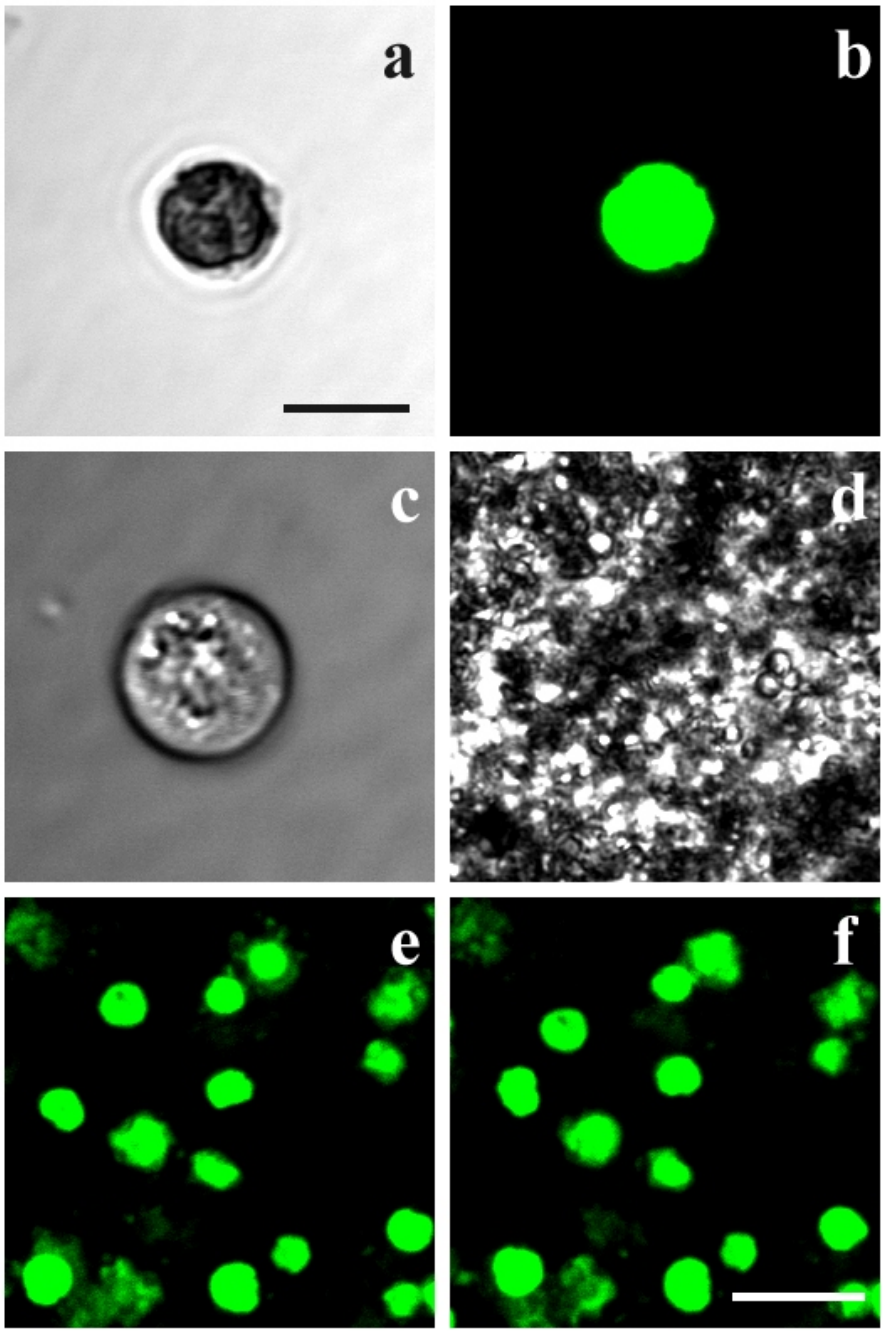

Figure 5.3. Confocal images of *Hydra* cells. Single endodermal cell on a solid substrate observed (a) by optical transmission and (b) by fluorescence; (c) single ectodermal cell by optical transmission; (d) endodermal aggregate observed in optical transmission and (e,f) in fluorescence at 3-min interval. Bars: (a-c) 10 μm, (e-f) 25 μm

nating with correlated motion. Figure 5.5 shows this behavior more clearly, showing fewer cells at a higher magnification.

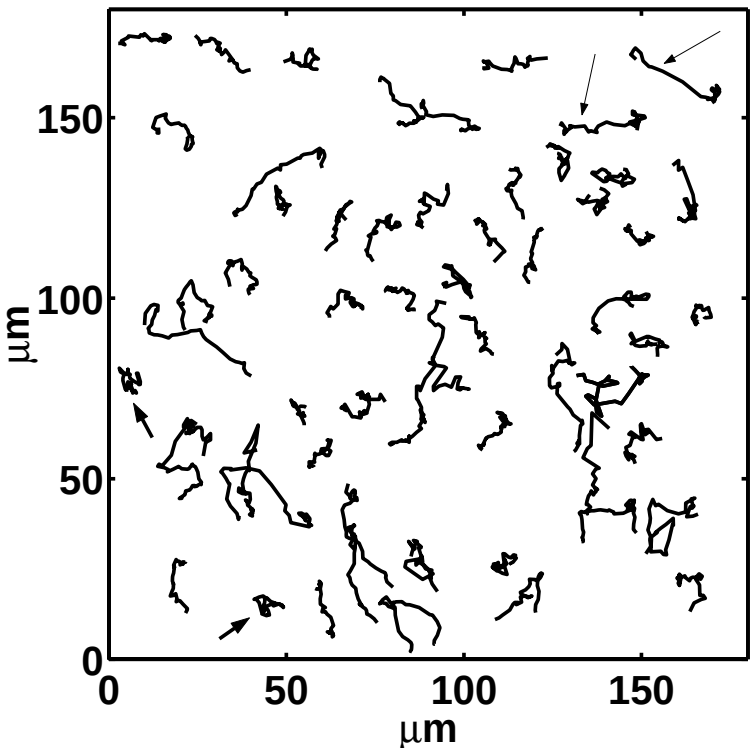

Figure 5.4. Trajectories of endodermal *Hydra* cells in an endodermal aggregate in a field 160 μm x 160 μm. The small arrows on the lower left indicate cells moving randomly and the long arrows on the upper right show cells approaching ballistic motion.

We first characterized the cell diffusion. For each experiment, we averaged the cell displacements, $\langle r^2(t)\rangle = \langle (x(t_0+t)-x(t_0))^2 + (y(t_0+t)-y(t_0))^2\rangle$, over all cells in the set (typically 15 to 30) and calculated the mean squared displacement. The mean squared displacement (or variance) is:

$$\langle\langle r^2(t)\rangle = Dt^{\alpha}, \tag{5.1}$$

where D is an effective diffusivity, and α is an exponent which can be greater than, less than or equal to one. Previous studies of cell motion on substrates [89] or cell

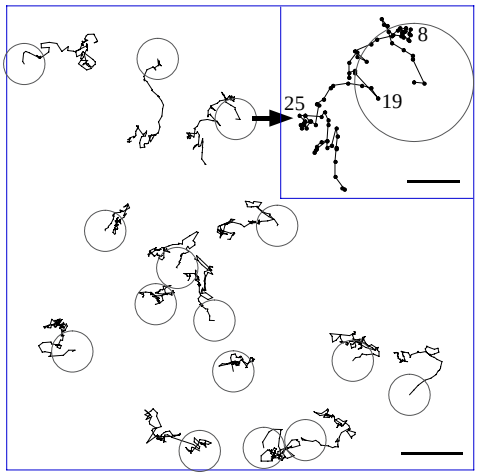

Figure 5.5. Trajectories of 15 endodermal *Hydra* cells in an endodermal aggregate. Images were taken at 30-s intervals for 39 min. Big circles show the approximate cell size and the initial cell position. Bar is 10 μm. Inset: The enlarged trajectory of the cell indicated with an arrow, numbers correspond to time after the beginning of the experiment in min. Bar is 4 μm.

motion in three-dimensional aggregates [91] found normal diffusive behavior ($\alpha = 1$). In our experiments, we obtain $\alpha = 1.23 \pm 0.14$. α is always greater than or close to 1 , indicating that these cells undergo normal to super-diffusive motion. In experiments with α close to 1, cells execute a biased random walk because the drift velocity $V = \langle r \rangle / t$ is non-zero. In fact, the drift is very small compared to $\sqrt{\langle r \rangle^2}$ (less than 10%).

Figure 5.6 shows the variance of displacement as a function of time $\langle r^2 \rangle$ vs. t for sample experiments showing super-diffusion ($\alpha > 1$). These plots show that the effective diffusion constant (y-axis intercept) of the endo-endo (ed) case is smaller than that of the endo-ecto (ec) case. For comparison to normal diffusion, the solid line has a slope of 1.2 while the dotted line has a slope of 1.

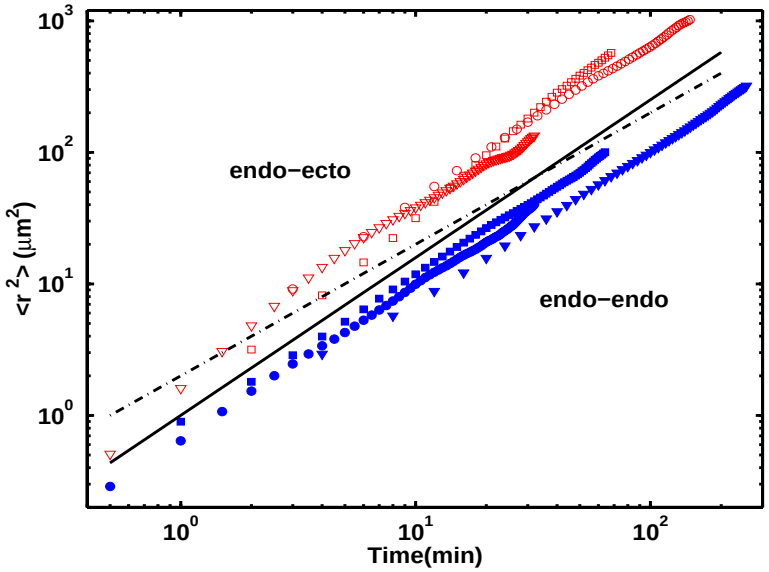

Figure 5.6. $\langle r^2 \rangle$ *vs.* t plot for endo-endo cells (blue filled symbols) and endo-ecto cells (red open symbols). The solid line has a slope of 1.2 and the dotted line has slope 1.

For a typical experiment, Figure 5.7 shows clearly the deviation of the mean squared displacements from normal diffusion represented by the straight line. Fig-

ure 5.8 shows $\langle r^2(t)\rangle$ for two experiments exhibiting almost normal diffusion ($\alpha \sim 1$). We find that the diffusion constant D (slope of the curve) defined as $\langle r^2(t)\rangle = 4Dt$ is always smaller for the endo-endo case. On average, we obtain $D_{ect} = 1.2 \pm 0.5$ μm^2/min and $D_{end} = 0.4 \pm 0.2$ μm^2/min. Consistent with the above results for diffusivity, we find that the endodermal cells have higher RMS speeds in an ectodermal aggregate than in an endodermal aggregate, $V_{ect} \sim 100$ μm/h, $V_{end} \sim 60$ μm/h, consistent with our intuition that cells will move faster in a less cohesive environment. The endo-endo cell contacts are more adhesive than the endo-ecto contacts, possibly increasing the effective viscosity of the cellular medium traversed by the endodermal cell. Recent experiments by Forgacs *et al.* [85] have shown that an aggregate of cells behaves like a viscoelastic medium, with more adhesive cells showing a higher effective viscosity.

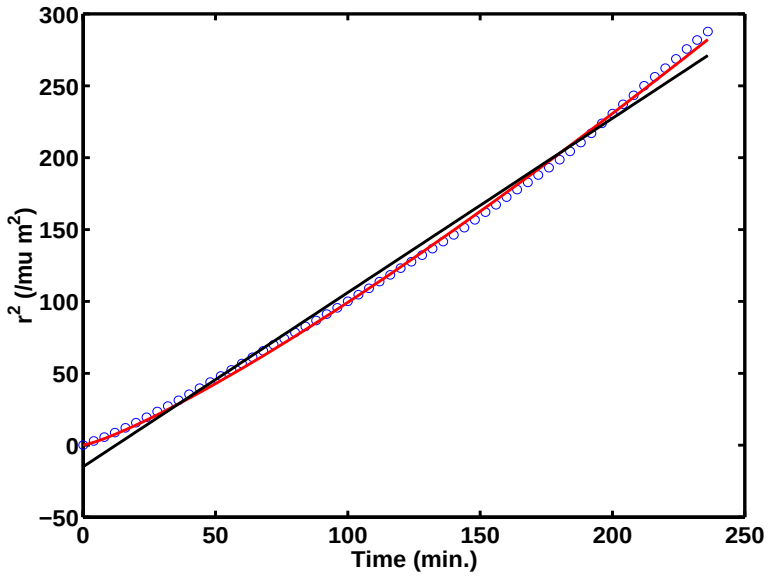

Figure 5.7. Mean squared displacements of a typical experiment showing anomalous diffusion. The circles are experimental data points. The curved (red) line is a nonlinear fit with exponent 1.2, and the straight (black) line is a linear fit.

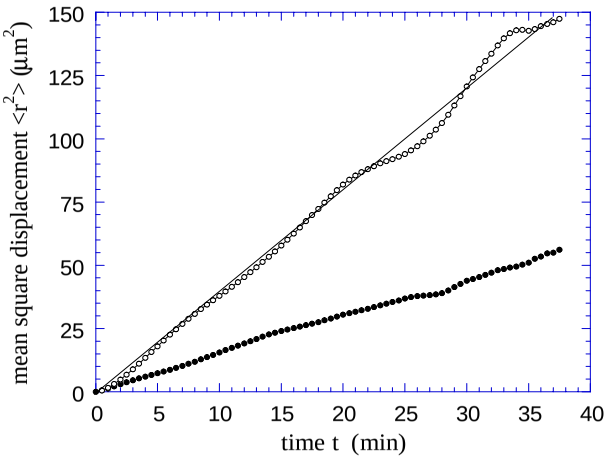

Figure 5.8. Mean squared displacements as a function of time for endodermal cells in an endodermal aggregate (filled symbols) and in an ectodermal aggregate (open symbols)

Most of our experiments showed anomalous super-diffusion. Non-normal (anomalous) diffusion has not been observed before for biological cells. In the next sections we explore the associated thermodynamics.

5.4 Velocity Distributions

We concentrate on the non-Gaussian statistics of the anomalous diffusion and try to determine the cause of the anomaly. Anomalous diffusion occurs in diffusion in turbulent fluids [158], diffusion of micelles [159], surface growth and diffusion in porous media [160] and in super-cooled liquids. The anomalous exponent can either be $\alpha < 1$, corresponding to **sub-diffusion**, or $\alpha > 1$, which corresponds to **super-diffusion**. Super-diffusion (as in our experiments) can be of two kinds: **Levy-type** (broad distributions with diverging first or second moments) and **correlated type** (due to long-range spatial or temporal correlations).

We analyze our data for the presence of correlations, which may cause the observed anomalous diffusion. If the correlations are very short-range (decaying more

rapidly than t^{-1}), they do not affect the dynamics and diffusion is normal. For example, finite-range correlations, like those that decay exponentially, result in a persistent random walk, where the time constant of the decay determines the persistence time. On the other hand, if the correlations are long range, *i.e* when $C(t) \sim t^{-k}$ with $k < 1$, they modify the typical behavior of the variance, enhancing diffusion. In our experiments, we calculated the temporal auto-correlation function of the velocities, $C(t)$, and fit it to a power law. For large t, we observe $C(t) \sim t^{-k}$. For those experiments which present collective behavior and anomalous diffusion (exponent $\alpha > 1$), the power law fit gives $k < 1$ ($k \sim 0.9$). For other experiments with normal diffusion, the correlations decay very rapidly: k is either greater than one or the decay is exponential. Figure 5.9 shows the data for long range correlations with a power-law fit. Spatial correlations can also change the dynamics. In a space dimension, d, larger than 2, only long range correlations give rise to anomalous diffusion. But if $d \leq 2$, even weak spatial correlations can induce anomalous diffusion [161]. Figure 5.10 shows short-range spatial correlations of the cell velocities. The correlation length is on the order of 10-15 μm.

To study the underlying thermodynamics of the motion, we calculated the probability distribution function of the velocities. For small time scales ($\Delta t = 30$s), the velocity distributions are non-Gaussian. Figure 5.11 shows a histogram of the speeds with a Maxwellian fit. The experimental distribution has a heavier tail, with significantly more high velocity events than predicted by Maxwell-Boltzmann thermodynamics. However, if we look at longer time scales (2 to 3 min), the velocity distribution approaches a Gaussian for those experiments which display normal diffusion.

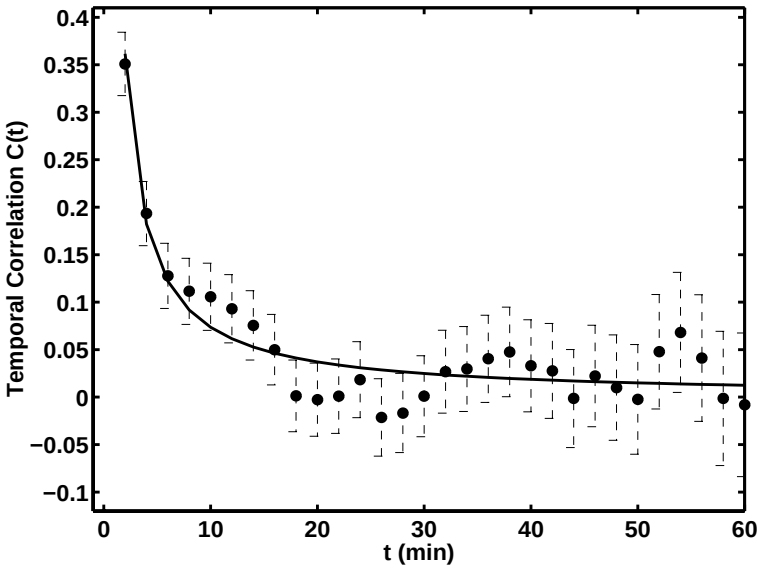

Figure 5.9. Temporal correlation of the velocity $C(t)$ for experiments showing collective motion of endodermal cells. The solid line is a fit to a power law.

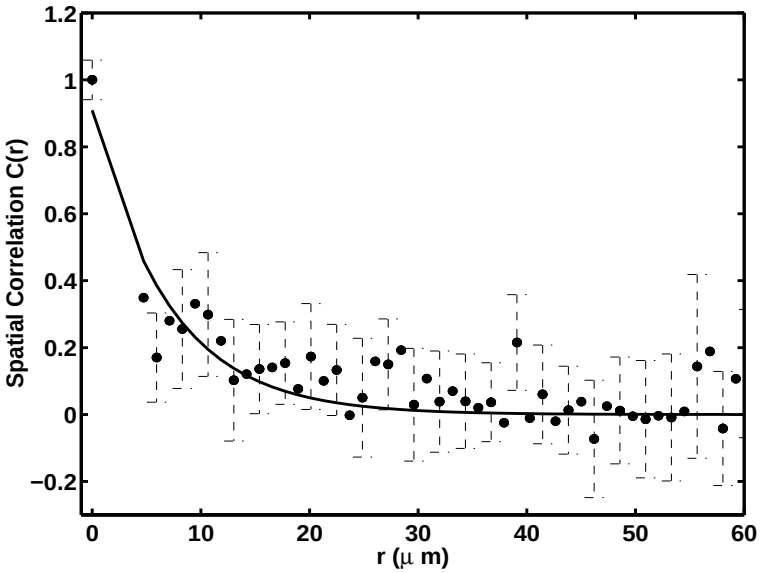

Figure 5.10. Spatial correlation of the endodermal cell velocities for a typical experiment. The solid line is a fit to an exponential.

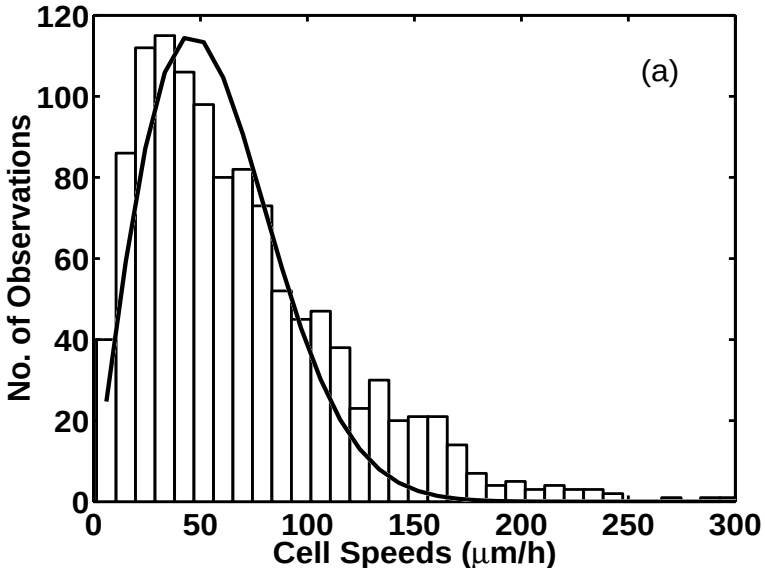

Figure 5.11. Histogram of endodermal cell speeds. The solid line is a fit to the Maxwell distribution of speeds for a Brownian particle: $F(V) = aV\exp(-bV^2)$.

We also calculated the histogram of angles between orientations of the velocity vector at successive observation times, as shown in Figure 5.12. A large percentage of events have angles less than 30°, rather than the flat distribution which would result from randomly distributed successive orientations. Thus the cell velocities have correlated direction and speed components.

To quantify the degree of deviation from Boltzmann thermodynamics, we calculated the non-Gaussian indicator (or *flatness* factor) of the velocity PDF,

$$\chi = \frac{\langle (v_x - \langle v_x \rangle)^4 \rangle}{\langle (v_x - \langle v_x \rangle)^2 \rangle^2}. \tag{5.2}$$

For a Gaussian PDF, $\chi = 3$. The *flatness* of the experimentally obtained velocity PDF is around 10, much greater than 3, showing that the velocity distribution is non-Gaussian.

Zanette and Alemany have developed the thermostatistical foundation of anomalous diffusion for Levy-type distributions [162] and Tsallis, Bukman and Borland for

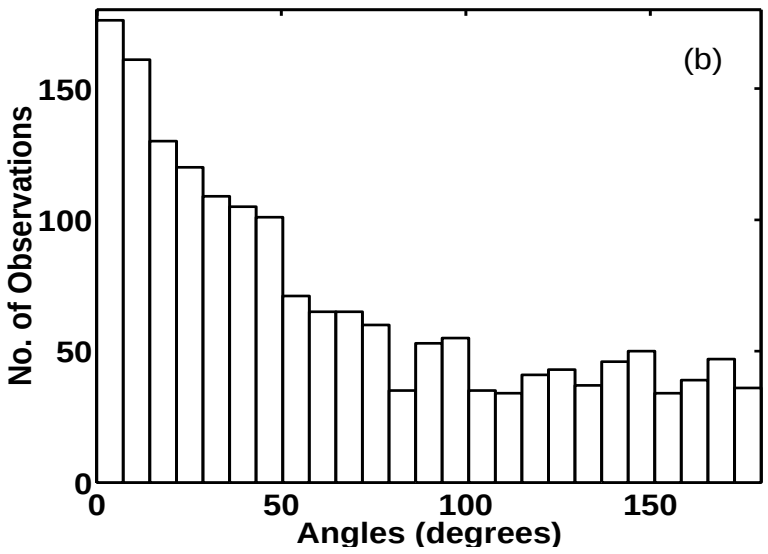

Figure 5.12. Histogram of angles between succesive orientations of the displacements of endodermal cells

correlated-type diffusion [163, 164]. Generalized thermodynamics derives from the non-extensive entropy [165]:

$$S_q = \frac{1 - \int dx[f(x)]^q}{q-1}, \tag{5.3}$$

where q is a parameter quantifying the degree of non-extensivity and $f(x)$ is the probability distribution function. The limit of $q \to 1$ recovers the regular Gibbs entropy. Optimizing S_q under normalization and mean energy constraints yields a generalized probability density function as well as the q-distribution of velocities [166]:

$$F(\mathbf{v}) = A_q[1 - (1-q)\frac{\beta m v^2}{2}]^{\frac{1}{1-q}}. \tag{5.4}$$

Again, $q \to 1$ recovers regular Maxwell-Boltzmann thermodynamics with Gaussian velocities.

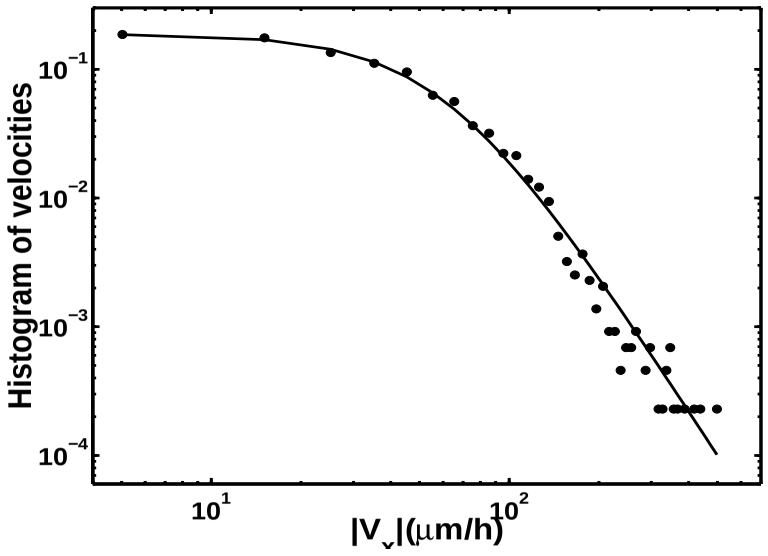

Figure 5.13. Probability distribution function for the horizontal component of velocity for endodermal cells in an ectodermal aggregate. The solid curve is a fit to the function $F(V_x) = \frac{a}{(1+bV_x{}^2)^c}$.

The experimental velocity distributions for both the endo-endo and endo-ecto cases have the functional form of the q-distribution of velocities:

$$F(V_x) = \frac{a}{(1 + bV_x{}^2)^c}. \tag{5.5}$$

We fit the x and y components of the velocity vectors (V_x and V_y) with the above form, Figure 5.13.

From the fits, we obtain q using $q = \frac{c+1}{c}$. Averaging the results of several experiments, we find $q \sim 1.54 \pm 0.05$. That we should be able to fit our data so well with a theory that has been quite successful in explaining physical phenomena like flow in porous media and turbulence is remarkable. The key is the presence of large correlations regardless of their cause. A generalized statistical physics framework can explain cell motion in aggregates. How can we distinguish whether non-Gaussian statistics arise due to correlated or Levy-type anomalous diffusion? Pure Levy

flight dynamics have a broad distribution of elementary displacements X during Δt without any correlated jumps:

$$P(X,t) = 1/X^a \quad \text{with} \quad a < 3. \tag{5.6}$$

In correlated-type anomalous diffusion, the distribution $P(X,t)$ can be narrow ($a > 3$) or Gaussian, with a non-linear growth of the variance. We measured the exponent a for the probability distribution of cell displacements and obtained $a \sim 4$. This value of a is consistent with $q \sim 1.5$ if we approximate the Tsallis form of $P(X,t)$ by a power law for large X and shows that our experimental distribution is narrow rather than broad.

The relation between q and the exponent α of the variance further elucidates which dynamics gives rise to the observed statistics. We consider an alternate way of obtaining probability distribution functions for anomalous diffusion - by solving the Fokker-Planck equations. A diffusion equation with fractional derivatives can describe Levy-type diffusion [167]. On the other hand, a non-linear Fokker-Planck equation [163, 167] has been proposed for correlated anomalous diffusion. The explicit form of the non-linear Fokker-Planck equation (FPE) is:

$$\frac{df^\mu}{dt} = -\frac{d}{dx}(Kf^\mu) + Q\frac{d^2}{dx^2}(f^\nu). \tag{5.7}$$

Interestingly, the solutions of the nonlinear Fokker-Planck equation are same as the distributions that optimize the generalized entropy [164, 163].

For correlated anomalous diffusion, $q = 1 + \mu - \nu$ and $\alpha = \frac{2\mu}{\mu+\nu}$, giving $\alpha = \frac{2\mu}{2\mu-q+1}$ [163]. The experimentally obtained values are $\alpha = 1.24$ and $q = 1.54$, corresponding to $\mu = 1.4$ and $\nu = 0.86$. On the other hand, for Levy-type diffusion, $\alpha = \frac{q-1}{3-q}$ [163]. For the observed value of q we should obtain $\alpha = 0.33$, while our

experimental $\alpha \sim 1.2$. Thus, cells display correlated-type rather than Levy-type anomalous diffusion.

For a physical explanation of this result, we can consider the underlying microscopic dynamics which ultimately gives rise to a macroscopic level of description. Borland [164] has shown that the Langevin equation (which represents the microscopics) corresponding to the nonlinear Fokker-Planck equation is of the form:

$$\frac{dx}{dt} = K(x,t) + \sqrt{Q} f(x,t)^{(\nu-1)/2} \eta(t), \tag{5.8}$$

where the Fokker-Planck Equation 5.7 gives the evolution of f. The f-dependence of the Langevin equation implies the presence of feedback from the macroscopic level of description (f) to the microscopic dynamics. We can think of the f-dependent term as a phenomenological description of the complex interaction of the particle (in this case, the cell) with the bath (the cellular environment).

A calculation of the Hurst exponent for a process showing anomalous diffusion can determine whether it arises from a non-linear Fokker-Planck Equation or fractional Brownian motion. The Hurst exponent (H) is defined as in [26]:

$$\frac{R}{S} = (\frac{\tau}{2})^H, \tag{5.9}$$

where the range R is given by:

$$R = \max X(t,\tau) - \min X(t,\tau), \tag{5.10}$$

with X equal to the accumulated departure from the mean of the stochastic increment ζ within the time interval τ,

$$X(t,\tau) = \sum_{i=1}^{t} [\zeta(i) - \langle \zeta \rangle_\tau], \tag{5.11}$$

and the standard deviation S is:

$$S = \left(\frac{1}{\tau} \sum_{t=1}^{\tau} [\zeta(t) - \langle \zeta \rangle_\tau]^2 \right)^{1/2}. \tag{5.12}$$

If $H = 0.5$, the process is either regular Brownian motion or correlated anomalous diffusion with the non-linear Fokker-Planck Equation. On the other hand, $H > 0.5$ implies a Levy-type diffusion. We calculated the Hurst-exponents for the cell displacement time series of our experiments (we have to calculate H separately for each cell trajectory, and then average over all cells). Averaging over all the experiments, we obtain $H = 0.66 \pm 0.18$, within error of $H = 0.5$, again supporting the correlated anomalous diffusion picture.

5.5 Potts Model Simulations of Cell Motion

We have successfully used simulations based on the Potts model to describe global cellular pattern formation phenomena like cell sorting and engulfment (as described in the previous chapters). Can we use the same model to describe the motion of single cells? Understanding the limits of its validity is important. Mombach *et al.* [91] attempted to compare the motion of single chick embryonic cells in aggregates with results from simulations. They found that pigmented cells from chick embryos perform a pseudo-random walk in neural aggregates and have a Gaussian velocity distribution. Simulations with the original model (Hamiltonian 2.7) give similar results. Velocity distributions are Gaussian and diffusion is random. Figure 5.14 shows the distribution of cell speeds of a light cell in a light-cell aggregate. A Maxwell distribution function fits the observations quite well.

However, we encounter some serious discrepancies when we try to compare the experimental results presented in this chapter with simulations of single cells within aggregates. In the simulations, cells move faster in a more cohesive (dark) envi-

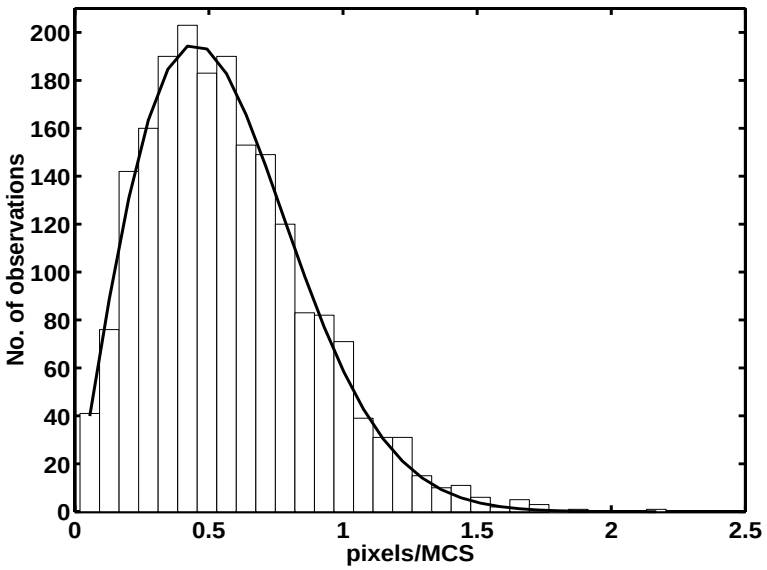

Figure 5.14. Probability distribution of cell speeds in a two-dimensional simulated light cell aggregate. Simulation parameters are: $J(2,2) = 2, J(1,2) = J(2,1) = 11, J(1,1) = 14, J(1,3) = J(3,1) = 16; \lambda = 1, T = 20$. The solid line is a fit to the Maxwellian distribution.

ronment than in a less cohesive (light) one. Figure 5.15 shows the mean squared displacement as function of time in simulations for a dark (more cohesive) cell in a dark aggregate and a dark cell in a light (less cohesive) aggregate. Diffusion is faster in the dark aggregate ($D_{dd} = 14.4\text{x}10^{-3}$ pix^2/MCS) than in the light aggregate ($D_{dl} = 6.8\text{x}10^{-3}$ pix^2/MCS). Biological cells, on the other hand, move **slower** in a more cohesive (endodermal) aggregate than in the less cohesive (ectodermal) aggregate.

To make the simulations more realistic, we modified the Hamiltonian and the simulation parameters as discussed in Chapter 2, to use negative energies (Equation 2.12). The surface energy values are negative and an additional term constrains the surface area (perimeter in two dimensions) of each cell. We find that, in simulations with the new Hamiltonian, if the perimeter constraint is the same for both

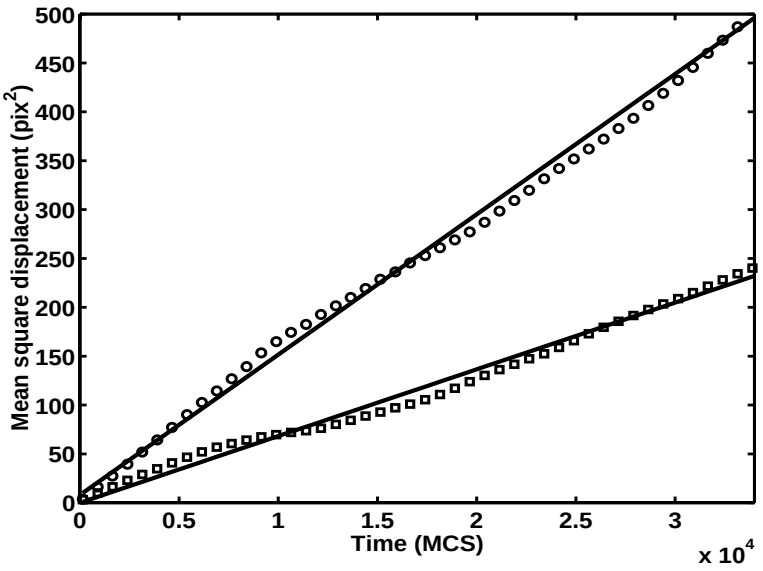

Figure 5.15. Two-dimensional Potts model simulation of cell diffusion with positive energy Hamiltonian. Mean squared displacements as a function of time for a dark cell in a dark aggregate (circles) and in a light aggregate (squares)

cell types, dark cells typically have a slightly greater deviation from their target perimeter than light cells. Dark cells tend to have greater boundary length due to their more negative surface energy values. Therefore, they lose energy by increasing boundary length but gain energy due to the perimeter constraint. Since the energy terms balance out, the two cell types diffuse at the same rate. To fix this problem, we weighted the perimeter constraint (Λ) so that both cells deviate equally from their target perimeters. With a larger value of Λ, the dark cells diffuse slower than the light cells, consistent with the experimental observations. Figure 5.16 shows mean-squared-displacement curves for simulations using the negative energy Hamiltonian. The diffusion constant is $D_l = 10.3\text{x}10^{-3}$ pix^2/MCS in the light aggregate and $D_d = 5.99\text{x}10^{-3}$ pix^2/MCS in the dark aggregate. We can view the perimeter constraint as a tension of the cell membrane, and could possibly be different for different cell types.

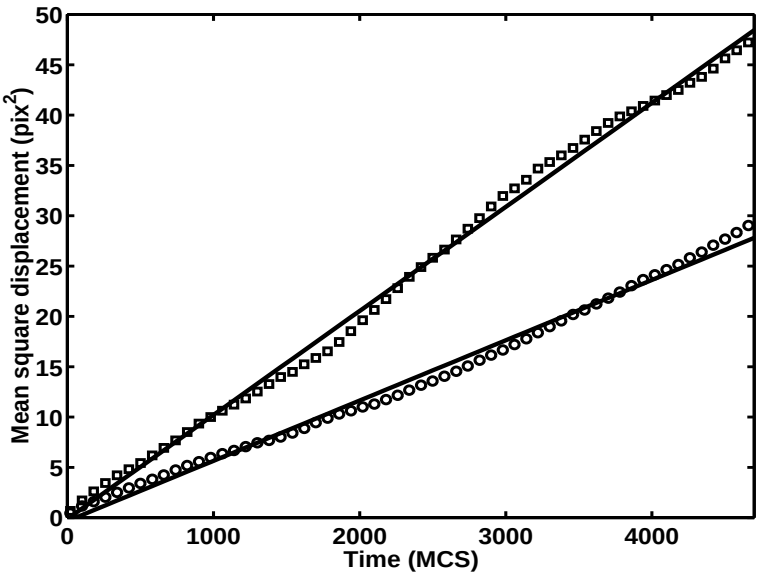

Figure 5.16. Two-dimensional Potts model simulation of cell diffusion with negative energy Hamiltonian. Mean squared displacements as a function of time for a dark cell in a dark aggregate (circles) and in a light aggregate (squares)

Our experiments with *Hydra* also show that cells in a tissue do not move randomly. We observe anomalous diffusion and non-Gaussian velocity distributions due to correlations in the cell motion. Potts model simulations may be useful in elucidating the mechanisms by which these correlations arise. We modified the Hamiltonian to introduce temporal correlations in the cell velocities (Equation 2.13, as explained in Chapter 2). We would like to determine whether introducing correlations leads to anomalous dynamics and non-Gaussian thermodynamics. Further, can temporal correlations induce spatial correlations and if so, to what extent?

Figure 5.17 shows the distribution of cell speeds for simulations with induced velocity correlations. The parameters are as given in the figure caption; λ is the area constraint and η is the velocity constraint. The probability distribution is clearly non-Maxwellian. We see a greater occurrence of high velocity events as observed in the experimental graph (Figure 5.11). Indeed, the presence of velocity correlations

changes the observed thermodynamics. We are characterizing the motion further in terms of cell diffusion, angle distributions and the Tsallis formalism of non-extensive thermodynamics.

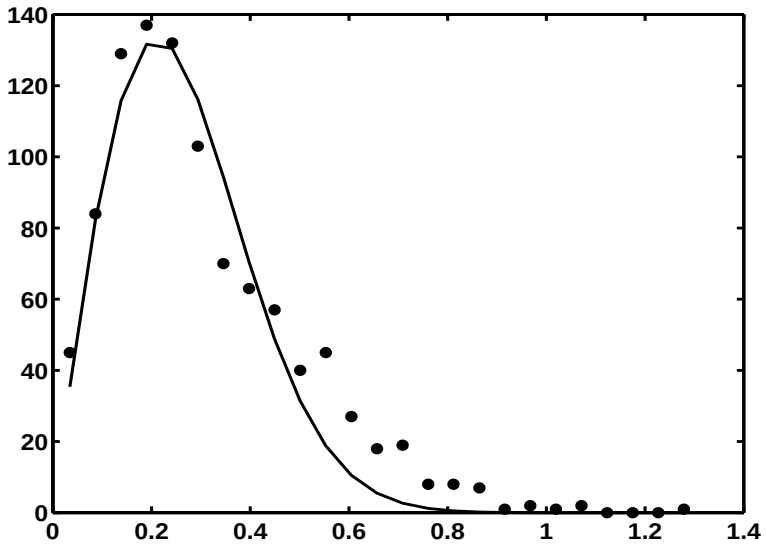

Figure 5.17. Probability distribution of cell speeds in a two-dimensional simulated light cell aggregate. The simulation parameters are: $J(2,2) = 2, J(1,2) = J(2,1) = 11, J(1,1) = 14, J(1,3) = J(3,1) = 16; \lambda = 0.5; \eta = 3500; T = 20$. The solid line is a fit to the Maxwellian distribution for cell speeds.

5.6 Cell Deformations

Cell motion intimately couples to the membrane protrusions driven by cytoskeletal activity. A complete understanding of the cell center of mass dynamics requires detailed study of these membrane fluctuations. In this section, we investigate the role of cell membrane deformations in the movement of cells within aggregates. From images of the cell contours, we observed that we could approximate most of the cells as quasi-spheres. Figure 5.18 plots the contours at 1 min intervals of an endodermal cell within an ectodermal aggregate. The overall shape changes slowly but some bumps appear frequently (see for instance in Figure 5.18a or Figure 5.18e

on the left side). The cell contours are always smooth and do not present filopodia or ruffles. Some cells do not change their shape during long periods of time even when they move long distances

In order to characterize these deformations, we first study the time series of cell expansion amplitudes ϕ_{max}, contraction amplitudes ϕ_{min} and directions. Figure 5.19 shows the time series of ϕ_{max} and ϕ_{min} for the endodermal cell whose trajectory is depicted in the inset of Figure 5.8. On average, ϕ_{max} and ϕ_{min} are symmetric with similar amplitude, indicating that the cell area is roughly constant during the analysis as expected. More interesting are the estimates of the mean amplitudes of deformations in the two kinds of cellular aggregates. On average, over 5 cell data sets in both cases, we obtain $\langle\phi_{max}\rangle_{end} = 0.29$ μm in endodermal aggregates and $\langle\phi_{max}\rangle_{ect} = 0.45$ μm in ectodermal aggregates. Hence, as we previously found for diffusion constants and instantaneous velocities, the amplitude of deformation is higher in ectodermal aggregates (1.5 times higher). Figure 5.19 shows the time series of the amplitude of the center of mass displacement. This displacement is always larger or equal to ϕ_{max}. It also shows large fluctuations, while the deformations are rather uniform. Large displacements corresponding to the persistent periods in the inset of Figure 5.8 do not seem to correlate with large ϕ_{max}.

We calculated the time correlation of the cell deformations following the method of Schneider *et al.* [168]. Their analysis is for fluctuating vesicles in a liquid medium. We consider a cell in an aggregate to be analogous to a vesicle in a fluid, with cytoskelatal activity playing the role of an effective temperature and the surrounding cellular aggregate behaving like a viscoelastic liquid with an effective viscosity arising mainly due to the friction caused by cell-cell adhesion. (The effect of cytoplasmic and intrinsic membrane viscosity is negligible [109]). Despite important differences

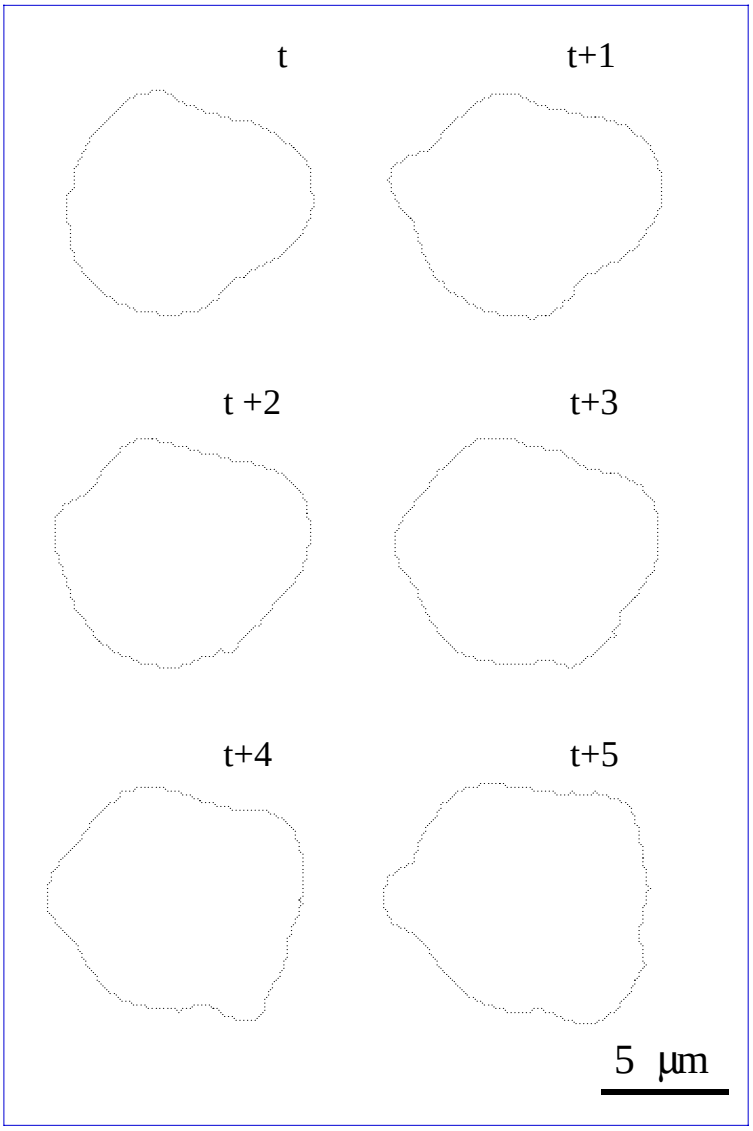

Figure 5.18. Contours of an endodermal cell within an endodermal aggregate every 1 min. Bar = 5 μm

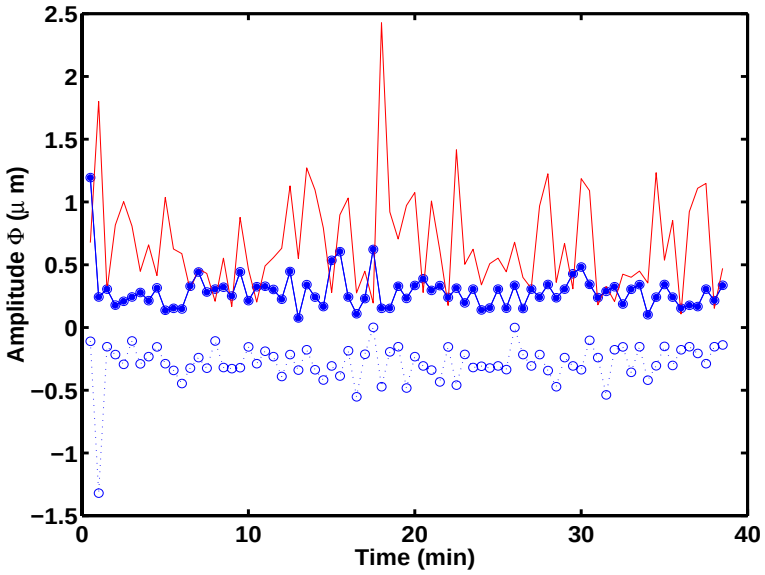

Figure 5.19. Time series of the cell extension amplitude (filled circles), the cell contraction amplitude (circles), and the center of mass displacements (solid line)

between vesicles and cells the analogy provides a simple, physical framework to quantify cell membrane fluctuations. We calculate the cell deformation as $r = d(\theta) - d(\theta + \frac{\pi}{2})$ which is the difference between perpendicular diameters of the fluctuating cell. The time correlation function is $R(t) =< r(t_o + t)r(t) >$, where the average is over the 18 diameters i and over t_o. For the sake of simplicity, we studied only the ellipsoidal deformation, but results are qualitatively the same for other kinds of deformation. Figure 5.20 shows $R(t)$ for a cell within an endodermal aggregate. It is reasonably exponential, decaying as $A\exp(-t/\tau)$ for both aggregates, indicating that deformations decorrelate beyond a characteristic time τ. The two parameters A and τ represent repectively the mean squared amplitude and correlation time of the deformations. A measures the driving force for fluctuations and τ measures the effective viscosity that damps the relaxation of the membrane. We find $A_{ect} = 0.55 \pm 0.25\ \mu\text{m}^2$, $\tau_{ect} = 3.2 \pm 2$ min for the endo-ecto case and $A_{end} = 0.35 \pm 0.20\ \mu$

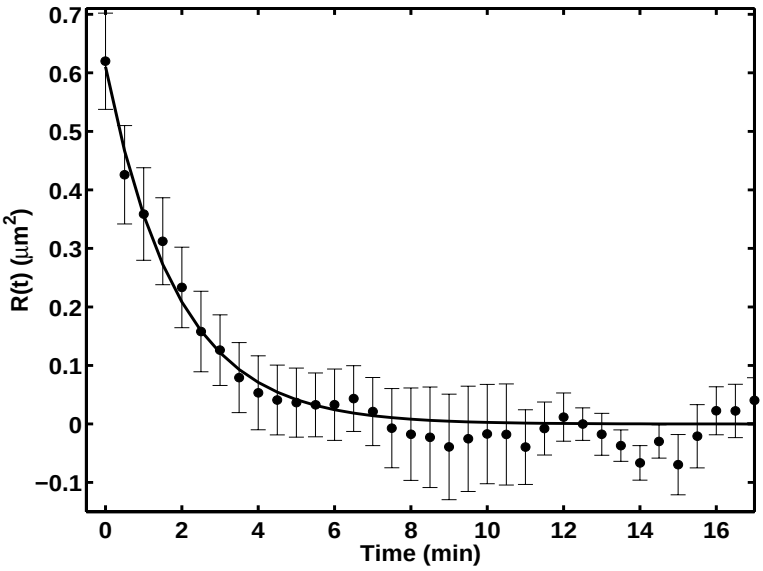

Figure 5.20. Temporal correlation of the cell deformations, $R(t) =< r(t_o + t)r(t) >$ as a function of time interval for an endodermal cell within an endodermal aggregate

m^2, $\tau_{end} = 5.1 \pm 2$ min for the endo-endo case (values averaged over 5 cells in both cases). Interestingly, the correlation time for the deformations is approximately the same as the correlation time for the displacements.

In Figure 5.21A, we present the histogram of $|\theta_{max} - \theta_{min}|$. This angle is the difference between the directions of extension (θ_{max}) and contractions (θ_{min}). The distribution extends between 30^o and 100^o indicating the presence of different kinds of deformations. Unexpectedly, the maximum of the distribution is not at 90° (ellipsoidal deformations) but rather at 60°. These deformations seem to correspond to the appearence of small bumps in the cell contours of Figure 5.18. In order to study whether the deformation and center of mass displacement directions correlate, we plotted the histogram of $|\theta_{max} - \theta_{disp}|$ where θ_{disp} corresponds to the direction of displacement. The distribution is approximately flat (Figure 5.21B). The variations are within the statistical error. We obtain the same kinds of histograms for $|\theta_{min} - \theta_{disp}|$, $|\theta_{max}|$, $|\theta_{min}|$ and $|\theta_{disp}|$ respectively. We conclude that our data set does not

show any correlations between the directions of displacements and deformations at the same time. We also studied cross-correlations between θ_{disp} at time t_o and θ_{max} or θ_{min} at time $t_o + t$. Again, we did not find any evidence of correlation.

5.7 Discussion

We have shown that in addition to a regular biased random walk, cell motion in aggregates shows a novel type of statistics. Cells move faster in a less adhesive cellular environment, although the type of observed dynamics is the same in both kinds of surroundings. All observed cells show non-Gaussian probability distributions and correlations, analogous to physical examples of spatial or temporal correlations, *e.g.* in turbulence, porous media and granular materials. Both temporal and spatial correlations play an important role in changing the dynamics. The physics resembles a granular material with very high packing density. Recent experiments and simulations of two-dimensional vibrated beds of granular media showed anomalous diffusion with exponent ~ 1.2 and non-Gaussian velocity distributions [169, 170]. Obvious differences are that cells are deformable while grains in general are not. Cells are self driven, whereas grains need an external driving driving force (*e.g.* vibrated beds). We can attempt to construct an analogy by thinking of the aggregate as a dense collection of soft, deformable objects being driven by internal noise (cellular machinery). Molecular dynamics simulations of deformable matter can provide the basis for more accurate modeling.

Since cells are in such close contact with one another, they cannot move independently. The motion of each cell depends on its intrinsic machinery but also depends on the motion and influence of neighbors via adhesive interactions, inter-cellular signaling, and geometrical constraints due to the densely packed configuration and the

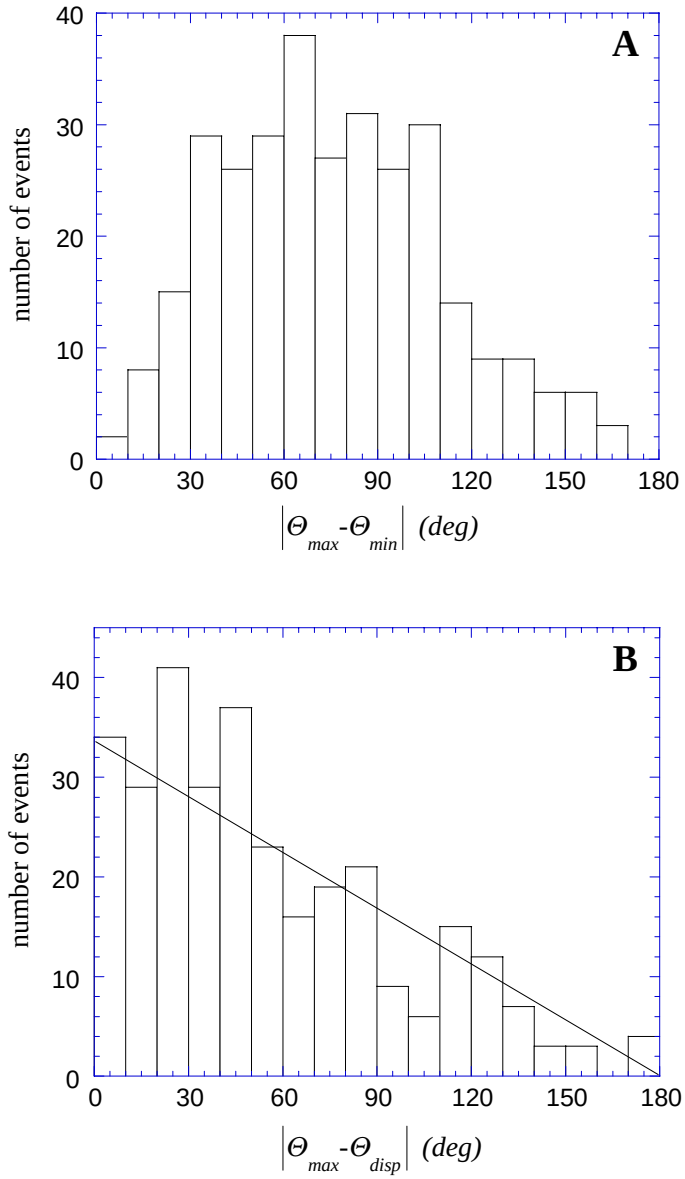

Figure 5.21. (A) Distribution of the difference between directions of extension and contraction. (B) Distribution of the difference between directions of extension and center of mass displacement

collective behavior of the surrounding domain. We observe, in the same experiment, several different types of dynamics. Cell motion appears to consist of "intervals" of random and correlated motion. The natural inhomogeneity of the cells, *e.g.* regions of high and low adhesion, leads to fluctuations in the packing density and the strength of interactions, possibly giving rise to the different modes of behavior. The strong interactions between cells induce correlations and collective motion. In some cases, pure ectodermal aggregates show a spiralling motion similar to that observed in *Dictyostelium* cells [171] and bacterial colonies [172, 173, 174].

Vicsek *et al.* have constructed a model of "self propelled particles" in which the particles locally interact by choosing at each time step the averge direction of motion of their neighbours with some random perturbation added [175, 176, 177]. Their model reproduces a wide variety of cooperative phenomena from bacterial colonies and flocking of birds to traffic movements. However, the model is for point particles and does not take into account the actual shape and plasticity of cells. Dimensionality plays an important role in causing cooperative motion. A diffusing particle in two dimensions returns to the vicinity of any point in its trajectory with probability 1, while the probability for the same to occur in three dimensions is less than 1 [177]. Therefore, clusters of particles are more likely to interact and order in two dimensions, than in three dimensions.

We can hypothesize the following scenario for cell motion. The motion of each cell exhibits: 1) Regimes where it is trapped in a cage of its nearest neighbors, all of which are fluctuating, 2) The cell has a finite probability of a sudden escape from the cage. Escape corresponds to the almost linear parts of the observed trajectories. The above process could also occur at different length scales *e.g.* trapping and escape of a cluster from surrounding clusters. The escape probability could depend

on the adhesion and the membrane fluctuation amplitude; the size of typical clusters formed could also depend on the cell-cell adhesivities. Spatial correlations between cells due to such mechanisms may lead to temporal correlations. More careful work is needed to characterize the difference in spatial correlation functions for the two cell types considered. The role of cell membrane protrusions driven by internal actin dynamics is a key factor in understanding the various motile processes. Non-Gaussian behavior is a consequence of microscopic non-linearity, and, of memory, *i.e.* an incomplete time scale separation between the "macroscopic" diffusing variable and the "microscopic" dynamics [178]. In our case, this mixing could results from the similar time scales of membrane fluctuations and center-of-mass displacements.

We also find that both the diffusion constant D and the deformation amplitude ϕ of the same endodermal cells depend on the cellular environment (endo or ecto). The direction and amplitude of cell deformation seem uncorrelated with the direction and amplitude of cell displacements. Thus, unlike the situation of an isolated cell on a substrate [88, 89], the displacement of a cell within an aggregate is not caused only by its own deformations, but is rather the result of the forces exerted by the cellular environment. The situation in a sense is similar to Brownian motion in liquids. The Brownian particle (cell, in our case) moves randomly because it receives random kicks from liquid molecules (other cells). The difference between the two cases is that the liquid molecules have uncorrelated random fluctuations (thermal bath) while in our case strongly interacting and deformable units (the cells) constitute the bath and the fluctuations may not be uncorrelated. No time scale separation exists between the random deformations of the cells and their random displacements as suggested by the correlation times obtained from Figures 5.9 and 5.20.

However, the comparison with Brownian motion is useful in order to discuss the physical parameters governing cell motion and cell deformations within aggregates. Using Stokes law for the viscous drag of a particle moving in a viscous fluid relates the diffusion constant to the temperature T and viscosity η:

$$D = k_B T / 6\pi\eta R, \tag{5.13}$$

where k_B is the Boltzmann constant and R the particle radius. For the cells, T is of course an effective temperature. $k_B T$ is the fluctuation energy arising from cell activity (actin polymerization dynamics) and from the energy released during bond formation. The viscous dissipation arises from the energy required to rupture bonds and to deform the cells (membrane rigidity and cytoplasmic viscosity). We expect the viscous dissipation to be larger in the more cohesive tissue because it costs more energy to break bonds. From our experiments, we indeed find the expected result that the diffusion is three times smaller in the more cohesive endodermal aggregates. A difference in fluctuation energy of the cellular bath could also contribute to the observed difference in diffusion constant. The deformation amplitude and the instantaneous velocity which are 1.5 and 1.3 times smaller respectively in endodermal aggregates may reveal this difference.

To qualitatively explain our observations, let us consider the following cellular model. Each cell can fluctuate a little, but, as it is bound to its nearest neighbors, these fluctuations do not generally produce center of mass displacement (trapped regime). When the pressure exerted by the neighbors becomes significant in some direction, the cell has a finite chance to escape from its cage and to find a new local configuration with new neighbors. The pressure could arise from many simultaneous deformations in the same direction - causing localized synchrony. In the less cohesive ectodermal aggregates, as the probability to break bonds and change local

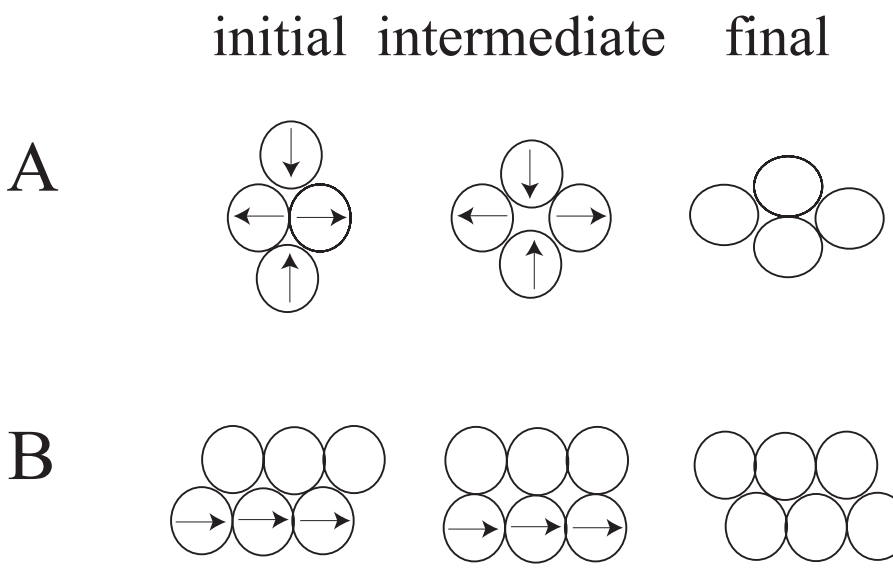

Figure 5.22. Two possible mechanisms of local configuration change are: (A) T1 process; and (B) sliding of cell layers.

configuration is higher, the diffusivity is higher. We examine in Figure 5.22, two possible changes of configuration. For both, we have drawn initial, intermediate and final configurations. Clearly, the intermediate situation costs a lot both in terms of contact surface between cells (and thus in terms of the number of adhesive bonds) and in terms of local density. Then, once a local reorganization starts from the initial configuration, the next favorable configuration is the final one. In between, the central cell has moved by roughly a half diameter in process A and by one diameter in process B. This motion is likely to be directed (persistent regime). We believe that the higher proportion of correlated cells in ectodermal aggregates results from the higher probability of changing configuration (due to lower adhesion). In addition, we note that both processes depicted in Figure 5.22 require cooperative motion of the cells, but process B also requires parallel displacements of the cells within the moving layer. Such a process may explain the spatial correlations of the velocity and also the origin of the cell flows often observed in the aggregate.

In conclusion, the relevant parameters driving cell motion within aggregates are: (i) The energy barrier associated with the rupture/formation of adhesive bonds; and (ii) The packing constraints. Future work will involve modeling cell motion within aggregates taking into account these parameters and investigating the mechanisms which lead to coherent motion. Specifically, analysis of cell motion at different time scales, experiments with different cell type combinations (ecto-ecto, ecto-endo) and more detailed experiments to characterize the cooperative phenomena will be important.

CHAPTER 6

MEMBRANE TENSION OF TUBULOVESICULAR NETWORKS

6.1 Introduction

Tension in the plasma membrane and the membranes of other cell organelles could be a global parameter that the cell uses to control physically plasma membrane dynamics like secretion and endocytosis, cell-shape and cell motility. Recent observations indicate that decreasing membrane tension stimulates endocytosis and increasing tension stimulates secretion [179, 180]. Membrane tension could also be an important regulator of membrane trafficking between intracellular organelles, like the Golgi and the endoplasmic reticulum (ER). Chapter 1 gives a brief description of their functions in the cell which consist mainly of vesicular membrane traffic of proteins between the nucleus and the plasma membrane. If different organelles have different membrane tensions, then tension driven flow would play an important part during trafficking.

A dramatic example of a phenomenon in which tension could play an important part is the rapid movement of the Golgi into the ER caused by the drug Brefeldin A (BFA). BFA is a fungal antibacterial reagent which inhibits the transport of proteins out of the ER and interferes with a dynamic membrane-recycling pathway between the ER and Golgi. One explanation of the rapid Golgi movement into the ER could be that the tension in the ER is much greater than the tension in the Golgi. The membrane tension would then rapidly draw the Golgi membrane into the ER when

the membranes come into contact by fusion. When a cell is treated with BFA, the Golgi membrane starts tubulating (extends long tubulovesicular processes along microtubules) and is rapidly drawn into the ER [181, 182]. Sciaky *et al.* [183] have observed a tubule network extending throughout the cytoplasm appear and persist for 5-10 min until the Golgi contents merge rapidly into the ER within 15-30 sec. Their analysis of the kinetics suggested that transport of lipids and proteins from the Golgi to the ER is not purely diffusive. The mechanism of transport may be analogous to a wetting or adsorptive phenomenon in which tension driven membrane flow supplements diffusive transfer of Golgi membrane into the ER. However, no direct evidence supports tension driven flow. Measurement of the membrane tension of these two membrane types separately can provide some answers.

The two main goals motivating the work presented in this chapter were to separate the Golgi and ER membranes to form networks and measure the membrane tension of both membrane types. *In vitro* reconstitution of ER and Golgi network formation and dynamics is useful to study the mechanical properties of these networks. Several previous studies have successfully formed networks *in vitro* both from ER [184] and Golgi [185] membranes. The dynamics and morphology of these reconstituted networks are very similar to those in living cells [186]. Mechanical measurements on these simplified cell-free networks clarify their properties in real cells. In the present study, ER and Golgi networks form on a microtubule mesh through the action of motors pulling the membrane into thin long tubes along the microtubule tracks. Microtubule polymerization can also drive the formation of membrane networks [187]. In this situation, the membranes attach to growing plus end microtubules which pull them into thin tubes. In living cells, a combination of

these two mechanisms probably causes the formation of the reticular structure of the ER.

The mechanical properties of the plasma membrane has been studied extensively but no previous work has investigated the properties of membranes from intracellular organelles. We formed tubulovesicular networks of both Golgi and ER membrane fractions from Chick Embryo Fibroblasts (CEFs). We characterized their morphology and membrane tension. To measure the tension of these membranes we used optical tweezers, used quite extensively to study the properties of the plasma membrane [180, 188], to pull membrane tethers *in vitro*. We use laser tweezers to trap beads attached to the membranes and pull tethers perpendicular to the membrane branch to determine the tether force. Ours is the first measurement of the tension of intracellular organelles, providing direct evidence that tension driven flow may be responsible for membrane traffic from the Golgi to the ER.

6.2 Experimental Methods

6.2.1 Formation of Membrane Networks

We obtained internal membranes from CEFs, using standard protocols. Appendix C describes the detailed protocols ([189]). We discarded the plasma membrane, nuclei and mitochondria leaving only the intra-cellular membranes and the cytosol. We used differential centrifugation to separate the Golgi from the ER membranes. We obtained a pellet of the heavier membranes (H-fraction) using a low speed spin of the diluted membranes; a high speed spin resulted in the lighter vesicles (L-fraction). We resuspended these fractions in buffer and used them for network formation and fluorescent assays. We discarded endogenous microtubules from the cytosol which we used undiluted in the experiments to provide motors. We formed tubulovesicular networks in a flow chamber between two glass coverslips. We introduced membrane

fractions with motors and ATP at appropriate concentrations on a bed of microtubules randomly attached to the coverglass surface. We observed networks about 1 - 2 hr after incubation at 37°C. We made our observations using video-enhanced differential interference contrast (DIC) microscopy at room temperature. For the fluorescence imaging of networks, we used a cooled charge coupled device (CCD) camera.

6.2.2 Measurement of Tether Force

After 30-60 min of incubation of the membrane extracts in the coverslip chambers, we mounted the coverslip on an aluminum coverslip holder using silicone grease and observed under the microscope. We flowed beads (0.5 μm in size) coated with a suitable antibody into the chamber along with motor-containing supernatant and appropriate concentrations of GTP, Taxol and Mg-ATP. (We coated beads with either anti-kinectin antibody, which binds to the ER membranes or Wheat Germ Agglutinin (WGA), which binds to the Golgi membrane). We trapped the bead with the laser, placed it on one branch of the network and allowed it to bind to the membrane by holding for a few seconds. Then we pulled it at a constant velocity perpendicular to the network branch. The straight branch first formed a **V** and then a **Y** as a tether extended (as discussed in Section 6.3). We held the tether static for 20 to 40 s, video-recorded the whole sequence and later digitized it for analysis.

6.2.3 Calibration

We calculated the force of the optical trap by viscous drag through the aqueous medium in the microscope focal plane. We trapped a single bead in the optical tweezer (sufficiently above the surface to eliminate viscous coupling to the coverslip). We generated the viscous force by oscillatory motion using a piezo-ceramically driven

stage at a constant velocity (using a sawtooth voltage signal). The relation $F = 6\pi\eta av$ gives the Stokes drag, where η is the viscosity of the medium, a is the radius of the bead and v is the velocity. Different velocities correspond to different forces. We tracked the position of the bead using a tracking program and obtained a linear force-displacement graph to calculate the calibration constant for the trap stiffness.

6.2.4 Data Analysis

We used ISEE software from Inovision, Inc. to digitize and analyze the recorded tether pulling sequences. This particle tracking program calculates the centroids of beads with a precision of up to a few nanometers. To measure the diameter of the network branches, we took orthogonal scans across the membrane tubules and across beads of known diameter (500 nm). The area under the intensity profile curve gave the values for the relative intensities [190]. We calculated the radius of each type of tubule (R_t) by multiplying the radius of the bead (R_b) by the square root of the ratio of the intensity of the tubule (I_t) to that of the bead (I_b). The intensity is proportional to the square of the diameter, $R_t = R_b\sqrt{\frac{I_t}{I_b}}$.

6.3 Results

6.3.1 Network Formation

Figure 6.1 shows an example of a typical membrane network from CEFs. An amorphous aggregate of membrane which adheres to a microtubule meshwork on the glass coverslip is the precursor of the network. Microtubule dependent motors (kinesin and dynein) attach to regions of the membrane and move along a stationary microtubule providing the force to draw out tubular branches. In the absence of motors, we do not observe any tubular extensions, either from the Golgi or ER membrane aggregates. This absence suggests that the microtubule motor force it-

self creates tubules from a free membrane with no preferred curvature, as opposed to motor proteins simply guiding pre-existing membrane extensions. New membrane branches form when another active motor contacts and moves along an intersecting microtubule. Figure 6.2 shows a cartoon for the possible scenario [184]. When two membrane tubules intersect each other, they fuse and relax to a configuration connected by trigonal vertices with 120° angles between the branches to minimize the local energy. The fusion and relaxation results in a reticular network of long membrane tubules on a bed of randomly intersecting microtubules. Networks do not form either in the absence of motors or ATP, clearly indicating that microtubule-dependent motors are necessary for network formation.

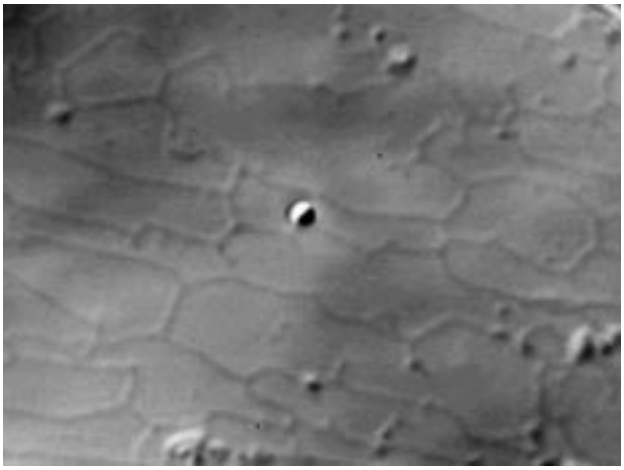

Figure 6.1. DIC image of a typical membrane network. The white sphere is a bead of 500 nm diameter.

For 1-2 hr after incubation, the growing network is an extremely dynamic structure. The membrane tubules exhibit many different types of motion - tubule growth and branching, polygon closure and sliding. Branching occurs when a new tubule is drawn out from one branch of the pre-existing network, first bending the branch to form a vertex from which a new tubule grows. Tubule formation suggests appli-

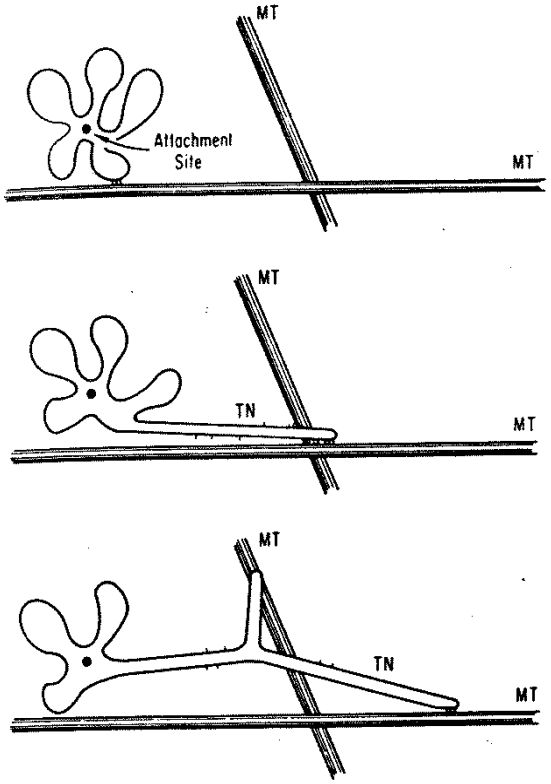

Figure 6.2. Hypothesis for network formation from membrane aggregates. Membranes are present as amorphous aggregates and vesicles on a bed of microtubules (MT). Molecular motors attach to the membrane at specific attachment sites, move along the microtubules and pull out long, tube-like membrane tethers which constitute the tubulo-vesicular network (TN). A tube may branch when another motor pulls a new tether along an intersecting microtubule.

cation of a force by a single motor or a group of motors at the tip. The growing tip either fuses with another branch or retracts to its origin. In some instances, pre-existing polygons shrink in size due to movement of one of the branches and eventually disappear, causing a local rearrangement of the network configuration but no long-range changes. Sliding occurs when a junction (vertex) moves along a tubule and can lead to polygon-closure (shrinking and disappearance of a polygon) as well as other local rearrangements. All these types of motion have also been observed in the ER of living cells [186], indicating that our cell free network is a good model to study ER structure and function. After a few hours, the whole structure stabilizes and the growth and dynamics of tubules ceases, as the network achieves a steady state configuration. The network is interconnected and can stretch unbroken over hundreds of microns. The tubulovesicular structure attaches to the underlying bed of microtubules only at some discrete points, for unknown reasons, possibly due to inactive motors or other attachment proteins. Between the points of attachment, the tubules undergo undulations due to Brownian motion, showing that they are not bound to the coverglass surface.

6.3.2 Tether Force

To measure the tension of these membranes, we use laser tweezers to pull membrane tethers with the help of beads attached to the membrane. We introduce protein coated beads into a flow chamber containing networks, trap a bead and place it on a membrane branch. After a few seconds it binds to the membrane. We pull the bead perpendicular to the membrane branch to determine the tether force. As we pull the bead out, it first bends the membrane into a **V** shape and then branches into a **Y** as a tether pulls out. Figure 6.3 shows such a sequence, exactly analogous to the branching of a tubule due to motor movement during the network growth phase. As

the new tether forms, membrane flows into the tether from the surrounding branches of the network. Since the network is interconnected, it essentially acts as an infinite reservoir of membrane material, especially due to the presence of large membrane aggregates which do not exhaust during network formation. The tether is of the same radius as the surrounding network and the triple point at the **Y** relaxes to a 120° angle. We could pull beads for long distances laterally across the branches, indicating that the network is indeed an interconnected fluid.

We pull tethers at a constant speed from the membrane tubules and hold them stationary for 30-60 seconds while measuring the static tether force. After the tethers form from the membrane network branches, they rapidly retract when we release the bead from the laser trap, indicating that a significant force pulls the membrane in the tether back into the network. Figure 6.4 shows a schematic diagram of the forces on the bead. The membrane tether exerts a force pulling the bead towards the network branches, this force displaces the bead from the center of the laser trap. To bring the bead back to the center, the trap exerts a restoring force on the bead which balances the tether force. We can calculate this force by measuring the displacement of the bead from the trap center. We measured the tether force for tethers formed from both fractions H and L. Figure 6.5 shows graphs of typical displacement curves for both fractions. We can obtain the force by multiplying the displacement by the force-displacement calibration constant. As the bead slowly pulls the membrane tube into a **V**, the force felt by the bead keeps increasing, until it reaches a maximum. At this point, the tether forms, and the force relaxes to a value corresponding to the static tether force (the horizontal part of the data curve). We measured forces from several samples over different parts of the network. For each of the fractions, we found a fixed value of force maintained throughout the

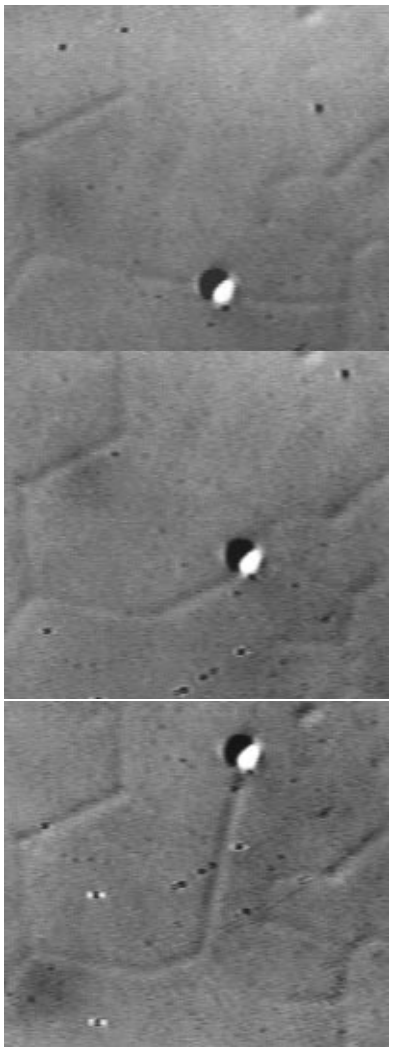

Figure 6.3. DIC image of a typical tether pull sequence. We hold the bead in the optical trap and pull it orthogonal to the membrane tubule. The bead is 500 nm in diameter.

entire network. The tether force for the H-fraction is 11.43 ± 1.4 pN whereas the tether force for the L-fraction is 18.62 ± 2.8 pN (see Table 1). We find that membrane networks formed by the lighter fraction exert significantly higher force than networks formed by the heavier fraction.

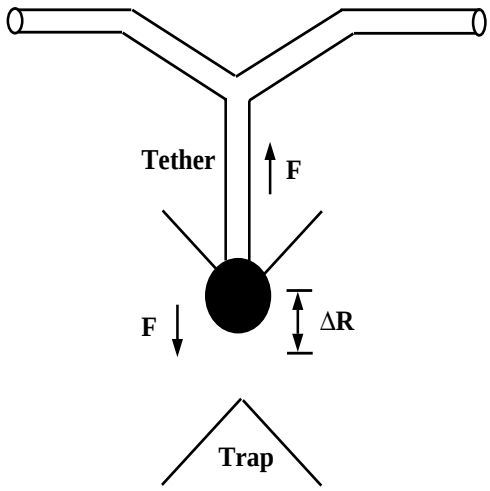

Figure 6.4. Schematic of a tether pull showing the displacement (ΔR) of the bead in the trap. The force of the laser tweezers on the bead balances the tether force.

6.3.3 Identification of Membrane Type

After network formation, we recorded several tether-pulls from a sample and studied the sample using fluorescent staining to identify the membrane type present in that fraction. We double-labeled each sample with (1) Ribosome receptors (found on ER) coupled with Texas Red (TR) stain and (2) WGA (Wheat Germ Agglutinin, which binds preferentially to components in the Golgi membrane) coupled with FITC (Fluorescein iso-thio-cyanate). Figure 6.6 shows a typical image for membrane networks from the L-fraction: the same field of view is observed first with a fluorescence filter for Ribosome-TR staining (Figure 6.6 - top panel) and then immediately for WGA-FITC staining (Figure 6.6 - bottom panel). As is evident from

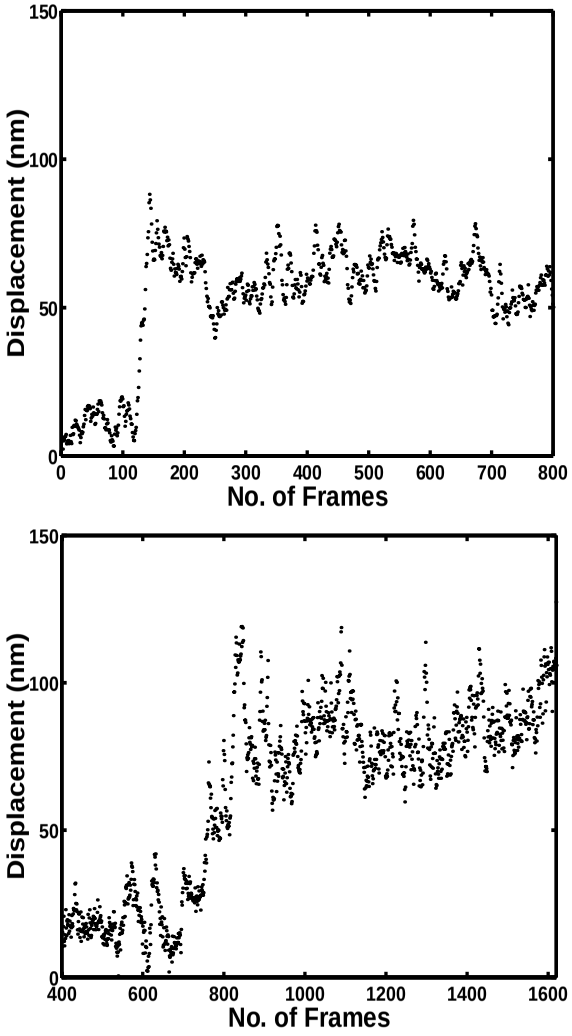

Figure 6.5. Typical curves for displacement of the trapped bead after pulling a membrane tether from the H-fraction (top panel), and the L-fraction (bottom panel)

the figures, almost all the network branches of the L-fraction stain preferentially for ER (Ribosome receptor) and almost none for Golgi (WGA). Figure 6.7 shows a typical image for networks from the H-fraction. In this case, the networks stain preferentially for the WGA-FITC staining (Figure 6.7 - top panel), indicating the presence of Golgi membrane; Ribosome-TR staining (Figure 6.7 - bottom panel) shows negligible staining of the network branches, indicating absence of ER membranes. These results show that the heavier fraction (H-fraction) is highly enriched in Golgi membranes and the lighter fraction (L-fraction) is enriched in membrane from the endoplasmic reticulum.

We also determined that membranes from the trans-Golgi network do not participate in *in vitro* network formation. We pre-incubated the cells in medium mixed with the fluorescent dye FM-143 (1 μM) for 30 min before harvesting. FM-143 is endocytosed into the cell by the plasma membrane and enters the vesicle trafficking pathway between the ER and Golgi. It localizes in the trans-Golgi network 30 min after endocytosis. We extracted membranes as before and formed networks. Observation of the samples showed that FM-143 labeled none of the networks from either fraction indicating that trans-Golgi membrane was not present.

6.3.4 Morphology

The polygonal networks formed from the two fractions had somewhat different morphology. The networks in the H-fractions are more 'floppy' (larger Brownian fluctuations) than the networks from the L-fraction, consistent with the lower tension of the H-fraction. Different widths also characterize the network branches in these two fractions. Figure 6.8 shows DIC images from the Golgi fraction (a) and ER fraction (b). The contrast of the membrane branch images in the Golgi network is higher than that in the ER network, suggesting that the former has a larger radius than

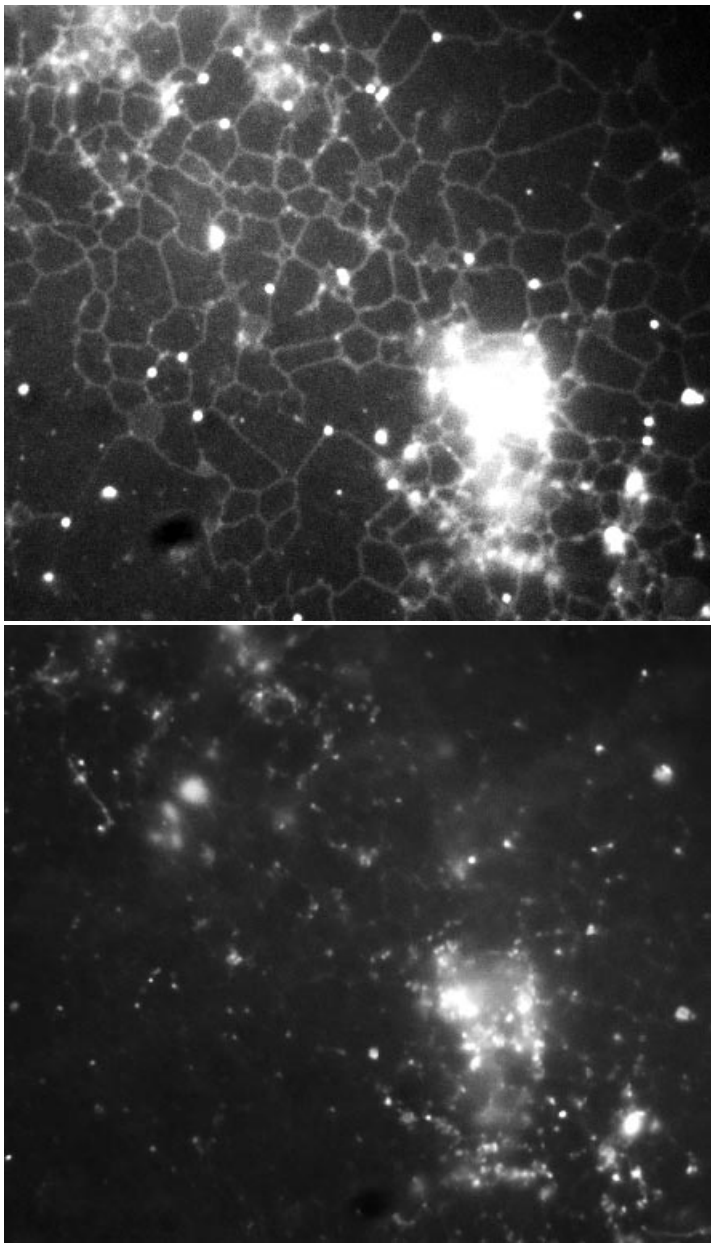

Figure 6.6. Double labeling of L-fraction network samples with Ribosome Receptor coupled to Texas Red - ER specific (top panel), and Wheat Germ Agglutinin coupled with FITC - Golgi specific (bottom panel)

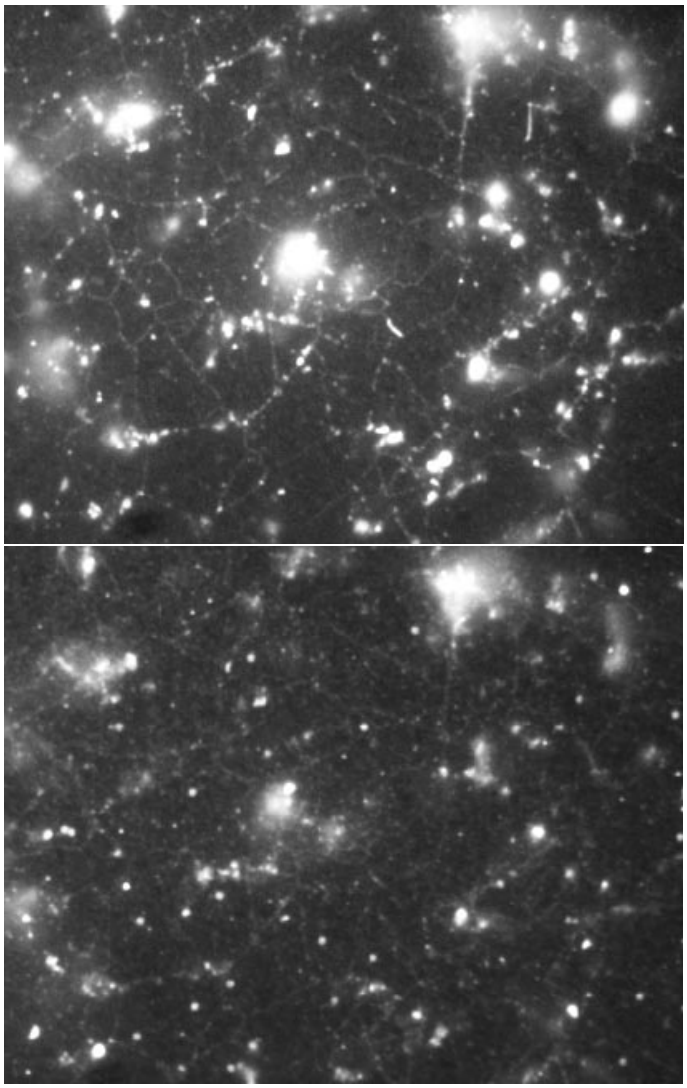

Figure 6.7. Double labeling of H-fraction network samples with Ribosome Receptor coupled to Texas Red - ER specific (top panel), and Wheat Germ Agglutinin coupled with FITC - Golgi specific (bottom panel)

the latter. We calculate the diameters of the tubules by determining the intensity profile by orthogonal scans across the DIC images of both kinds of membranes, and comparing them to intensities for beads of known diameter (as shown in Figure 6.9). We find that membrane tubules from networks of the H-fraction (Golgi) have an average diameter of ~ 180 nm while the L-fraction (ER) network branches are ~ 115 nm in diameter. Membrane tubules from the ER (E) are thicker than membrane tubules from the Golgi (G) by a factor $R_G/R_E = 1.57 \pm 0.2$. The inverse ratio of tether forces is $F_E/F_G = 1.63 \pm 0.3$. Table 6.1 tabulates these results.

TABLE 6.1. TETHER FORCES AND RADII OF GOLGI AND ER MEMBRANES.

	Tether Force (pN)	Radius (nm)
H-fraction (Golgi)	11.43±1.4	180±12
L-fraction (ER)	18.62±2.8	115±8
Ratios	$F_E/F_G = 1.63$	$R_G/R_E = 1.57$

6.3.5 Effect of Motor Inhibitors and Membrane Fusion

To check whether the molecular motors kinesin or dynein are responsible for generating the observed tensions, we used motor inhibitors to knock out these motors and then measured the tether forces. We incubated pre-formed network samples with (1) Kinesin inhibitor - adenylylimidodiphosphate (AMP-PNP, 2mM), and (2) Dynein inhibitor - sodium orthovanadate (Na_3VO_4, 0.5μM). We measured the tether force as for controls (with no inhibitors). Preliminary data shows that neither drug has any effect on the tether force for ER or Golgi membranes. To study the fusion between different membrane tubules, we pulled tethers, placed them above a nearby network branch and allowed them to fuse for several seconds. For homologous membrane types (*i.e.* ER to ER or Golgi to Golgi) fusion occurred $\sim 70\%$ of

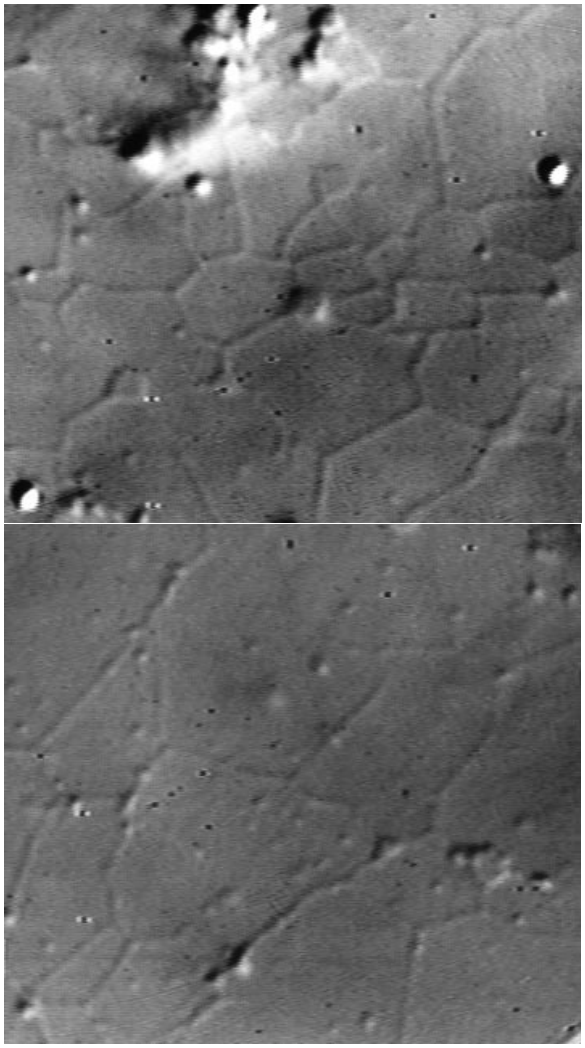

Figure 6.8. Membrane networks from the Golgi (top panel) have larger radii than network tubules from the ER (bottom panel)

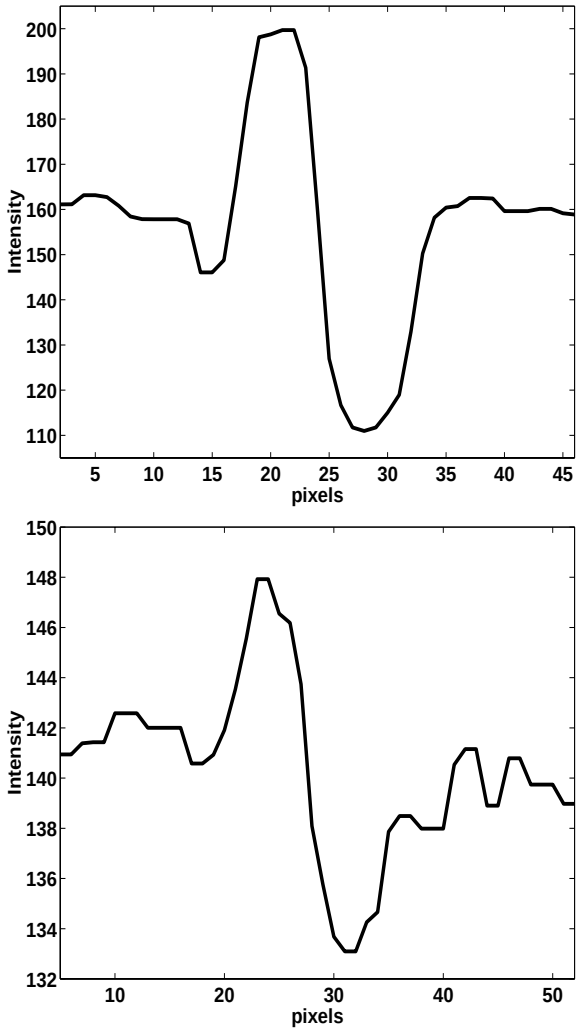

Figure 6.9. Representative plots of the intensity profiles of orthogonal scans across a bead of 500 nm radius (top panel), and a tubule of unknown radius (bottom panel)

the time. After fusion, the local configuration of the network changed to maintain the reticular structure with trigonal branching. For heterogenous membrane types, ER to Golgi or *vice versa*, we observed no fusion event.

6.4 Discussion

We perform a basic thermodynamic analysis of tether formation in which we equate the work done to form a tether to the increase in free energy of the network due to bending of the membrane when we pull a tether. The work done on the network is due to the tether force, F, and the tension, T, when we displace the tether a small distance dL_t:

$$dW = FdL_t - 2\pi R_t T dL_t, \tag{6.1}$$

where R_t is the radius of the tether. The increase in bending energy to form a tether of curvature $c = 1/R_t$ is:

$$dE = \frac{B}{2}c^2 dA, \tag{6.2}$$

where $dA = 2\pi R_t dL_t$ and B is the bending modulus of the membrane. Equating the two gives a relation for the tether force:

$$F = 2\pi R_t T + \frac{\pi B}{R_t}. \tag{6.3}$$

We see that the tether force has two components - one due to the tension and another due to the bending. We can obtain another independent relation between the tether force and bending by considering an isolated tether with a constant membrane surface area. A small increment in the static tether force F produces a deformation which causes an increase in length dL_t and a small decrease in radius dR_t. The change in free energy is only due to the change in curvature:

$$dE = BAcdc = -\frac{2\pi B L_t}{{R_t}^2} dR_t. \tag{6.4}$$

Equating this energy change to the work at the boundary, FdL_t, under conditions of constant surface area ($R_t dL_t = -L_t dR_t$) gives:

$$F = \frac{2\pi B}{R_t}. \tag{6.5}$$

From these equations we can relate the tether force F, the radius of the tether R_t, the bending stiffness of the membrane B and the membrane tension T by the following additional equations [191, 192]:

$$F = 4\pi R_t T, \tag{6.6}$$

and

$$F = 2\pi\sqrt{2BT}. \tag{6.7}$$

A difference in tether force can arise either due to a difference in bending stiffness or due to a difference in membrane tension. From our results for the forces and radii we can estimate the relative bending moduli. From Equation 6.5, the tether forces and radii of the two membrane types ER (E) and Golgi (G) relate by:

$$\frac{F_E}{F_G} = (\frac{B_E}{B_G})\frac{R_G}{R_E}. \tag{6.8}$$

From the experimental data shown in Table I, the two ratios are almost the same within error, implying that both membrane types have approximately the same bending stiffness ($B_E \sim B_G \sim 3.3\text{x}10^{-19}$ Nm). The bending stiffness is similar to that of growth cone membranes $\sim 2.7\text{x}10^{-19}$ Nm [188] and phospholipid bilayer membranes: $\sim 2.5\text{x}10^{-19}$ Nm [193] or $\sim 3.3\text{x}10^{-19}$ Nm [194]. Since the membranes have almost the same bending stiffness, a difference in tether forces reflects a difference in membrane tensions of tubulovesicular networks from the Golgi and the ER. Calculating the tensions explicitly using Equation 6.6, we find that the tension

in the ER membrane networks is $T_E \sim 0.013$ dyn/cm and the tension in the Golgi membrane is $T_G \sim 0.005$ dyn/cm. To put these tensions in perspective, membrane lysis requires tension of 5-10 dyn/cm.

Is the observed tension difference sufficient to cause membrane flow from Golgi to ER as observed after addition of BFA [181]? From measured redistribution of chimeras consisting of a membrane protein and green fluorescent protein, Sciaky *et al.* concluded that movement of membrane protein between Golgi and ER is due to convective flow rather than diffusive movement, with velocities on the order of 10mm/s [183]. Recently, Chizmadzhev *et al.* [195] have calculated the velocity of lipid transfer between fusing membranes at different tensions. Making some reasonable assumptions about the pore geometry and viscosity of these membranes ($\sim 10^{-6}$ g/s) we find that our observed tension difference (~ 0.01 dyn/cm) is consistent with the lipid flow velocities predicted by Sciaky *et al.*, further evidence that tension differences affect membrane flow in the cell.

Because we pull the tethers from a larger nonspherical membrane vesicle and the tether force is independent of the tether length, the source of the membrane tension is not clear. In plasma membranes, tether force primarily depends on membrane-cytoskeleton adhesion; but our membranes have no obvious structure corresponding to the cytoskeleton. Understanding the source of the difference in membrane tensions requires further work. One possibility is that the tension could be due to the action of microtubule motors which extend the membrane. Preliminary experiments of tension measurements of networks under the influence of motor inhibitors show no effect on the tether force, suggesting that the motors play a passive role, just serving to extend the network, while the tension difference arises from a difference in the chemical composition of the Golgi and ER membranes.

Since we were not able to observe fusion of heterogenous membrane types, we could not test *in vitro* whether tension differences were directly responsible for lipid flow. Possible future experiments include the use of BFA to induce fusion between ER and Golgi to mimic the *in vivo* situation. We could then directly measure lipid flow velocities and correlate with the expected velocities as predicted by the tension difference. Altering the chemical compositions of the membranes (say the lipid protein ratio) might also make it possible to investigate the effect on membrane tension. We do not completely understand the formation of these networks. We need theories based on the physical properties and the biochemistry of membranes to explain even the basic aspects like the selection of a particular tubule radius, branching and fusion.

CHAPTER 7

CONCLUSIONS

Our main goal has been to attempt a physical explanation of certain biological phenomena. We have obtained a picture where thermodynamics and fluid properties play an important role in examples ranging from embryogenesis to intracellular dynamics. In some cases, we also made analogies with new types of material such as granular media. Qualitative resemblance between two phenomena does not automatically establish that similar mechanisms are at work. Cell sorting resembles liquid phase separation and engulfment resembles coalescence, but, in spite of the visual similarity, the driving forces could be quite different. Only the kinetics of the process can provide a clue about the mechanisms. We have obtained quantitative results for cell sorting, tissue engulfment, cell motion in aggregates and intracellular membranes to support our previous qualitative understanding.

7.1 Cell Sorting

We studied the sorting out of dissimilar cell populations in chicken and *Hydra* cells and compared experiments to Potts model simulations. The simulations, which are based on the Differential Adhesion Hypothesis, reproduce the experimental patterns of sorting both qualitatively and quantitatively. The logarithmic evolution of boundary lengths in both sorting experiments and simulations show that a simple

physical model can explain the kinetics of sorting. Our work is a first step towards establishing a quantitative model.

We also described sorting as analogous to phase-separation in liquids. How far this analogy holds is still not entirely clear. For concentrated mixtures (large volume fraction of the minority phase), the domain growth rate in tissues is linear in time and agrees quite well with the theory for liquids. However, tissues sort completely even at volume fractions much lower than the critical volume fraction for complete phase separation in liquids. Further experiments will be useful in determining whether a critical concentration does exist for tissues, below which they do not sort (and the growth law is not linear). These experiments will require large aggregates with low concentrations of dark cells. Even if a critical concentration exists, we expect that it may be lower than that for liquids, because cells are actively driven. The study of phase separation in tissues is by itself an interesting topic - number densities of different types of cells might help to regulate the dynamics of reorganization in intact organisms.

In the linear growth regime, measurement of the rates for different combinations of tissues will give an estimate for the surface tension to viscosity ratio σ/η. Since we can measure viscosities by independent means [85], this ratio can provide an estimate for the interfacial tension between the two tissue phases, *i.e.* a measure of the heterotypic binding energies which are otherwise hard to measure.

We have just started preliminary work on Potts model simulation of phase separation. Further work will involve simulations in two and three dimensions to determine the growth laws for dilute and concentrated mixtures. In the model, cells have finite size unlike liquid molecules. We can explore the effects of varying different parameters like membrane rigidity, fluctuation temperature, surface energies

and volume compressibility, independently of each other. Thus, we can elucidate the role played by different properties in cell sorting dynamics, giving the Potts model some predictive power to determine which parameters are experimentally most important.

7.2 Engulfment

For the first time, we quantitated the rate of engulfment between two tissues. We found that the heterotypic interface grows linearly in time for biological tissues, model aggregates and liquid drops. The similarity of our experimental results with those of the Potts model simulations is encouraging - a simple model is enough to explain the dynamics. The linear growth rate, as expected for liquids, suggests that the two parameters surface tension and viscosity suffice to explain engulfment. Unlike phase separation, the kinetics of engulfment in liquids, has not been thoroughly investigated theoretically or experimentally. The next important step is to derive a theory for liquids to compare to our results for tissues. We must also measure the contact angles as a function of time to complete the comparison.

We need further experiments to study the interfacial growth rate for different tissue pairs *e.g.* heart-liver, neural-liver, heart-neural, etc. Again, values for the surface tension to viscosity ratios will allow us to determine interfacial tensions between tissue types. Three-dimensional imaging of the entire tissue using recent developments in advanced imaging techniques like two-photon microscopy would provide much greater accuracy.

7.3 Single Cell Motion

Having viewed sorting and engulfment in analogy with liquids, the next logical question was whether the individual subunits that control the dynamics, *i.e* the cells,

actually behave like liquid molecules, *i.e.* are they thermodynamically equivalent? Experiments (with Cytochalasin-B) have shown that sorting requires some random fluctuations - the cells must be actively motile. The general consensus is that cell movements accompanying sorting result from a combination of active (internally driven) and passive (surface tension guided) processes - "cooperative cell motion." We find that cell motion in aggregates is not entirely random, as studies with single non-interacting cells suggested. Complex interactions in a dense population lead to non-trivial behavior. We find long range correlations and non-Gaussian velocity distributions.

Our results point the way to a highly interesting field of research. We can formalize cell motion using a statistical mechanical framework. What happens with different tissue type combinations? What is the relative role of effective temperature versus effective viscosity? Can we draw some systematic conclusions? Rigorous quantitative analysis of cell motion in different environments (for example on various adhesive substrates mimicking *in vivo* situations) will be vital in identifying key mechanisms and characterizing different types of cells. *In vivo*, cells occur in many different environments; statistical analysis of physical parameters of cell locomotion can formally distinguish between these and identify behaviors depending on specific cell properties.

Another useful extension of our experiments will be to do them in three-dimensions, since the dynamics could depend on the dimensionality. We were not successful using confocal microscopy, due to limitations in the depth of tissue imaged. With advanced imaging technologies, *e.g.* two photon microscopy, imaging cell and tissue motion in three-dimensions should be possible.

7.4 Membrane Tension

Membrane tension is an important physical parameter that could regulate both plasma membrane dynamics and intracellular membrane trafficking. Cells may use membrane tension to control changes in cell shape and even cell motion. We have made the first measurements of membrane tension in Endoplasmic Reticulum and Golgi membranes. We used membrane fractions in the presence of cytoplasm, to form microtubule dependent tubulovesicular networks *in vitro*. Using optical tweezers we found that the tether force was 11.4 pN from Golgi networks and 18.6 pN from ER networks. Consequently, membrane tension was lower in the Golgi, providing direct evidence that differences in membrane tension between the two membrane types could drive movement of the Golgi into the ER when the two membranes fuse. Golgi network tubules were larger in diameter and were floppier in the light microscope than ER network tubules.

We have yet to determine the cause of the tension difference but we believe that differences in membrane composition are responsible. Further experiments in this direction using membranes with different compositions of lipids and proteins will be very useful. Quantitative studies of physical properties of membranes will be invaluable in understanding the effect of these on cell structure and function. Our long range goals are to understand how the cell regulates cell membrane properties and what effect membranes have on motion of organelles inside the cell and of the cell itself. Our work is one of the first steps in this direction.

Our experiments and models have reinforced our view of cells, tissues and membranes as objects with physical properties and of several biological phenomena as "physical" processes - where the outcomes depend not only on complex genetic rules, but are a natural consequence of the physics. Additionally, we also find interesting

departures from predictions based on simple models with an inherent lack of 'detail.' After all, cells are living objects and quite unlike inert matter in their form and function. Our research has been instructive - simple physical laws apply surprisingly often at certain scales (sorting, engulfment), but also, when we probe deeper, the situation becomes more complicated, *e.g.* single cell motion.

Our work though in no way complete, has opened interesting avenues of research.

APPENDIX A

EXPERIMENTAL PROTOCOLS

A.1 Experiments Using Chicken Embryos

This section contains the complete protocols for dissection, fluorescent labeling and manipulation of aggregates obtained from chick embryonic tissues, as used in experiments described in Chapter 3 and Chapter 4.

A.1.1 Basic Protocol for Dissecting Organs

(1) Sterilize instruments for 15 min in 70% ethanol.

(2) Spray eggs with 70% ethanol.

(3) Fill 3-4 Petri dishes with PBS solution.

(4) Crack open the eggs, remove the embryos with forceps and place in PBS.

(5) Wash embryos with PBS 3 times.

(6) Cover the Petri dishes and turn UV light on for 5-10 min.

(7) Dissect eyes from the embryos using fine scissors and forceps. Open up the body of the embryo ventrally, remove the heart and liver and place in PBS solution.

(8) Place eyes in a solution of 3% trypsin + 1% pancreatin; use 15 ml test tubes to put 5 eyes in 1.5 ml. of solution per test tube.

(9) Incubate for 15 min. in water bath at 37 °C.

(10) Prepare for dissection of eyes: Put instruments back in 70% ethanol and take a new set of Petri dishes.

(11) Fill dishes with Minimum Essential Medium (MEM) and wash chicken eyes four times.

(13) First remove the layer of connective tissue surrounding the eyeball. Then separate the neural and pigmented layers using very fine forceps.

(14) Place the separated layers in two test tube with MEM.

(15) After the separation is complete, remove all MEM from the test tubes.

(16) For dissociating into single cells, incubate the tissues in Trypsin-EDTA at 37 °C using the shaker bath. Incubate 25 min for neural, heart and liver tissues and 50 min for pigmented tissue.

(17) After incubation is complete, remove all the trypsin and put 1ml of MEM in the test tubes.

(18) Centrifuge for 3 min (velocity=3), to obtain a cell pellet.

(19) Wash the cells thoroughly in MEM (5 times).

(20) Using a long thin-tip Pasteur pipette resuspend the cells into a suspension by vigorous shearing (about 50 times for each test tube). Be careful not to introduce air bubbles into the medium.

(21) To count the density of cells, place 2 small drops of the cell suspension in the haemocytometer and observe under the microscope.

(22) Make aggregates either by shaking cell suspensions in culture flasks at 37°C or by pelleting and cutting into smaller fragments as outlined in the next section.

A.1.2 Further Steps for Engulfment Experiments

(1) Dissolve the lipophilic dye DiI in ethanol as a 2.5 mg/ml stock solution.

(2) Before use, dilute to 20-40 μg/ml in MEM, sonicate the solution and filter through a 0.45 μm pore size Millipore filter.

(3) Incubate cells to be labeled in this solution for 1 hr in the dark.

(4) Wash cell suspension in MEM three times before aggregate formation.

(5) Take about 5 x10^6 cells of each type in small Eppendorf tubes.

(6) Centrifuge them at 1000 rpm for 15 min to get thin pellets.

(7) Incubate the pellets at 37°C for 2-3 hr to allow the adhesion between cells to stabilize and strengthen.

(9) Remove the pellets from the tubes into Petri dishes filled with MEM at 37°C.

(10) Cut the pellets into tiny fragments $\sim 200\mu m$ in diameter, using microsurgical knife and forceps. While cutting, try to make the fragments circular in shape, getting rid of any sharp edges.

(11) Transfer each fragment into a single well of a 24-well cell well plate filled with medium.

(12) Incubate the fragments at 37°C for 12 hr in a shaker to allow them round up.

(13) Place pairs of spherical aggregates (one of heart tissue and one of neural retinal tissue) in 1.5 ml volume Eppendorf tubes.

(14) Centrifuge aggregate pair in a microcentrifuge at 1000 rpm for 10 min. (This is the lowest speed and time combination required to establish adhesion between aggregates).

(15) The aggregate pair settle at bottom of the tube and adhere to each other.

(16) Transfer the tubes to 37°C and incubate for 2-3 hours to strengthen the adhesion between the aggregates.

(17) Gently transfer each pair to one well of a 24-well cell-well plate and observe under the microscope.

A.2 Experiments Using *Hydra*

This section contains the complete protocols for dissociation of *Hydra* cells and separation of layers, as used for the experiments in Chapter 3 and Chapter 5.

A.2.1 Recipes for Media

To make 10 l hydra culture medium (HM), we mix the following with deionized double-distilled water.

- 30ml solution A: $NaHCO_3$, 0.5 M, 8.4 g, and 200 ml distilled water
- 10ml solution B: $MgCl_2 \cdot 6H_2O$, 0.1 M, 4.07 g, and 200 ml distilled water
- 10ml solution C: $MgSO_4$, 0.08 M, 1.93 g, and 200 ml distilled water
- 10ml solution D: KNO_3, 0.03 M, 0.61 g, and 200 ml distilled water
- 10ml solution E: $CaCl_2$, 1 M, 22.2 g, and 200 ml distilled water

Then use HCl buffer to make the pH 7.4.
To make 500 ml of dissociation medium (DM), we mix the following solutions in deionized double-distilled water.

- 25 ml solution A:
    1. $MgSO_4 \cdot 7H_2O$, 0.123 g, (0.245 g if 50 ml of solution A is needed).
    2. KCl 0.105 g, (0.21 g if 50 ml of solution A is needed).
    3. TES Buffer, 1.238 g, (2.475 g if 50 ml of solution A is needed).
- 25 ml solution B:
    1. Na_2HPO_4, 0.048 g, (0.095 g if 50 ml of solution B is needed).

2. KH_2PO_4, 0.030 g, (0.06 g if 50 ml of solution B is needed).

- 25 ml solution C:

  1. Na Pyruvic acid, 0.275 g, (0.55 g if 50 ml of solution C is needed).
  2. Na_3 Citrate, 0.735 g, (1.47 g if 50 ml of solution C is needed).

- 425 ml solution D:

  1. $CaCl_2 \cdot 2H_2O$, 0.368 g , (0.441 g if 510 ml of solution D is needed).

Then use HCl buffer to make the pH 6.90 .

A.2.2 Protocol for Dissociating *Hydra* Cells

(1) Using a scalpel, cut off the head and feet of 20-30 animals and place the bodies in a test tube.

(2) Wash the bodies 3 times with ice-cold Hydra Medium (HM) and twice with ice-cold Dissociation Medium (DM).

(3) Place the test tube on ice and incubate in the DM for about 30 min.

(4) Remove most of the DM and transfer the bodies onto a glass plate.

(5) Chop very finely with a single edged razor blade to obtain a paste like mass of tissue.

(6) Break the tissue into cells and cell clusters by vigorous pipetting in a test-tube using a thin tipped Pasteur pipette. Avoid formation of bubbles.

(7) Filter the cell solution through a 53 μm mesh to allow only single cells and small cell clusters to pass through.

(8) Centrifuge the suspension at 1500 rpm for 7 min to form a firm pellet.

(9) Remove the pellet using a large transfer pipette into a Petri dish filled with DM at 18°C.

(10) Cut the pellet into small aggregates, 200 μm to 400 μm in diameter, and transfer to cell-wells.

A.3 Membrane Network Experiments

This section contains protocols for the experiments on tubulo-vesicular networks as described in Chapter 6.

A.3.1 Preparation of Membrane Fractions

Internal membranes from Chick Embryo Fibroblasts (CEF) were obtained following standard protocols [189]. Four Roller Bottles of confluent CEF cells were incubated for 1 hour in 1 mM db-CAMP. Cells were washed and harvested with 0.05% trypsin-EDTA and pelleted at 1000 g for 10 min at 4°C. Cells were washed twice, resuspended in an equal volume of buffer PMEE′+ (35 mM PIPES, 5 mM $MgSO_4$, 5 mM EGTA, 0.5 mM EDTA (pH 7.4) with 1 mM dithiothreitol (DTT), 1 mM phenylmethylsulfonyl fluoride (PMSF), 1 mM protease cocktail mix) and homogenised. The homogenate was centrifuged at 1000 g for 15 min and the nuclear pellet (P1) was discarded. The supernatant (S1) was centrifuged at 100,000 g for 30 min at 4°C to obtain the membrane pellet (P2) and supernatant (S2). 20 μM of Taxol and 1 mM GTP was added to the supernatant (S2) and incubated at 37°C for 15 min to polymerize endogenous microtubules. This mixture was then centrifuged for 15 min at 21°C at 100,000 g. The pellet of endogenous microtubules was discarded and the supernatant (S3) was used neat in network formation. We separated the Golgi membrane from the ER using differential centrifugation. The S1 was diluted with PMEE′+ to 1 ml. This dilution was centrifuged at low speed (10,000 g) to obtain a pellet of the heavier membranes (H). The resulting supernatant was spun at high

speed (100,000 g) to get a pellet of lighter vesicles (L). H and L fractions were then resuspended in PMEE′+ and used for network formation and fluorescent assays.

A.3.2 Formation and Observation of Networks

To observe the formation of tubulovesicular networks, we formed $\sim$ 10 μl capacity flow chambers assembled from a slide, a 22 x 22 mm^2 coverslip and two parallel strips of 70 μm thick double stick tape. To facilitate the formation of a microtubule mesh, we flowed anti-tubulin antiserum (1:40 dilution) into the chamber, incubated it for 5 min at room temperature and washed it away with excess PMEE′+ (40 μl). The chamber was then perfused with taxol stabilized microtubules (10 μl, at 0.1-0.5 mg/ml) made from tubulin purified from bovine brain and incubated in a humid chamber for 15-20 min. Unbound microtubules were washed with washing buffer (PMEE′+, 1 mM GTP, 20 μM Taxol). Membrane fractions (5 μl) with motor supernatant (3 μl) and Mg-ATP (2 μl) were introduced into the flow chambers and network formation was assayed after about 60 min incubation at 37 ° C. The membrane concentration was titrated by dilution in PMEE ′+.

Preparation of Beads

For the purposes of optical trapping we used 0.5 μm diameter carboxylate microspheres from Polysciences, Inc. The beads were activated using standard protocol with 1-(3-dimethylaminopropyl)-3-ethylcarbodiimide (EDC). After activation, beads were coated with either 2B6 antibody (anti-kinectin antibody, which has a preference for ER membranes) or WGA (Wheat Germ Agglutinin, which binds preferentially to the Golgi membrane).

Imaging

We monitored network formation by differential interference contrast (DIC) microscopy at room temperature with a Zeiss Axiovert 100 microscope equipped with a 1.4 numerical aperture (NA) oil condenser and a 100x, 1.4 NA Planapochromat DIC objective. A halogen lamp provided illumination. A Hammamatsu Newvicon camera collected images and a Hammamatsu Argus-10 image processor performed contrast enhancement, background subtraction and frame averaging prior to recording the images real time on a Panasonic S-VHS video recorder. We used a cooled charge coupled device (CCD) camera (Princeton Instruments) for the fluorescence imaging of networks.

BIBLIOGRAPHY

[1] D. Godt and U. Tepass, "Drosophila oocyte localization is mediated by differential cadherin-based adhesion," Nature **395,** 387–391 (1998).

[2] P. B. Armstrong, "Cell sorting out: the self-assembly of tissues *in vitro*," Crit. Rev. Biochem. molec. Biol. **24,** 119–149 (1989).

[3] R. A. Foty, G. Forgacs, C. M. Pfleger, and M. S. Steinberg, "Liquid properties of embryonic tissues: Measurement of interfacial tensions," Phys. Rev. Lett. **72,** 2298–2301 (1994).

[4] F. Graner and Y. Sawada, "Can surface adhesion drive cell-rearrangement? Part II: A geometrical model," J. theor. Biol. **164,** 477–506 (1993).

[5] J. C. M. Mombach, J. A. Glazier, R. C. Raphael, and M. Zajac, "Quantitative comparison between differential adhesion models and cell sorting in the presence and absence of fluctuations," Phys. Rev. Lett. **75,** 2244–2247 (1995).

[6] J. P. Rieu, N. Kataoka, and Y. Sawada, "Quantitative analysis of cell motion during sorting in two-dimensional aggregates of dissociated *Hydra* cells," Phys. Rev. E. **57,** 924–931 (1998).

[7] N. Kataoka, K. Saito, and Y. Sawada, "NMR microimaging of the cell sorting process," Phys. Rev. Lett. **82,** 1075–1078 (1999).

[8] H. Tanaka, "New coarsening mechanisms for spinodal decomposition having droplet pattern in binary fluid mixture: collision-induced collisions," Phys. Rev. Lett. **72,** 1702–1705 (1994).

[9] S. Torza and S. G. Mason, "Coalescence of two immiscible liquid drops," Science **163,** 813–814 (1969).

[10] B. Alberts, D. Bray, J. Lewis, M. Raff, K. Roberts, and J. D. Watson, *Molecular Biology of the Cell*, 3rd ed. (Garland, New York, 1994).

[11] R. Lipowsky, "The conformation of membranes," Nature **349,** 475–481 (1991).

[12] R. Lipowsky, "The morphology of lipid membranes," Curr. Opin. Struct. Biol. **5,** 531–540 (1995).

[13] M. Mutz and W. Helfrich, "Unbinding transition of a biological model membrane," Phys. Rev. Lett. **62,** 2881–2884 (1989).

[14] E. Evans, "New physical concepts for cell amoeboid motion," Biophys. J. **64,** 1306–1322 (1993).

[15] M. Bloom, E. Evans, and O. G. Mouritsen, "Physical properties of the fluid lipid-bilayer component of cell membranes: a perspective," Q. Rev. Biophys. **24,** 293–397 (1991).

[16] S. J. Singer and G. L. Nicolson, "The fluid mosaic model of the structure of cell membranes," Science **175,** 720–731 (1972).

[17] A. Curtis, in *Physical Basis of Cell-Cell Adhesion*, P. Bongrand, ed., (Boca Raton, Florida: CRC Press, 1988), Chap. 9.

[18] G. I. Bell, "A theoretical model for adhesion between cells mediated by multivalent ligands," Cell Biophys. **1,** 133–147 (1979).

[19] *Physical Basis of Cell-Cell Adhesion*, P. Bongrand, ed., (Boca Raton, FL: CRC Press, 1988).

[20] A. Nicol and D. R. Garrod, "Fibronectin, intercellular junctions and the sorting-out of chick embryonic tissue cells in monolayer," J. Cell. Sci. **54,** 357–372 (1982).

[21] D. R. McClay and C. A. Ettensohn, "Cell adhesion in morphogenesis," Ann. Rev. Cell. Biol. **3,** 319–345 (1987).

[22] *The Cell in Contact*, G. Edelman and J. P. Thiery, eds., (England: Wiley, 1985).

[23] G. I. Bell, in *Physical Basis of Cell-Cell Adhesion*, P. Bongrand, ed., (Boca Raton, Florida: CRC Press, 1988), Chap. 10.

[24] M. Takeichi, "Cadherin cell adhesion receptors as a morphogenetic regulator," Science **251,** 1451–1455 (1991).

[25] M. S. Steinberg, "Adhesion-guided multicellular assembly: a commentary upon the postulates, real and imagined, of the differential adhesion hypothesis, with special attention to computer simulations of cell sorting," J. theor. Biol. **55,** 431–443 (1975).

[26] S. A. Newman and W. D. Comper, "Generic physical mechanisms of morphogenesis and pattern formation," Development **110,** 1–18 (1990).

[27] D. R. McClay, "The role of thin filopodia in motility and morphogenesis," Exp. Cell. Res. **253,** 296–301 (1999).

[28] R. E. Keller, "Review: cell rearrangement in morphogenesis," Zool. Science **4,** 763–779 (1987).

[29] D. K. Fristom, "The cellular basis of epithelial morphogenesis. A review," Tissue Cell **20,** 645–690 (1988).

[30] C. A. Erickson, "Cell migration in the embryo and adult organism," Curr. Opinion Cell Biol. **2,** 67–74 (1990).

[31] S. Carter, "Haptotaxis and the mechanism of cell motility," Nature **213,** 253–260 (1967).

[32] E. Ruoslahti, "How cancer spreads," Sci. Am. **275,** 72–77 (1996).

[33] M. S. Steinberg, "Reconstitution of tissues by dissociated cells," Science **141,** 401 (1963).

[34] M. S. Steinberg, in *Cellular Membranes in Development*, M. Locke, ed., (New York: Academic Press, 1964).

[35] M. S. Steinberg, "Does differential adhesion govern self-assembly processes in histogenesis? Equilibrium configurations and the emergence of a hierarchy among populations of embryonic cells," J. Exp. Zool. **173,** 395 (1970).

[36] G. Oster, "On the crawling of cells," J. Embryol. Exp. Morph. **83s,** 329–364 (1983).

[37] G. Oster and A. Perelson, "The physics of cell motility," J. Cell. Sci. Suppl. **8,** 35–54 (1987).

[38] A. G. Jacobson, G. F. Oster, G. M. Odell, and L. Y. Cheng, "Neurulation and the cortical tractor model for epithelial folding.," J. Embryol. Exp. Morphol. **96,** 19–49 (1986).

[39] H. M. Phillips and M. S. Steinberg., "Embryonic tissues as elasticoviscous liquids: I. Rapid and slow shape changes in centrifuged cell aggregates," J. Cell Sc. **30,** 1–20 (1978).

[40] M. Weliky and G. Oster, "The mechanical basis of cell rearrangement. I. Epithelial morphogenesis during *Fundulus* epiboly," Development **109,** 373–386 (1990).

[41] A. Grebecki, "Membrane and cytoskeletal flow in motile cells with emphasis on the contribution of free-living amoeba," Int. Rev. Cytol. **148,** 37–79 (1994).

[42] T. P. Stossel, "On the crawling of animal cells," Science **260,** 1086–1094 (1993).

[43] M. P. Sheetz, "Cell migration by graded attachment to susbstrates and contraction," Semin. Cell Biol. **5,** 149–155 (1994).

[44] D. A. Lauffenburger and A. F. Horwitz, "Cell migration: A physically integrated process," Cell **84,** 359–369 (1996).

[45] T. J. Mitchison and L. P. Cramer, "Actin-based cell motility and cell locomotion," Cell **84,** 371–379 (1996).

[46] L. P. Cramer, T. J. Mitchison, and J. A. Theriot, "Actin-dependent motile forces and cell motility," Curr. Opinion Cell Biol. **6,** 82–86 (1994).

[47] J. A. Theriot and T. J. Mitchison, "Actin microfilament dynamics in locomoting cells," Nature **352,** 126–131 (1991).

[48] J. A. Theriot, "Regulation of the actin cytoskeleton in living cells," Semin. Cell Biol. **5,** 193–199 (1994).

[49] J. V. Small, G. Rinnerthaler, and H. Hinssen, "Organization of actin meshworks in cultured cells: the leading edge," Cold Spring Harbor Symp. Quant. Biol. **46,** 599–611 (1982).

[50] J. V. Small, M. Herzog, and K. Anderson, "Actin filament organization in the fish keratocyte lamellipodium," J. Cell Biol. **129,** 1275–1286 (1995).

[51] P. Matsudaira, "Actin cross-linking proteins at the leading edge," Semin. Cell Biol. **5,** 165–174 (1994).

[52] J. A. Theriot and T. J. Mitchison, "Comparison of actin and cell surface dynamics in motile fibroblasts," J. Cell. Biol. **118,** 367–377 (1992).

[53] Y. Wang, "Exchange of actin subunits at the leading edge of living fibroblasts: possible role of treadmilling," J. Cell Biol. **101,** 597–602 (1985).

[54] J. Condeelis, "Life at the leading edge," Ann. Rev. Cell Biol. **9,** 411–444 (1993).

[55] J. A. Cooper, "The role of actin polymerization in cell motility," Ann. Rev. Physiol. **53,** 585–605 (1991).

[56] J. D. Cortese, B. Schwab, C. Frieden, and E. L. Elson, "Actin polymerization induces shape changes in actin-containing vesicles," Proc. Natl. Acad. Sci. **86,** 5773–5777 (1989).

[57] C. S. Peskin, G. M. Odell, and G. F. Oster, "Cellular motions and thermal fluctuations: the Brownian ratchet," Biophys. J. **65,** 316–324 (1993).

[58] A. Mogilner, "Cell motility driven by actin polymerization," Biophys. J. **71,** 3030–3045 (1996).

[59] A. Trembley, *Memoirs pour Servir a L'Histoire Naturelle d'un Genre de Polypes D'Eau Douce, a Bras en Forme de Cornes* (Leyden, 1744).

[60] H. V. Wilson, "On some phenomena of coalescence and regeneration in sponges," J. Exp. Zool. **5,** 245–258 (1907).

[61] J. Holtfreter, "Experimental studies on the development of the pronephros," Rev. Can. Biol. **3,** 220 (1944).

[62] P. L. Townes and J. Holtfreter, "Directed movements and selective adhesion of embryonic amphibian cells," J. Exp. Zool. **128,** 53–120 (1955).

[63] M. S. Steinberg, "On the mechanism of tissue reconstruction by dissociated cells. III. Free energy relations and the reorganization of fused, heteronomic tissue fragments," Proc. Nat. Acad. Sci. USA **48,** 1769–1776 (1962).

[64] A. Gierer, S. Berking, H. Bode, C. David, K. Flick, G. Hansmann, H. Schaller, and E. Trenkner, "Regeneration of *Hydra* from reaggregated cells," Nature New Biol. **239,** 98–101 (1972).

[65] A. A. Moscona, "Patterns and mechanisms of tissue reconstruction from dissociated cells," in *Developing Cell Systems and Their Control*, D. Rudnick, ed., (Academic Press, New York, 1960), p. 45.

[66] D. R. Garrod and M. S. Steinberg, "Tissue specific sorting out in two dimensions in relation to contact inhibition of cell movement," Nature **244,** 568–569 (1973).

[67] A. Nicol and D. R. Garrod, "The sorting out of embryonic cells in monolayer, the differential adhesion hypothesis and the non-specificity of cell adhesion," J. Cell. Sci. **38,** 249–266 (1979).

[68] P. Weiss and A. C. Taylor, "Reconstitution of complete organs from single-cell suspensions of chick embryos in advanced stages of differentiation," Proc. Natl. Acad. Sci. U. S. A. **46,** 1177 (1960).

[69] M. T. Zenzes and W. Engel, "The capacity of ovarian cells of the postnatal rat to reorganize into histotypic structures," Differentiation **19,** 199–202 (1981).

[70] K. D. Ansevin, "Aggregative and histoformative performance of adult frog liver cells maintained in vitro," J. Exp. Zool. **155,** 371 (1964).

[71] P. Cau, M. Michel-Bechet, and G. Fayet, "Morphogenesis of thyroid follicles in vitro," Adv. Anat. Embryol. Cell Biol. **52,** 3–66 (1976).

[72] D. R. Friedlander, R. M. Mege, B. A. Cunningham, and G. M. Edelman, "Cell sorting-out is modulated by both the specificity and amount of different cell adhesion molecules," Proc. Natl Acad. Sci. USA **86,** 7043–7047 (1989).

[73] M. S. Steinberg and M. Takeichi, "Experimental specification of cell sorting, tissue spreading, and specific spatial patterning by quantitative differences in cadherin expression," Dev. Biol. **91,** 206–209 (1994).

[74] A. Gonzalez-Reyes and D. S. Johnston, "The Drosophila A-P axis is polarised by the cadherin-mediated positioning of the oocyte," Development **125,** 3635–3644 (1998).

[75] P. B. Armstrong, "Modulation of tissue affinities of cardiac myocyte aggregates by mesenchyme," Dev. Biol. **64,** 60 (1978).

[76] J. R. Downie, "The mechanism of chick epiblast expansion," J. Embryol. exp. Morph. **35,** 559–575 (1976).

[77] E. Ho and Y. Shimada, "Formation of the epicardium studied with the scanning electron microscope," Dev. Biol. **66,** 579–585 (1978).

[78] H. M. Phillips and G. S. Davis, "Liquid-tissue mechanics in amphibian gastrulation: Germ-layer assembly in *Rana pipiens*," Am. Zool. **18,** 81–93 (1978).

[79] P. B. Armstrong and J. S. Child, "Stages in the normal development of *Fundulus heteroclitus*," Biol. Bull. Mar. Biol. Lab. Woods Hole **128,** 143–168 (1965).

[80] T. J. Poole and M. S. Steinberg, "Amphibian pronephric duct morphogenesis: Segregation, cell rearrangement and directed migration of the Ambyostoma duct rudiment," J. Embryol. Exp. Morph. **63,** 1–16 (1981).

[81] D. A. Frenz, N. S. Jakaria, and S. A. Newman, "The mechanism of precartilage mesenchymal condensation," Dev. Biol. **136,** 97–103 (1989).

[82] M. S. Steinberg, P. B. Armstrong, and R. E. Granger, "On the recovery of adhesiveness by trypsin-dissociated cells," J. Membr. Biol. **13,** 97–128 (1973).

[83] R. A. Foty, C. M. Pfleger, G. Forgacs, and M. S. Steinberg, "Surface tensions of embryonic tissues predict their mutual envelopment behavior," Development **122,** 1611–1620 (1996).

[84] G. M. Davis, H. M. Phillips, and M. S. Steinberg, "Germ layer surface tensions and "tissue affinities" in *Rana pipiens* gastrulae: Quantitative measurements," Dev. Biol. **192,** 630–644 (1997).

[85] G. Forgacs, R. A. Foty, Y. Shafrir, and M. S. Steinberg, "Viscoelastic properties of living embryonic tissues: A quantitative study," Biophys. J. **74,** 2227–2234 (1998).

[86] A. W. Adamson, *Physical Chemistry of Surfaces* (John Wiley & Sons, New York, 1967).

[87] H. M. Phillips, M. S. Steinberg, and B. H. Lipton, "Embryonic tissues as elasticoviscous liquids: II. Direct Morphological evidence for cell slippage in centrifuged aggregates," Dev. Biol. **59,** 124–134 (1977).

[88] J. T. H. Mandeville, R. N. Ghosh, and F. R. Maxfield, "Intracellular calcium levels correlate with speed and persistent forward motion in migrating neutrophils," Biophys. J. **68,** 1207–1217 (1995).

[89] G. A. Dunn and A. F. Brown, "A unified approach to analysing cell motility," J. Cell. Sci. Suppl. **8,** 81–102 (1987).

[90] D. Wessels, N. A. Schroeder, J. C. E. Voss, A. L. Hall, and D. R. Soll, "cAMP-mediated inhibition of intracellular particle movement and actin reorganization in *Dictyostelium*," J. Cell. Biol. **109,** 2841–2851 (1989).

[91] J. C. M. Mombach and J. A. Glazier, "Single cell motion in aggregates of embryonic cells," Phys. Rev. Lett. **76,** 3032–3035 (1996).

[92] A. Czirok, K. Schlett, E. Madarasz, and T. Vicsek, "Exponential distribution of locomotion activity in cell cultures," Phys. Rev. Lett. **81,** 3038–3041 (1998).

[93] R. T. Tranquillo, "Self-organization of tissue-equivalents: The nature and role of contact guidance," Biochem. Soc. Symp. **65,** 27–42 (1999).

[94] R. B. Dickinson, S. Guido, and R. T. Tranquillo, "Biased cell migration of fibroblasts exhibiting contact guidance in oriented collagen gels," Ann. Biomed. Eng. **22,** 342–356 (1994).

[95] *Structure and Dynamics of Membranes, Handbook of Biological Physics*, R. Liposwky and E. Sackmann, eds., (Elsevier, Amsterdam, 1995).

[96] S. A. Safran, *Statistical Thermodynamics of Surfaces, Interfaces and Membranes*, Vol. 90 of *Frontiers in Physics* (Addison-Wesley, Reading, Mass., 1994).

[97] W. Helfrich, "Elastic properties of lipid bilayers: theory and possible experiments," Z. Naturforsch. **28c,** 693–703 (1973).

[98] R. Golestanian, M. Goulian, and M. Kardar, "Fluctuation-induced interactions between rods on a membrane," Phys. Rev. E **54,** 6725–6734 (1996).

[99] M. Elbaum, D. K. Fygenson, and A. Libchaber, "Buckling microtubules in vesicles," Phys. Rev. Lett. **76,** 4078–4081 (1996).

[100] W. Hackl, M. Barmann, and E. Sackmann, "Shape changes of self-assembled actin bilayer composite membranes," Phys. Rev. Lett. **80,** 1786–1789 (1998).

[101] J. B. Manneville, P. Bassereau, D. Levy, and J. Prost, "Activity of transmembrane proteins induces magnification of shape fluctuations of lipid membranes," Phys. Rev. Lett. **82,** 4356–4359 (1999).

[102] I. Cantat and C. Misbah, "Dynamics and similarity laws for adhering vesicles in haptotaxis," Phys. Rev. Lett. **83,** 235–238 (1999).

[103] A. Turing, "The chemical basis of morphogenesis," Phil. Trans. Roy. Soc. B. **237,** 37–72 (1952).

[104] J. D. Murray, *Mathematical Biology* (Springer, Berlin, 1993).

[105] L. Wolpert, "The development of pattern and form in animals," in *Carolina Biol. Readers*, J. J. Head, ed., (Scientific Publications Div., Carolina Supply Co., Burlington, North Carolina, 1977), No. 51, pp. 1–16.

[106] G. Odell, G. Oster, P. Alberch, and B. Burnside, "The mechanical basis of morphogenesis. I. Epithelial folding and invagination," Dev. Biol. **85,** 446–462 (1981).

[107] N. Goel, R. Campbell, R. Gordon, R. Rosen, H. Martinez, and M. Ycas, "Self sorting of isotropic cells," J. theor. Biol. **28,** 423–468 (1970).

[108] N. Goel and A. Leith, "Self sorting of anisotropic cells," J. theor. Biol. **28,** 469–482 (1970).

[109] R. Gordon, N. Goel, M. S. Steinberg, and L. L. Wiseman, "A rheological model sufficient to explain the kinetics of cell-sorting," J. theor. Biol. **37,** 43–73 (1972).

[110] N. S. Goel and G. Rogers, "Computer simulation of engulfment and other movements of embryonic tissues," J. theor. Biol. **71,** 103–140 (1978).

[111] G. Rogers and N. S. Goel, "Computer simulation of cellular movements: cell-sorting, cellular migration through a mass of cells and contact inhibition," J. theor. Biol. **71,** 141–166 (1978).

[112] R. J. Matels and R. J. Fletterick, "A topological exchange model for cell self-sorting," J. theor. Biol. **76,** 403–414 (1979).

[113] T. Rogers and J. Sampson, "Computer simulations of surface tensions in cellular aggregates," Inter. J. Biol. Med. Comp. **8,** 45–68 (1977).

[114] D. Greenspan, "A classical molecular approach to computer simulation of biological sorting," J. theor. Biol. **12,** 227–235 (1981).

[115] D. Sulsky, S. Childress, and J. K. Percus, "A model of cell sorting," J. theor. Biol. **106,** 275–301 (1984).

[116] R. B. Potts, Proc. Camb. Phil. Soc. **48,** 106 (1952).

[117] P. S. Sahni, G. S. Grest, M. P. Anderson, and D. J. Srolovitz, "Kinetics of the Q-state Potts model in two dimensions," Phys. Rev. Lett. **50,** 263–266 (1983).

[118] J. A. Gazier, "Grain growth in three dimensions depends on grain topology," Phys. Rev. Lett. **70,** 2170–2173 (1993).

[119] Y. Jiang, Ph.D. thesis, University of Notre Dame, 1998.

[120] F. T. Lewis, "The analogous shapes of cells and bubbles," Proc. A. A. A. S. **77,** 147–186 (1948).

[121] J. A. Glazier and F. Graner, "Simulation of the differential adhesion driven rearrangement of biological cells," Phys. Rev. E **47,** 2128–2154 (1993).

[122] F. Graner, "Can surface adhesion drive cell-rearrangement? Part I: Biological cell-sorting," J. theor. Biol. **164,** 455–476 (1993).

[123] *Measuring Cell Adhesion*, A. S. Curtis and J. M. Lackie, eds., (Wiley, England, 1991).

[124] F. Graner and J. A. Glazier, "Simulation of biological cell sorting unsing a two-dimentional extended Potts model," Phys. Rev. Lett. **69,** 2013–2016 (1992).

[125] A. Upadhyaya, J. P. Rieu, J. A. Glazier, and Y. Sawada (unpublished).

[126] P. B. Armstrong and D. Parenti, "Cell sorting in the presence of Cytochalasin B," J. Cell Biol. **55,** 542–553 (1972).

[127] M. Abercrombie, "The crawling movement of metazoan cells," Proc. R. Soc. Lond. (Biol.) **207,** 129–147 (1980).

[128] S. B. Carter, "Effects of cytochalasins on mammalian cells," Nature **213,** 256 (1967).

[129] J. A. Cooper, "Effects of cytochalasin and phalliodin on actin," J. Cell Biol. **105,** 1473–1478 (1987).

[130] M. S. Steinberg and L. L. Wiseman, "Do morphogenetic tissue rearrangements require active cell movements? The reversible inhibition of cell sorting and tissue spreading by cytochalasin B," J. Cell Biol. **55,** 606–615 (1972).

[131] J. W. Sanger and H. Holtzer, "Cytochalasin B: Effects on cell morphology. cell adhesion, and mucopolysaccharide synthesis," Proc. Natl. Acad. Sci. **69,** 253–257 (1972).

[132] M. P. Sarras, M. E. Madden, X. M. Zhang, S. Gunwar, J. K. Huff, and B. G. Hudson, "Extracellular matrix (mesoglea) of *Hydra vulgaris*. I. Isolation and characterization," Dev. Biol. **148,** 481–494 (1991).

[133] S. E. Fraser, C. R. Green, H. R. Bode, and N. B. Gilula, "Selective disruption of gap junctional communication interferes with a patterning process in hydra," Science **237,** 49–55 (1987).

[134] H. G. E. Hentschel and A. Fine, "Instabilities in cellular dendritic morphogenesis," Phys. Rev. Lett. **72,** 3592–3595 (1994).

[135] M. Sato-Maeda, M. Uchida, F. Graner, and H. Tashiro, "Quantitative evaluation of tissue-specific cell adhesion at the level of a single cell pair," Dev. Biol. **162,** 77–84 (1994).

[136] E. D. Siggia, "Late stages of spinodal decomposition in binary mixtures," Phys. Rev. A **20,** 595–605 (1979).

[137] A. Onuki, "Domain growth and rheology in a phase-separating binary mixture with viscosity difference," Europhys. Lett. **28,** 175–179 (1994).

[138] V. S. Nikolayev, D. Beysens, and P. Guenoun, "New hydrodynamic mechanism for drop coarsening," Phys. Rev. Lett. **76,** 3144–3147 (1996).

[139] J. D. Gunton, M. S. Miguel, and P. S. Sahni, in *Phase Transitions and Critical Phenomena*, C. Domb and J. L. Lebowitz, eds., (Academic Press, New York, 1983), Vol. 8, p. 267.

[140] F. Perrot, P. Guenoun, T. Baumberger, D. Beysens, Y. Garrabos, and B. L. Neindre, "Nucleation and growth of tightly packed droplets in fluids," Phys. Rev. Lett. **73,** 688–691 (1994).

[141] K. Binder and D. Stauffer, "Theory for the slowing down of the relaxation and spinodal decomposition of binary mixtures," Phys. Rev. Lett. **33,** 1006–1009 (1974).

[142] J. E. Farrell and O. T. Valls, "Spinodal decomposition in a two-dimensional fluid model," Phys. Rev. B **40,** 7027–7039 (1989).

[143] F. J. Alexander, S. Chen, and D. W. Grunau, "Hydrodynamic spinodal decomposition: Growth kinetics and scaling functions," Phys. Rev. B. **48,** 634–637 (1993).

[144] D. A. Beysens, G. Forgacs, and J. A. Glazier, "Networks of droplets induced by coalescence: application to cell sorting," In *Dynamical Networks in Physics and Biology*, D. A. Beysens and G. Forgacs, eds., pp. 161–169 (Springer-Verlag, Berlin, 1997).

[145] W. J. Ma, A. Maritan, J. R. Banavar, and J. Koplik, "Dynamics of phase separation of binary fluids," Phys. Rev. A **45,** R5347–R5350 (1992).

[146] G. Forgacs, N. Jaikaria, H. L. Frisch, and S. A. Newman, "Wetting, percolation and morphogenesis in a model tissue system," J. theor. Biol. **140,** 417–430 (1989).

[147] J. S. Rowlinson and B. Widom, *Molecular Theory of Capillarity* (Clarendon Press, Oxford, 1982).

[148] J. Frenkel, "Viscous flow of crystalline bodies under the action of surface tension," J. Physics **9,** 385–390 (1945).

[149] R. J. Good and E. Elbing, "Generalization for theory for estimation of interfacial energies," Ind. Eng. Chem. (Am. Chem. Soc.) **62,** 54–78 (1970).

[150] A. Lamura, G. Gonnella, and J. M. Yeomans, "A lattice Boltzmann model of ternary fluid mixtures," Europhys. Lett. **45,** 314–320 (1999).

[151] U. D'Ortona, D. Salin, M. Cieplak, R. B. Rybka, and J. R. Banavar, "Two-color nonlinear Boltzmann cellular automata: Surface tension and wetting," Phys. Rev. E. **51,** 3718–3728 (1995).

[152] M. Cieplak, "Rupture and coalescence in two-dimensional cellular automata fluids," Phys. Rev. E. **51,** 4353–4361 (1995).

[153] K. W. Doolittle, I. Reddy, and J. G. McNally, "3D analysis of cell movements during normal and myosin-II-null cell morphogenesis in *Dictyostelium*," Dev. Biol. **167,** 118–129 (1995).

[154] A. Huttenlocher, R. S. Sandborg, and A. F. Horwitz, "Adhesion in cell migration," Curr. Opinion Cell Biol. **7,** 697–706 (1995).

[155] U. Technau and T. Holstein, "Cell sorting during the regeneration of *Hydra* from reaggregated cells," Dev. Biol. **151,** 117–127 (1992).

[156] R. D. Campbell, "Vital marking of single cells in developing tissues: India ink injection to trace tissue movements in *Hydra*," J. Cell Sci. **13,** 651–661 (1973).

[157] Y. Kishimoto, M. Murate, and T. Sugiyama, "*Hydra* regeneration from recombined ectodermal and endodermal tissue," J. Cell Sci. **109,** 762–772 (1996).

[158] T. H. Solomon, E. R. Weeks, and H. L. Swinney, "Observation of anomalous diffusion and Levy flights in a two-dimensional rotating flow," Phys. Rev. Lett. **71,** 3975–3978 (1993).

[159] A. Ott, J. P. Bouchad, D. Langevin, and W. Urbach, "Anomalous diffusion in "living polymers": A genuine Levy flight?," Phys. Rev. Lett. **65,** 2201–2204 (1990).

[160] H. Spohn, "Surface dynamics below the roughening transition," J. Phys. I **3,** 69 (1993).

[161] J. P. Bouchaud and A. Georges, "Anomalous diffusion in disordered media - statistical mechanisms, models and physical applications," Phys. Rep. **195,** 127–293 (1990).

[162] D. H. Zanette and P. A. Alemany, "Thermodynamics of anomalous diffusion," Phys. Rev. Lett. **75,** 366–369 (1995).

[163] C. Tsallis and D. J. Bukman, "Anomalous diffusion in the presence of external forces: Exact time-dependent solutions and their thermostatistical basis," Phys. Rev. E. **54,** R2197–R2200 (1996).

[164] L. Borland, "Microscopic dynamics of the nonlinear Fokker-Planck equation: A phenomenological model," Phys. Rev. E **57,** 6634–6642 (1998).

[165] C. Tsallis, "Non-extensive thermostatistics: Brief review and comments," Physica A **221,** 277–290 (1995).

[166] R. Silva, A. R. Plastino, and J. A. S. Lima, "A Maxwellian path to the q-nonextensive velocity distribution function," Phys. Lett. A 249 (1998).

[167] A. Compte and F. Jou, "Non-equilibrium thermodynamics and anomalous diffusion," J. Phys. A. **29,** 4321–4329 (1996).

[168] M. B. Schneider, J. T. Jenkins, and W. W. Webb, "Thermal fluctuations of large quasi-spherical bimolecular phospholipid vesicles," J. Physique **45,** 1457–1472 (1984).

[169] Y. Murayama and M. Sano, "Transition from Gaussian to non-Gaussian velocity distribution functions in a vibrated granular bed," J. Phys. Soc. Jap. **67,** 1826–1829 (1998).

[170] Y. H. Taguchi and H. Takayasu, "Power law velocity fluctuations due to inelastic collisions in numerically simulated vibrated bed of powder," Europhys. Lett. **30,** 499–504 (1995).

[171] W.-J. Rappel, A. Nicol, A. Sarkissian, H. Levine, and W. F. Loomis, "Self-organized vortex state in two-dimensional *Dictyostelium* dynamics," Phys. Rev. Lett. **83,** 1247–1250 (1999).

[172] E. O. Budrene and H. C. Berg, "Complex patterns formed by motile cells of *Escherichia coli*," Nature **349,** 630–633 (1991).

[173] E. O. Budrene and H. C. Berg, "Dynamics of formation of symmetrical patterns by chemotactic bacteria," Nature **376,** 49–53 (1995).

[174] J. A. Shapiro and D. Trubatch, "Sequential events in bacterial colony morphogenesis," Physica D **49,** 214–223 (1991).

[175] T. Vicsek, A. Czirok, E. Ben-Jacob, I. Cohen, and O. Shochet, "Novel type of phase transition in a system of self-driven particles," Phys. Rev. Lett. **75,** 1226–1229 (1995).

[176] A. Czirok, E. Ben-Jacob, I. Cohen, and T. Vicsek, "Formation of complex bacterial colonies via self-generated vortices," Phys. Rev. E. **54,** 1791–1801 (1996).

[177] A. Czirok, M. Vicsek, and T. Vicsek, "Collective motion of organisms in three dimensions," Physica A **264,** 299–304 (1999).

[178] P. Allegrini, M. Buiatti, P. Grigolini, and B. J. West, "Non-Gaussian statistics of anomalous diffusion: The DNA sequences of prokaryotes," Phys. Rev. E. **58,** 3640–3648 (1998).

[179] M. P. Sheetz and J. Dai, "Modulation of membrane dynamics and cell motility by membrane tension," Trends in Cell Biol. **6,** 85–89 (1996).

[180] D. Raucher and M. P. Sheetz, "Membrane expansion increases endocytosis rate during mitosis," J. Cell. Biol. **144,** 497–506 (1999).

[181] J. Lippincott-Schwartz, L. C. Yuan, J. S. Bonifacino, and R. D. Klausner, "Rapid redistribution of Golgi proteins into the ER in cells treated with Brefeldin A: Evidence for membrane cycling from Golgi to ER," Cell **56,** 801–813 (1989).

[182] J. Lippincott-Schwartz, J. G. Donaldson, A.Schweizer, E. G. Berger, H. Hauri, L. C. Yuan, and R. D. Klausne, "Microtubule-dependent retrograde transport of proteins into the ER in the presence of Brefeldin A sugggests an ER recycling pathway," Cell **60,** 821–836 (1990).

[183] N. Sciaky, J. Presley, C. Smith, K. J. M. Zaal, N. Cole, J. E. Moreira, M. Terasaki, E. Siggia, and J. Lippincott-Schwartz, "Golgi tubule traffic and the effects of Brefelden A visualized in living cells," J. Cell. Biol. **139,** 1137–1155 (1997).

[184] S. L. Dabora and M. P. Sheetz, "The microtubule-dependent formation of a tubulovesicular network with characteristics of the ER from cultured cell extracts," Cell **54,** 27–35 (1988).

[185] V. J. Allan and R. D. Vale, "Membrane formation and tubule transport in vitro," J. Cell Biol. **13,** 347–359 (1991).

[186] C. Lee and L. B. Chen, "Dynamic behavior of endoplasmic reticulum in living cells," Cell **54,** 37–46 (1988).

[187] C. M. Waterman-Storer, J. Gregory, S. F. Parsons, and E. D. Salmon, "Membrane/microtubule tip attachment complexes (TACs) allow the assembly dynamics of plus ends to push and pull membranes into tubulovesicular networks in interphase *Xenopus* egg extracts," J. Cell Biol. **130,** 1161–1169 (1995).

[188] J. Dai and M. P. Sheetz, "Mechanical properties of neuronal growth cone membranes studied by tether formation with laser optical tweezers," Biophys. J. **68,** 988–996 (1995).

[189] J. M. McIlvain, C. Lamb, S. Dabora, and M. P. Sheetz, "Microtubule motor-dependent formation of tubulovesicular networks from Endoplasmic Reticulum and Golgi membranes," Methods in Cell Biology **39,** 227–236 (1993).

[190] B. J. Schnapp, J. Gelles, and M. P. Sheetz, "Nanometer-scale measurements using video-light microscope," Cell Motil. Cytoskel. **10,** 47–53 (1988).

[191] R. M. Hochmuth, J. Y. Shao, J. Dai, and M. P. Sheetz, "Deformation and flow of membranes into tethers extracted from neuronal growth cones," Biophys. J. **70,** 358–369 (1996).

[192] R. E. Waugh, J. Song, S. Svetina, and B. Zeks, "Local and nonlocal curvature elasticity in bilayer membrane by tether formation from lecithin vesicles," Biophys. J. **61,** 974–982 (1992).

[193] E. A. Evans and W. Rawicz, "Entropy-driven tension and bending elasticity in condensed-fluid membranes," Biophys. J. **64,** 2094–2097 (1990).

[194] J. Song and R. E. Waugh, "Bending rigidity of SOPC membrane containing cholesterol," Biophys. J. **64,** 1967–1970 (1993).

[195] Y. A. Chizmadzhev, D. A. Kumenko, P. I. Kuzmin, L. V. Chernomordic, J. Zimmerberg, and F. S. Cohen, "Lipid flow through fusion pores connecting membranes of different tensions," Biophys. J. **76,** 2951–2965 (1999).